Comparing CID Dissociation of PAH Ions with iPEPICO: Implications for the RRKM Modeling of CID Breakdown Diagrams

Sabria Emamer Mabruk Mohamed

Thesis submitted to the
Faculty of Graduate & Postdoctoral Studies
University of Ottawa
In partial fulfillment of the requirements for the
MSc. degree in the Ottawa-Carleton Chemistry Institute

Department of Chemistry and Biomolecular sciences
Faculty of Science
University of Ottawa

To my father,

Who did not see him and I have not lived in his compassion

Abstract

In the last several decades, polycyclic aromatic hydrocarbons (PAHs) have been the subject of extensive investigation due to their presumed abundance in the interstellar medium (ISM). My thesis concentrated on investigating the dissociation of ionized PAH molecules in the gas phase under similar conditions of the ISM. The twelve PAHs studied were naphthalene (NAP), anthracene (ANT), phenanthrene (PHN), cyclopenta[d,e,f] phenanthrene (CYC), pyrene (PYR), fluoranthene (FLN), perylene (PER) and coronene (COR). In addition, two dihydro PAHs were studied to examine potential intermediates in H_2 catalysis, 1,2-dihydronaphthalene (DHN) and 9,10-dihydrophenanthrene (DHP), and two stabilized fragments of PAHs, acenaphthylene (ACE), fluorene-H (FLU). These ions were studied using atmospheric pressure chemical ionization (APCI) to generate the ions and the fragmentation was produced by collision induced dissociation (CID). The CID experiments were done at different lab frame collision energies to produce breakdown curves for all fragments in each molecule. These curves were fitted by using Rice – Ramsperger-Kassel- Marcus (RRKM) theory to derive the activation energy (E_0) at 0K and the entropy of activation ($\Delta^{\ddagger} S$) for each reaction.

The primary dissociation channel observed was H loss and this fragmentation channel was a common fragment to all PAHs molecules studied. Also, there were other fragments (CH_3, C_2H_2, C_4H_2) observed in all of these molecules studied except perylene and coronene. The final step in this project was to compare these results with results derived from imaging photoelectron photoion coincidence spectroscopy (iPEPICO) reported by West and co-workers in order to determine the suitability of the APCI-CID technique for deriving reliable kinetic parameters for this class of ions.

Acknowledgments

I would not have been able to complete the requirements of this degree without them. First of all, I would like to thank my mom for all her support and encouragement throughout the years. I would like to thank my husband, Abdurazagh Mansur and my boys Aslam, Minyar and Maburk, for their love and support. It is for this reason I give this thesis to them.

Next, I am thankful to my supervisor, Dr. Paul Mayer, for giving me the opportunity to work under his supervision. He was always available for discussion and never stopped for giving excellent advice and feedback. I am grateful for his precious patience with me and my thesis. For this, I am exceedingly thankful.

I would also like to thank Dr. Sander Mommers, Dr. Sharon Curtis and Sean Overton for their knowledge about the instrument.

Finally, I would like to thank my best friend Dr. Barbara Francisco. She was always available when I need her. I am extremely grateful. I am thankful to Alica Sit for helping me to understand RRKM theory and teach me how can I use Gaussview program. Also, I would like to thank other members of the Mayer research group: Dr. Justin Renaud. Dr. Ameneh Gholami,Dr. Brandi West, Dr. Hauyu Xue, Eduardo Solano, Jeffery Butson, Jaleh Halvachizadeh, Jenna Hamilton, Melanie Ouelette, Peter Chen, Shaan Rashid, Samata Khan, and Iden Djavani.

Table of Contents

List of Figures

List of Tables

List of abbreviations

PAHs	Polycyclic aromatic hydrocarbons
ZPE	Zero Point Energy
ISM	Interstellar medium
DFT	Density functional theory
E_0	0K activation energy (eV)
$\rho(E)$	Reaction ion density of states
RRKM	Rice–Ramsperger–Kassel–Marcus
T_i	Initial temperature
$\Delta^{\ddagger}S$	Entropy of activation
T_{eff}	Effective temperature
BIDs	Diffuse interstellar bands
SLS	Swiss Light Source
UIBs	Unidentified infrared bands
TOF	Time of flight
MAH	Monocyclic aromatic hydrocarbon
MCP	Microchannel plate
UV	Ultraviolet
α	alpha (Kev^{-1})
IR	Infrared
$TS^{\ddagger}$	Transition state
IVR	Intramolecular vibrational relaxation
$N^{\ddagger}$	Transition state sum of state
MS	Mass spectrometry

m/z	Mass-to-charge ratio
APCI	Atmospheric Pressure Chemical Ionization
LC	Liquid chromatography
MS/MS	Tandem mass spectrometry
Dc	Direct current
RF	Radio frequency
CID	Collision induced dissociation
E_{lab}	Lab frame collision energy
E_{com}	Center of mass collision energy
B3LYP	Becke 3-Parameter (Exchange), Lee, Yang and Parr
iPEPICO	imaging photoelectron photoion coincidence spectroscopy

Molecular name abbreviations

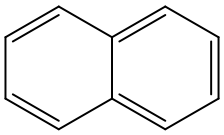

Naphthalene
(NAP)

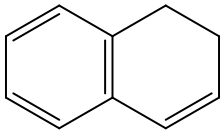

Dihydronaphthalene
(DHN)

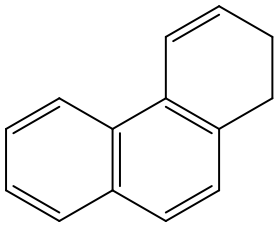

Dihydrophenanthrene
(DHP)

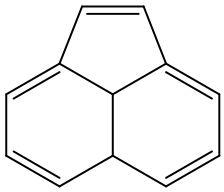

Acenaphthylene
(ACE)

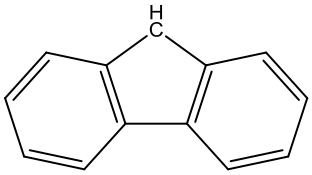

Fluorene-H
(FLU)

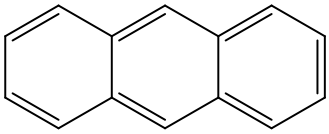

Anthracene
(ANT)

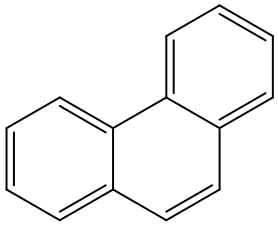

Phenanthrene
(PHN)

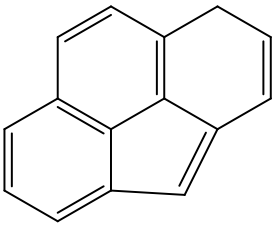

Cyclopenta[d,e,f]phenanthrene
(CYC)

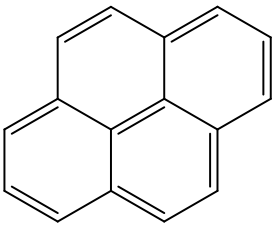

Pyrene
(PYR)

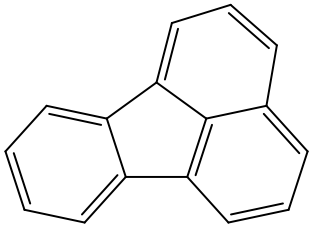

Fluoranthene
(FLN)

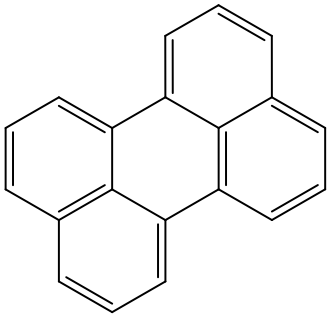

Perylene
(PER)

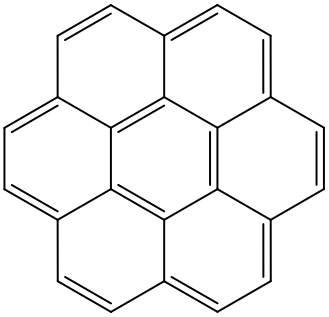

Coronene
(COR)

Chapter 1 Introduction

1.1 Objectives

The purpose of this project has been to study the dissociation of polycyclic aromatic hydrocarbons (PAHs) in the gas phase under the same conditions of the interstellar medium (ISM). A combination of mass spectrometry and theory was used to model the dissociation pathways of a variety of PAH ions: naphthalene, anthracene, phenanthrene, cyclopenta[d,f,e]phenanthrene, pyrene, fluoranthene, perylene, and coronene; two hydrogenated PAHs: 1,2-dihydronaphthalene and 9,10-dihydrophenanthrene; and two stable fragments: acenaphthylene and fluorene. RRKM theory was used to derived the energy of activation (E_0) and activation entropy ($\Delta^{\ddagger}S$) for all primary channels for each ion. The results were compared to the more robust, but less accessible technique of imaging photoelectron photoion coincidence spectroscopy.

1.2 The molecules in the interstellar medium

On a clear summer nights, if we look up, we find that the space between stars is empty, but it is not true. The space between the stars in our Milky Way consists of gas and dust, which astronomers name the interstellar medium (ISM). The ISM contains hydrogen gas, molecules, and grains of dust.[1] These regions are not easy to see with the naked eyes, Fig 1.1.

Figure 1-1: Shows many aspects of the interstellar medium which are very hard to see with the naked eyes. The image is taken from Interstellar Medium: Cold - University of Oregon.[45] http://abyss.uoregon.edu/~js/ast122/lectures/lec22.html

Many astronomers focus their research on knowing how many molecular and atomic species exist in the ISM. The first three molecules: CN, CH, and CH^+, were discovered in the interstellar medium between 1937 and 1941. [2] The molecules OH, H_2O and NH_3 were discovered by their spectroscopic emission lines in 1965. [3] At the beginning of 1970, the expansion of millimeter telescopes was used to discover many other molecules by their rotational emissions.[3, 4] Currently, over 120 molecules and ions have been confirmed in the ISM, which includes both diffuse and dark clouds, and most of them contain from 2 to 13 atoms. [1,5,6] Table 1.1 shows the list of molecules that have been observed.[1]

Table 1.1: Molecules observed in the ISM.[1]

Atoms	Molecular species
2	H_2, OH, SO, SH, SO^+, SiO, SiS, SiC, SiN, HCl, NaCl, KCl, AlCl, AlF, NH, NO, NS, HF, CH, CH^+, CN, CO, CO^+, C_2, CS, CP, PN, PO
3	H_2O, H_2S, HNO, HCO, HCO^+, H_3^+, N_2H^+, NH_2, N_2O, OCS, C_2H, HCS^+, CO_2, C_2O, C_2S, C_3, MgCN, MgNC, NaCN, HCN, HNC, KCN, CH_2, SO_2, SiH_2, SiC_2, HOC^+
4	NH_3, H_3O, H_2CO, H_2CS, HNCO, HNCS, C_3N, HCO_2^+, C_3H, C_3O, C_3S, C_2H_2, CNH_2^+, HC_2N, H_2CN, H_3O^+, SiC_3
5	SiH_4, CH_4, HCOOH, HC_3N, CH_2NH, NH_2CN, H_2C_2O, C_4H, CH_2CN, C_5, SiC_4, C_3H_2, HC_2NC, HC_3N, H_2COH^+
6	CH_3OH, NH_2CHO, CH_3CN, CH_3NC, CH_3SH, C_5H, HC_2CHO, CH_2CH_2, H_2C_4, HC_3NH^+, C_5N, C_6^-, C_5S
7	CH_3CHO, CH_3NH_2, CH_3C_2H, CH_2CHCN, HC_5N, C_6H, C_7^-, CH_2OCH_2
8	CH_3CO_2H, CH_3C_3N, C_7H, H_2C_6, C_8^-
9	CH_3CH_2OH, CH_3OCH_3, CH_3CH_2CN, CH_3C_4H, HC_7N, C_8H, C_9^-
10	CH_3COCH_3, CH_3C_5N
11	HC_9N
13	$HC_{11}N$

The molecules observed in the ISM are generally organic molecules and can have either linear (l) or cyclic (C) geometry. Many of them are hydrocarbon molecules with nitrogen and oxygen heteroatoms. [1,7]The molecules are presented in Table 1.1 appear independent of the elemental abundance in space; Table 1.2 shows the list of the abundance of elements in the universal, compared to hydrogen. [8]

Table 1.2: Universal abundances of elements relative to hydrogen. [8]

Element	Abundance	Element	Abundance
H	1.00	Si	$3.5*10^{-5}$
He	0.10	S	$1.6*10^{-5}$
O	$7.4*10^{-4}$	P	$2.8*10^{-7}$
C	$4.0*10^{-4}$	Cl	$1.1*10^{-7}$
N	$9.3*10^{-5}$	K	$1.3*10^{-7}$
Na	$2.1*10^{-6}$	Ca	$2.3*10^{-6}$
Mg	$3.8*10^{-5}$	Fe	$3.2*10^{-5}$

The organic molecules studied in this thesis are polycyclic aromatic hydrocarons, or PAH, molecules. More detail about PAH molecules will be provided in section 1.4

The molecules, ions, and radicals mentioned earlier are not found homogeneously in the ISM but rather are restricted to certain environments.The ISM consists of three primary kinds of large-scale structures called clouds: diffuse clouds, translucent clouds, and dense clouds. [2] The molecular species found in each cloud is a function of the chemical and physical conditions found in each, which are summarized in fig 1.2.

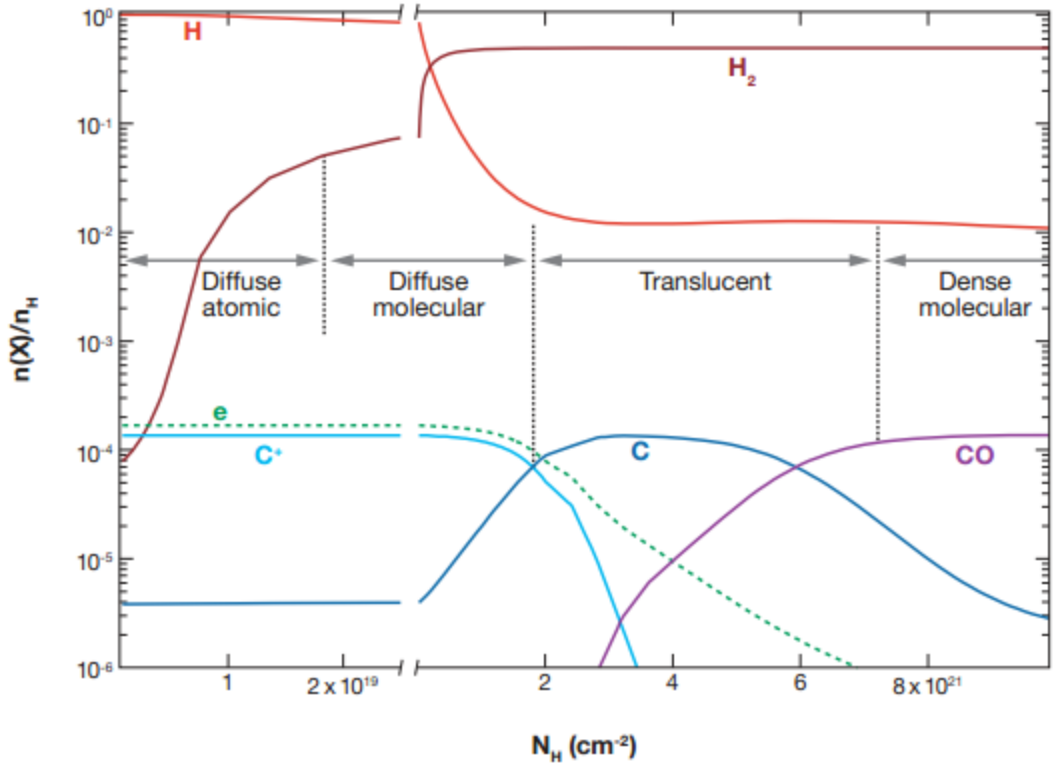

Figure 1-2: Physical and chemical condition of three cloud types in the ISM (with nH = 102 cm-3 and XUV = 1).[9]

The first type of interstellar clouds is diffuse clouds. They are observed at low concentrations of interstellar matter with densities of 10^1- 10^2 atoms cm^{-3} while the translational gas temperature is 100-120 K, see Table 1.3. [10] They are named diffuse due to the fact that UV radiation can pass though them easily, and these photons have played an important role in the diffuse clouds chemistry as they include molecule photodissociation. Additionally, molecules and atoms can photoionize in these clouds that have less photodissociation energy than the hydrogen atomic line (13.59 eV). So, the atomic ion species that have been found in such clouds including carbon C (11.26 eV), sulfur S (10.36 eV), silicon Si (8.15 eV), and magnesium Mg (7.64 eV). Nitrogen N (14.53 eV) and oxygen O (13.62 eV) exist in their neutral atomic form. Also, the diatomics H_2, C_2, CH, CH^+, CN, CS, OH, CO, and HCl have

discovered unequivocally. Only four types of triatomics (HCN, HNC, C_2H, and HCO^+) are detected.[11] The aromatic species cyclopropenylidene (c-C_3H_2) and molecular formaldehyde (H_2CO) have observed too. Moreover, large molecules can be present in this cloud, such as polycyclic aromatic hydrocarbons (PAHs).[12]

Table 1.3: illustrates the physical parameters in the different clouds of ISM.[12]

region	molecules	density, cm^{-3}	temp, K
diffuse clouds	simple molecules H2, CH+, CH, CN, C2, OH, CO, HCO+, HCN	10^1-10^2	100-120
translucent clouds	simple molecules H2, CH+, CH, CN, C2, OH, CO, HCO+, HCN	10^2-10^3	50-100
dense clouds (molecular clouds) (cold clouds)	carbon-rich, linear and cyclic molecules with up to 13 atoms	10^2-10^4	10-15

The second cloud is translucent clouds which are intermediate between diffuse and dense structures. In this cloud, the density value ranged of 10^2-10^3 atoms cm^{-3} and low translational temperatures of gas of 50-100 K, Table 1.3. [13] The molecular synthesis of the translucent clouds as Cygnus OB2 12, HD 147889, HD 29647 and Cas A is reflected via small diatomics such as H_2, C_2, CH, CH^+, CN, CS, CO, and OH jointly with other large species as HNC, HNC, C_2H, H_2-CO, and HCO^+ . Also, the molecule of tricarbon C_3 was recognized in HD 147889. The interstellar CH_2 abundance was importantly increased in the cold cloud when comparing with the regions of low density.

Finally, dense clouds are shaped from low-density clouds by densities of number of10^2-10^4 atoms cm^{-3}. These clouds structures referred as cold clouds because of their low gas translational temperatures of 10-15K.[14,9] Likewise, these clouds are known as dark clouds due to the fact that they appear asblack spots on images. However, while molecule formation in diffuse and translucent clouds is dominated by photoionization and photochemistry, that in dense clouds is dominated by reactions on interstellar dust particle (submicrometer-sized silicate- and carbonaceous-based grain nuclei). The dense clouds protection complex molecules

from the damaging short wavelength radiation field.[15] Dense clouds contain many neutral molecules and the primarily molecule in this clouds is H_2, which is followed by CO with an abundance of about 10^{-4} of that of H_2. Other species appeared as well in this cloud such as CH, OH, CN, and H_2O showed only 10^{-7} of the H_2 abundance. [16,17] Also, dense clouds contain many of molecules that include carbon-rich, linear, and cyclic molecules with up to 13 atoms.[12]

One of the major pieces of evidence for the existence of large organic molecules in the diffuse ISM is the appearance of diffuse interstellar bands (DIBs).

1.3 Diffuse Interstellar Bands (DIBs)

The diffuse interstellar bands (DIBs) are a group of absorption bands that appear when astronomers obtain spectra of clouds in the ISM. An example is shown in fig 1.3.[18,19,20,21] Heger reported the first DIBs in 1922. In 1930, Merrill confirmed the interstellar origin of these DIBs.[18,22,23,24] There are more than 300 DIBs that have been observed, ranging from the UV to IR regions of the electromagnetic spectrum, and almost all of these bands are created by large organic molecules.[19,20,24,25,26,27] The carriers of DIB are one of the longest-standing mysteries in astronomy. By the beginning of the 1980s, DIBs were accepted by many astronomers to be key to understanding the chemistry of the ISM.[28,29]

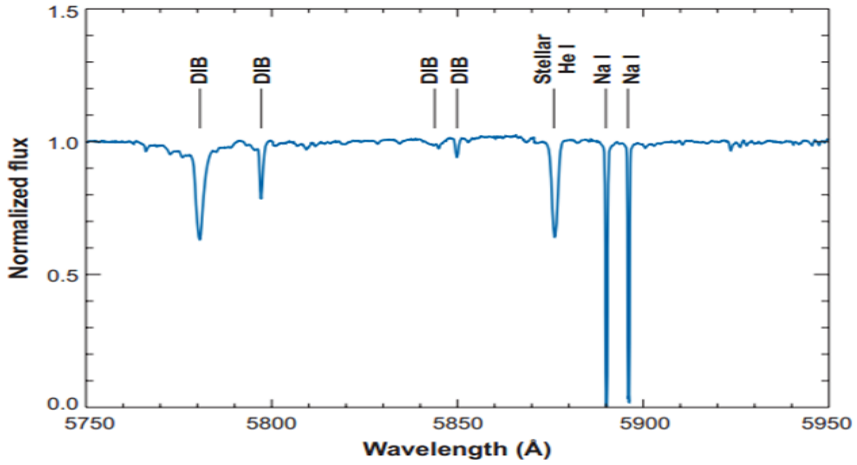

Figure 1-3: Diffuse interstellar bands spectrum (DIBs), which consist of two for the sodium D-line and one for helium in a neutral state (He I) at right. The two peaks of the end of spectrum at left were the first DIBs reported over 95 years ago.[17]

There have been many guesses about which molecules generate the DIBs. The discussion has largely focussed on two kinds of molecules: PAHs and carbon chains. PAH molecules are interesting due to the aromatic nature of the carriers of several unidentified infrared bands (UIBs) and their likely appearance in the diffuse clouds, which lead them to present as strong candidates for carriers of the DIBs.[28,30,31] Carbon chains are thought of as candidates because many of molecular species confirmed in the ISM have open-chain structures. However, carbon chains have not been confirmed in diffuse atomic clouds which show the strongest DIBs, Table 1.3.[29]

The experimental data and physical models for large PAH molecules, which consist of 30 carbon atoms or more, are the most promising carriers of DIB.[29] Nevertheless, these molecules present problems to spectroscopists because it is not easy to vaporize and study these molecules in the gas phase.[31,32,33] The potential abundance of PAHs indicates that these molecule are one of the large molecular groups found in space, and that they possibly make up 5%–20% of the total abundance of carbon in the ISM. This abundance could be enough to calculate the observed starlight absorption in DIBs.[16, 34,35] At the end, any molecule contributing to the DIBs can produce new understanding of the ISM chemistry.

1.4 Polycyclic Aromatic Hydrocarbons (PAHs)

PAHs are unsaturated molecules of carbon and hydrogen, containing 6-member carbon rings akin to graphite.[36] These molecules have high thermal and radiation stability because of the electron arrangement in the molecule. A monocyclic aromatic hydrocarbon (MAH) has a monocular ring. By using a number of MAH a large polycyclic molecule can be created, examples of which are shown in Fig 1.4.[36]

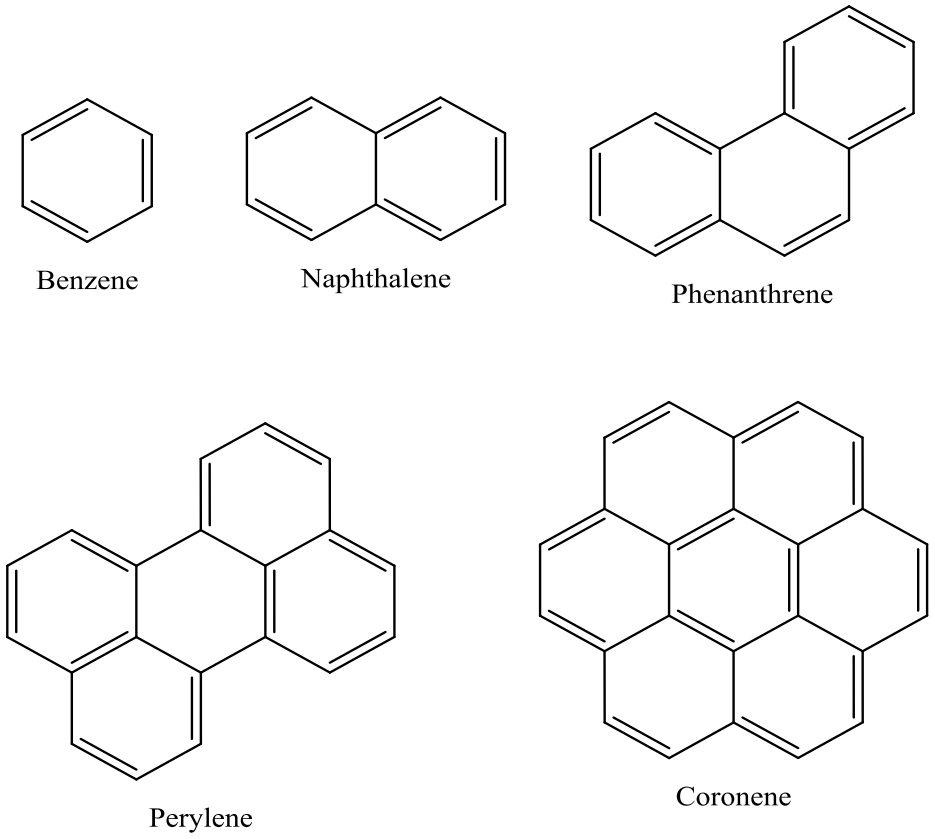

Figure 1-4:shows the schematic of molecule structure of C_6H_6, $C_{10}H_8$, $C_{14}H_{10}$, $C_{20}H_{12}$ and $C_{24}H_{12}$.

PAHs absorb radiation in the ultraviolet (UV) region of the electromagnetic spectrum and can emit infrared (IR) radiation via radiationless transitions from electronic excited states to leading to vibrationally-excited levels in the ground state (intramolecular vibrational relaxation, or IVR). [27,19] The molecule then cools by emission of infrared photons. [37, 38]

PAH molecules have appeared in the interstellar IR emission spectrum, which exhibit important features at 3.3, 6.2, 7.7, 8.6, 11.2 and 12.7 µm, fig 1.5. [37]

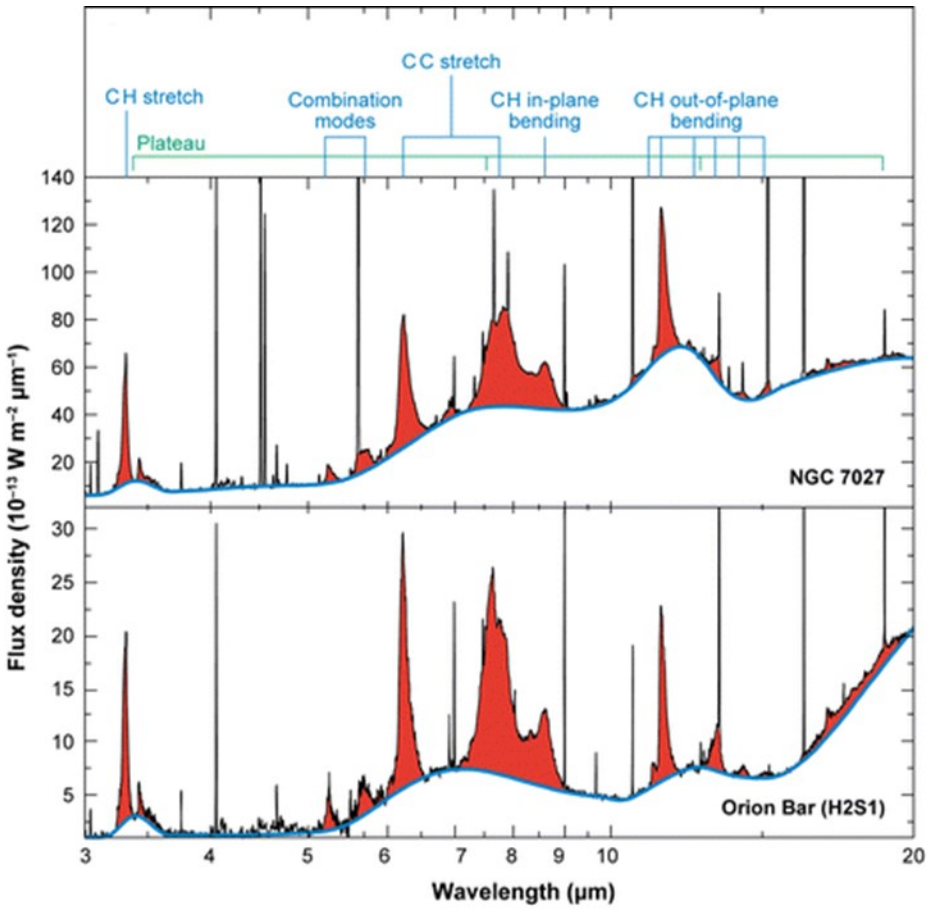

Figure 1-5: Features of the IR emission spectrum in the interstellar medium, labeled with the corresponding PAH vibrational modes.[37]

The propensity of C-C and CH stretching and bending modes is one feature that led to the hypothesis that PAH molecules are responsible for the IR emission.[37,39] While small molecules have distinctive partial features and thus are easily identified in the ISM, they tend to have poor emission probabilities compared to longer molecules.[19,27,40]

PAH molecules can be divided into closed-shell neutral, radical or ionized.[19,27,40] Neutral PAHs have comparatively strong spectral features for the C-H bonds at 3.3, 11.3 and 12.7 μm while ionization raises the relative importance of emissions at 6.2, 7.7 and 8.6 μm for the C-C bonds, Fig 1.6. These molecules are proposed to absorb in the IR region that contains the diffuse interstellar bands (DIB).[41]

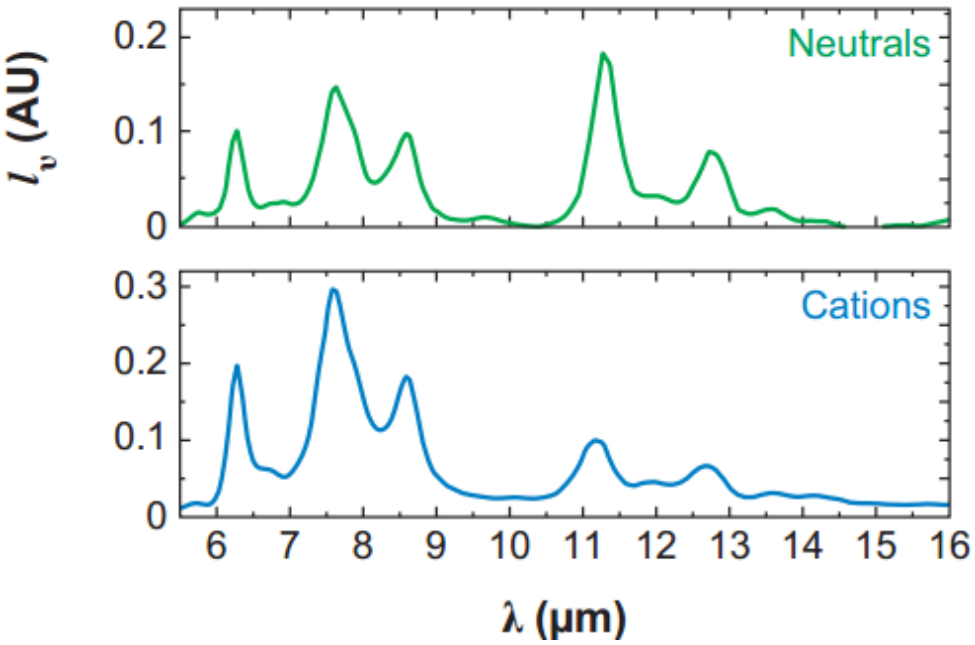

Figure 1-6: Spectra of two different types of PAHs, from the spatial spectral ISOCAM maps of NGC 7023.[37]

Finally, PAHs molecules are one of the most abundant family of species after H_2 and CO in the ISM, and thus are proposed to be a primary source of the DIBs. Also, PAHs present strong absorption of UV in two broad bands which make them good candidates for far-UV absorption. However, the far-UV absorption depends on the charge state of PAHs. [42,36] Since they are so abundant, their role in the chemistry of the ISM has been greatly speculated upon. One hypothesis is that they play a role in the catalytic formation of H_2. One of the most famous methods for formation of H_2 from PAHs contains two reaction steps:

$$PAH^+ + H \longrightarrow [PAH^+ + H] \qquad 1.1$$

$$[PAH^+ + H] + H \longrightarrow PAH^+ + H_2 \qquad 1.2$$

The first step is an H atom attached with a PAH cation by a covalent bond in the gas phase; the second hydrogen atom then extracts an H atom to produce PAH cation and forms molecular hydrogen. One of our goals in this thesis is to study the PAH ions in order to help elucide their participation in the above mechanism.[43,44] For this reason, the radical cations of natural PAH molecules are of specific interest in this study.

1.5 References

1. Lequeux, J., *The interstellar medium*. Springer Science & Business Media: 2004.
2. Hartquist, T. W.; Williams, D. A.; Williams, D. A., *The Molecular Astrophysics of Stars and Galaxies*. Oxford University Press: 1998.
3. Lequeux, J., The interstellar medium (The interstellar medium, Translation from the French language edition of: Le Milieu Interstellaire by James Lequeux, EDP Sciences, 2003 Edited by J. Lequeux. Astronomy and astrophysics library, Berlin. Springer: 2005.
4. Ehrenfreund, P.; Cami, J., Cosmic carbon chemistry: from the interstellar medium to the early Earth. *Cold Spring Harbor perspectives in biology* **2010,** *2* (12), a002097.
5. Maciel, W. J.; Roos, M. S., *Astrophysics of the interstellar medium*. Springer: 2013.
6. Williams, D. A.; Viti, S., 4Recent progress in astrochemistry. *Annual Reports Section" C"(Physical Chemistry)* **2002,** *98*, 87-120.
7. Sellgren, K., Aromatic hydrocarbons, diamonds, and fullerenes in interstellar space: puzzles to be solved by laboratory and theoretical astrochemistry. *Spectrochimica Acta Part A: Molecular and Biomolecular Spectroscopy* **2001,** *57* (4), 627-642.
8. van Dishoeck, E. F., *The chemistry of diffuse and dark interstellar clouds*. Oxford University Press: Oxford: 1998.
9. Snow, T. P.; McCall, B. J., Diffuse atomic and molecular clouds. *Annu. Rev. Astron. Astrophys.* **2006,** *44*, 367-414.
10. Somerville, W. B.; Crawford, I. A., Observations of molecules in diffuse interstellar clouds. *Journal of the Chemical Society, Faraday Transactions* **1993,** *89* (13), 2261-2268.
11. Viti, S.; Williams, D.; O'neill, P., Hydrocarbons in diffuse and translucent clouds. *Astronomy and Astrophysics* **2000,** *354*, 1062-1070.
12. Kaiser, R. I., Experimental investigation on the formation of carbon-bearing molecules in the interstellar medium via neutral-neutral reactions. *Chemical reviews* **2002,** *102* (5), 1309-1358.
13. Turner, B., A Common Gas-Phase Chemistry for Diffuse, Translucent, and Dense Clouds? *The Astrophysical Journal* **2000,** *542* (2), 837.
14. Charnley, S.; Ehrenfreund, P.; Kuan, Y.-J., Spectroscopic diagnostics of organic chemistry in the protostellar environment. *Spectrochimica Acta Part A: Molecular and Biomolecular Spectroscopy* **2001,** *57* (4), 685-704.
15. Ikeda, M.; Maezawa, H.; Ito, T.; Saito, G.; Sekimoto, Y.; Yamamoto, S.; Tatematsu, K. i.; Arikawa, Y.; Aso, Y.; Noguchi, T., Large-Scale Mapping Observations of the CI (3P1-3P0) and CO (J= 3-2) Lines toward the Orion A Molecular Cloud. *The Astrophysical Journal Letters* **1999,** *527* (1), L59.
16. Puget, J.; Leger, A., A new component of the interstellar matter-Small grains and large aromatic molecules. *Annual review of astronomy and astrophysics* **1989,** *27*, 161-198.
17. Snow, T. P.; Bierbaum, V. M., Ion chemistry in the interstellar medium. *Annu. Rev. Anal. Chem.* **2008,** *1*, 229-259.
18. Heger, M. L., The spectra of certain class B stars in the regions 5630A-6680A and 3280A-3380A. *Lick Observatory Bulletin* **1922,** *10*, 146-147.
19. Herbig, G. H., The diffuse interstellar bands. *Annual Review of Astronomy and Astrophysics* **1995,** *33*, 19-74.

20. Snow, T. P., The unidentified diffuse interstellar bands as evidence for large organic molecules in the interstellar medium. *Spectrochimica Acta Part A: Molecular and Biomolecular Spectroscopy* **2001,** *57* (4), 615-626.
21. Escure, C.; Leininger, T.; Lepetit, B., Ab initio study of valence and Rydberg states of CH3Br. *The Journal of chemical physics* **2009,** *130* (24), 244306.
22. Merrill, P. W., Unidentified interstellar lines. *Publications of the Astronomical Society of the Pacific* **1934,** *46*, 206-207.
23. Merrill, P. W.; Wilson, O. C., Unidentified interstellar lines in the yellow and red. *The Astrophysical Journal* **1938,** *87*, 9.
24. Crawford, M.; Tielens, A.; Allamandola, L., Ionized polycyclic aromatic hydrocarbons and the diffuse interstellar bands. *The Astrophysical Journal* **1985,** *293*, L45-L48.
25. Fortenberry, R. C., Singlet excited states of anions with higher main group elements. *Molecular Physics* **2013,** *111* (21), 3265-3275.
26. Fortenberry, R. C.; Crawford, T. D., Theoretical prediction of new dipole-bound singlet states for anions of interstellar interest. *The Journal of chemical physics* **2011,** *134* (15), 154304.
27. Grein, F., The ClO4 radical: a theoretical study on ground and excited states. *Molecular Physics* **2009,** *107* (19), 2005-2013.
28. Le Page, V.; Snow, T. P.; Bierbaum, V. M., Hydrogenation and charge states of PAHs in diffuse clouds. I. Development of a model. *The Astrophysical Journal Supplement Series* **2001,** *132* (2), 233.
29. Le Page, V.; Snow, T. P.; Bierbaum, V. M., Hydrogenation and charge states of polycyclic aromatic hydrocarbons in diffuse clouds. II. Results. *The Astrophysical Journal* **2003,** *584* (1), 316.
30. Maier, J. P.; Walker, G. A.; Bohlender, D. A., On the possible role of carbon chains as carriers of diffuse interstellar bands. *The Astrophysical Journal* **2004,** *602* (1), 286.
31. Ruiterkamp, R.; Cox, N.; Spaans, M.; Kaper, L.; Foing, B.; Salama, F.; Ehrenfreund, P., PAH charge state distribution and DIB carriers: Implications from the line of sight toward HD 147889. *Astronomy & Astrophysics* **2005,** *432* (2), 515-529.
32. Ruiterkamp, R.; Halasinski, T.; Salama, F.; Foing, B.; Allamandola, L.; Schmidt, W.; Ehrenfreund, P., Spectroscopy of large PAHs-Laboratory studies and comparison to the diffuse interstellar bands. *Astronomy & Astrophysics* **2002,** *390* (3), 1153-1170.
33. Salama, F.; Galazutdinov, G.; Krełowski, J.; Allamandola, L.; Musaev, F., Polycyclic aromatic hydrocarbons and the diffuse interstellar bands: A survey. *The Astrophysical Journal* **1999,** *526* (1), 265.
34. Allamandola, L.; Tielens, A.; Barker, J., Interstellar polycyclic aromatic hydrocarbons-The infrared emission bands, the excitation/emission mechanism, and the astrophysical implications. *The Astrophysical Journal Supplement Series* **1989,** *71*, 733-775.
35. Leger, A.; D'Hendecourt, L.; Boccara, N., Book Review: Polycyclic aromatic hydrocarbons and astrophysics./Reidel, 1986. *The Observatory* **1987,** *107*, 168.
36. Tielens, A. G., *The physics and chemistry of the interstellar medium*. Cambridge University Press: 2005.
37. Tielens, A. G., Interstellar polycyclic aromatic hydrocarbon molecules*. *Annu. Rev. Astron. Astrophys.* **2008,** *46*, 289-337.
38. Hammer, N. I.; Hinde, R. J.; Compton, R. N.; Diri, K.; Jordan, K. D.; Radisic, D.; Stokes, S. T.; Bowen, K. H., Dipole-bound anions of highly polar molecules: Ethylene carbonate and vinylene carbonate. *Journal of Chemical Physics* **2004,** *120* (2), 685-690.
39. Bauschlicher Jr, C. W., The Infrared Spectra of C96H24, C96H24+, and C96H25+. *The Astrophysical Journal* **2002,** *564* (2), 782.
40. Kaneda, H.; Onaka, T.; Sakon, I.; Kitayama, T.; Okada, Y.; Suzuki, T., Properties of polycyclic aromatic hydrocarbons in local elliptical galaxies revealed by the Infrared Spectrograph on Spitzer. *The Astrophysical Journal* **2008,** *684* (1), 270.

41. Li, A.; Draine, B., Infrared emission from interstellar dust. II. The diffuse interstellar medium. *The Astrophysical Journal* **2001,** *554* (2), 778.
42. Verstraete, L., The role of PAHs in the physics of the interstellar medium. *EAS Publications Series* **2011,** *46*, 415-426.
43. Bierbaum, V.; Le Page, V.; Snow, T., PAHs and the Chemistry of the ISM. *EAS Publications Series* **2011,** *46*, 427-440.
44. Boschman, L.; Cazaux, S.; Spaans, M.; Hoekstra, R.; Schlathölter, T., H2 formation on PAHs in photodissociation regions: a high-temperature pathway to molecular hydrogen. *Astronomy & Astrophysics* **2015,** *579*, A72.

45. Cold - University of Oregon.http://abyss.uoregon.edu/~js/ast122/lectures/lec22.html

Chapter 2. Experimental Methods

2.1 Mass Spectrometry Methods

Mass spectrometry (MS) is an analytical technique that can analyze qualitatively and quantitatively chemical samples by measuring the mass-to-charge ratio (m/z) and abundance of gas-phase ions. MS has an enormous number of applications including industrial processing, environmental monitoring, food and drug quality control, identifying unknown substances, healthcare, characterization of proteins and biomolecules, space exploration and drug testing in athletes.[1,2] Mass spectrometry is based on the generation of gas-phase ions from a sample in the ion source of the instrument, and then isolating and characterizing these ions using an analyzer. Since the resolution of modern mass spectrometers is quite good, it is generally possible to separate out the individual naturally occuring isotopes for a given ion elemental composition. High resolution coupled with calibration (accurate mass) can reveal the exact mass of an ion, defining its elemental composition uniquely.[3] Also, fragmenting an ion can confirm the molecule's identity in the mass spectrum.[2]

All mass spectrometer instruments consists of five main components: sample inlet, an ion source (produces ions in the gas phase), a mass analyzer (separates ions based on their the m/z ratio), a detector (measures the ion abundance), and a data system, fig. 2.1 .[2] A picture of the

Micromass Quattro-LC triple-quadrupole mass spectrometer used in this thesis is shown in fig. 2.2.

Figure 2-1:Schematic views of mass spectrometry.

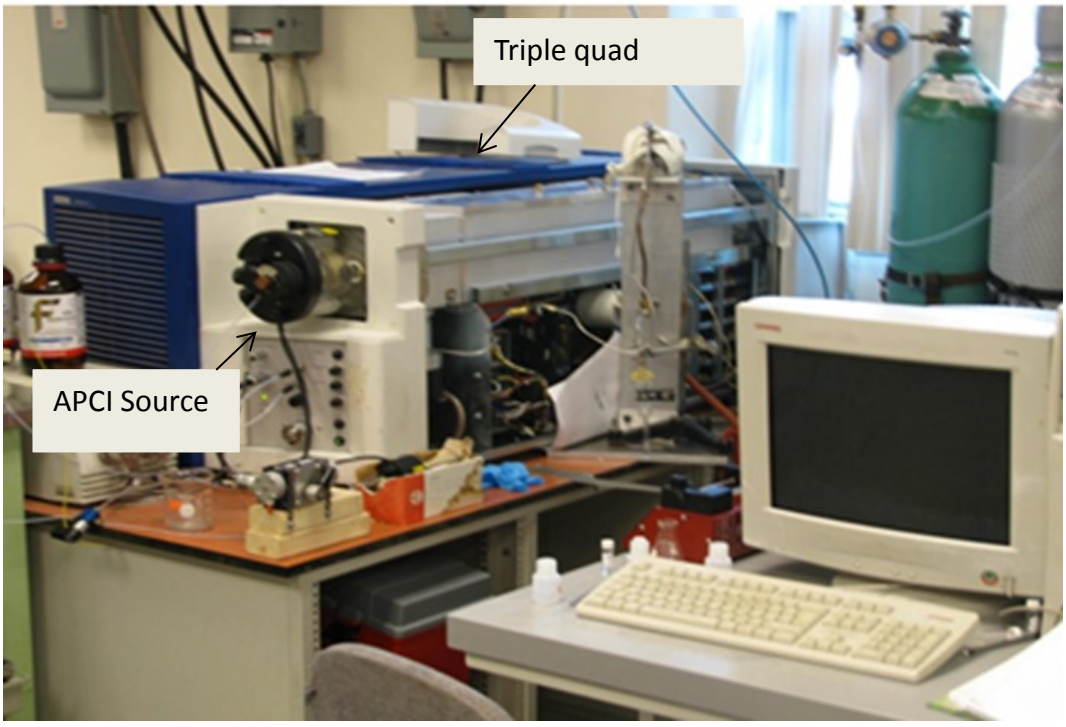

Figure 2-2:view of of Micromass Quattro-LC triple-quadrupole mass spectrometer.

2.2 Atmospheric Pressure Chemical Ionization (APCI)

APCI is an ionization technique that uses gas-phase ion–molecule reactions at atmospheric pressure and is typically employed for non-polar compounds.[4] It is related to its sister technique, electrospray, in that analyte molecules are dissolved in solution and passed through a capillary inlet. Unlike electrospray, the inlet is heated to volatolize solvent and the analyte. A corona discharge is produced at a needle held at high voltage, and this discharge ionizes solvent molecules which then react with the analyte molecules.

APCI is mostly used to study non-polar compounds with reasonable molecular weight up to around 1500 Da and yields primarily singly-chanrged ions. The schematic view of an APCI source is shown in fig.2.3.

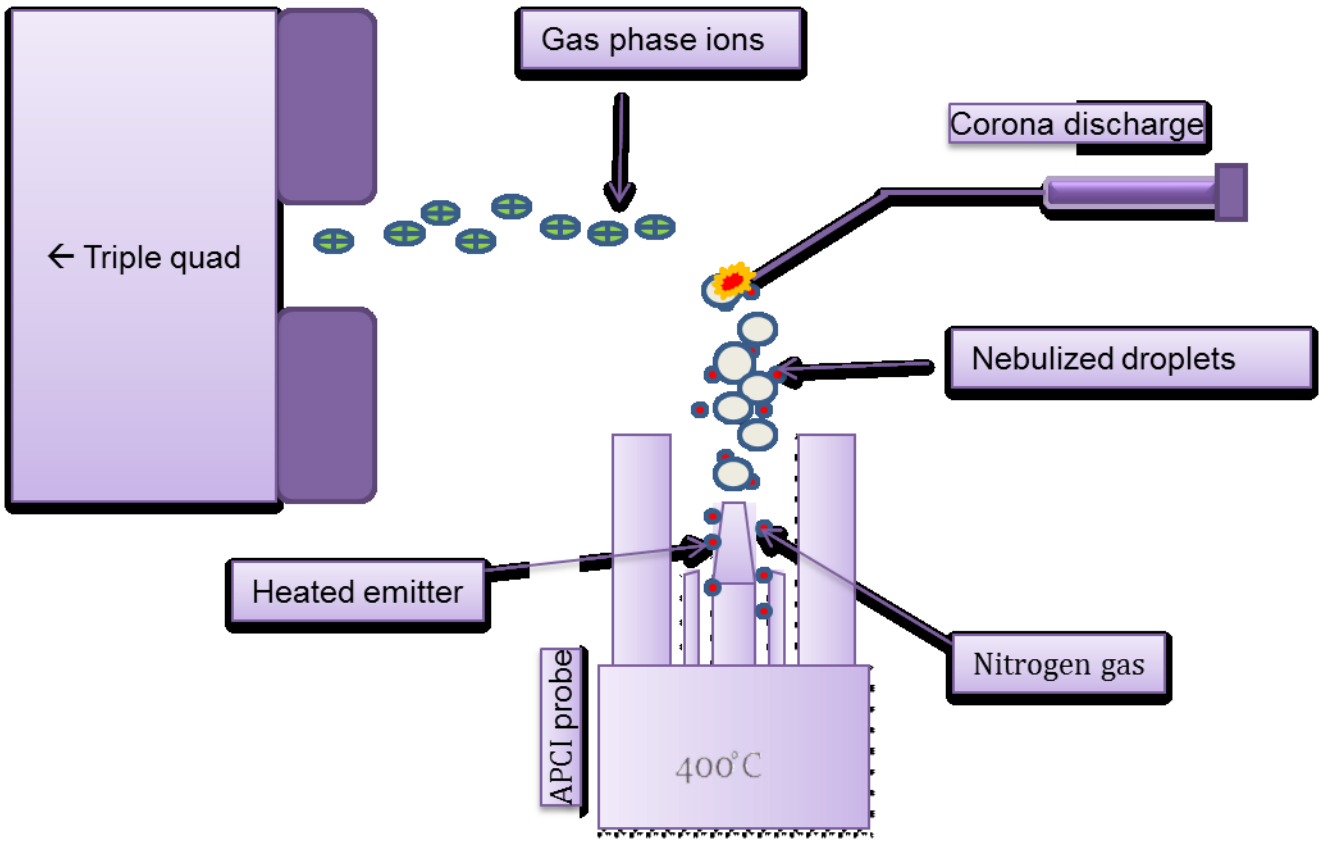

Figure 2-3: Schematic views of the APCI source

Specifically, the experimental conditions employed in this thesis are as follows. The analyte was dissolved in chloroform and introduced into the APCI probe at a flow rate between 0.3 and 0.5 ml/min. The solution is directly introduced into a pneumatic nebulizer where it is converted into a thin fog by a high temperature nitrogen gas stream. These droplets are displaced via the gas flow through a heated tube called a vaporization chamber.[5] The heat transferred to the droplets drives the evaporation of the solvent and the sample in the gas flow. After desolvation, they are passed through a corona discharge electrode where ionization happens. In this thesis, analyte molecules were ionized by charge exchange with solvent ions to produce radical cations of the PAH molecules in question. Chloroform has been shown to increase

ionization by charge transfer as the gas-phase acidity is very high, resulting in little to no proton transfer.

Since ions are generated at atmospheric pressure, they undergo many thermalizing collisions with nitrogen and solvent molecules prior to entering the mass spectrometer, which should produce ions with a thermal internal energy distribution. This will be significant later on when the modeling of the experimental data is discussed.

2.3 Mass analysis

2.3.1 Quadrupole Mass Filter

Once the ions enter the mass spectrometer through the sampling cone, they are subjected to mass analysis by the first quadrupole mass filter. In this way, the desired m/z ratio, corresponding to the molecular ion of interest, can be selected and passed along to the collision cell for MS/MS experiments.[6] The quadrupole filter is made from four parallel metal rods (the rods are normally around 5 to15 mm in diameter and 10 cm long) fig. 2-4. [1,7]

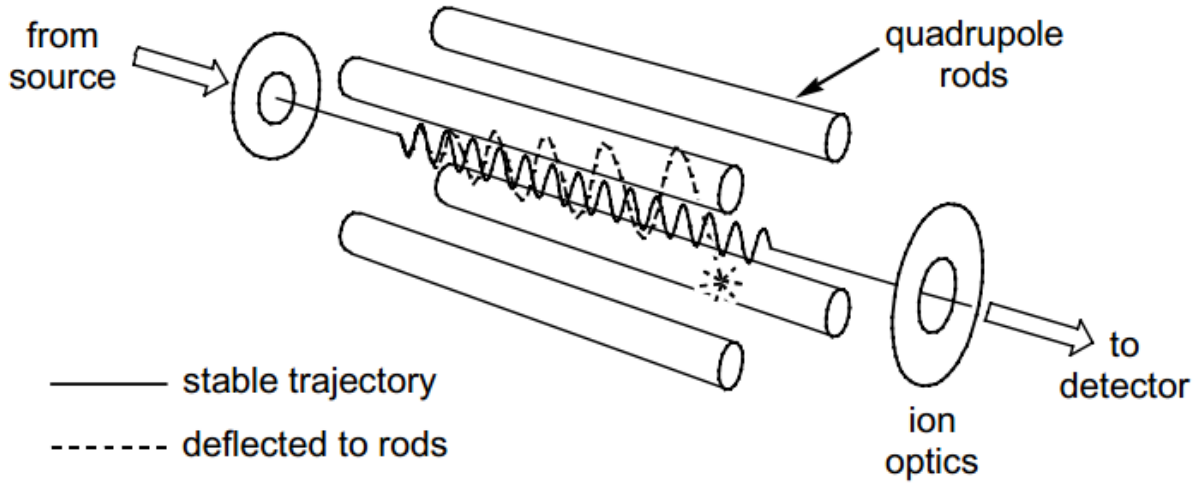

Figure 2-4: schematic of quadrupole mass analyser. [1]

The four rods have alternating potential and polarity.[3] The voltage applied to each pair of opposing rods consists of a direct current (DC), and radio frequency (RF). The latter produces a rapid alternation of the polarity on the rods, effectively trapping the ion motion in two dimensions as they travel through the filter.[2] The superposition of the DC voltage means that only one ion m/z ratio will have a stable trajectory thorugh the rods at any one value of the voltage, thus permitting the filter to behave as a mass spectrometer.

2.3.2 MS/MS

Yost and Enke developed the triple quadrupole mass spectrometer at the end of the 1970s.[8] The first design contained two quadrupole mass analysers that were separated by a quadrupole collision cell in RF–only mode (no DC potential, and thus all ions have stable trajectories through this set of rods). [8,9,10] An APCI source was used in this project. The three quadrupoles

are named as Q1, q2, and Q3 respectively from the ion source to the detector[5], and are shown in fig. 2.5.

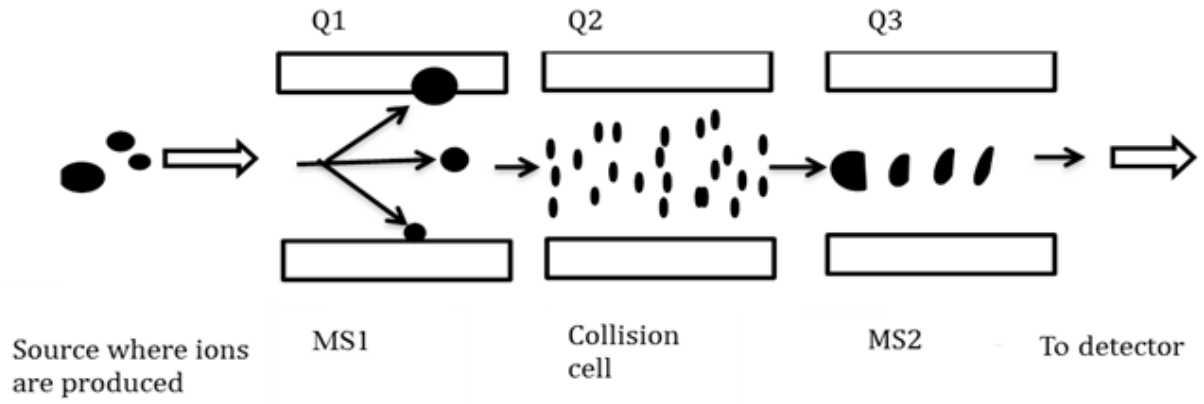

Figure 2-5: Schematic of product ion scan. Different ions come in MS 1 but only specific ions (m/z value) are permitted to enter the collision cell and fragment ions are scanned in MS 2. [1]

In order to improve the 2-D trapping in the central quadrupole, the Micromass Quattro-LC employs a hexapole instead (though the instrument is still referred to as a triple-quadrupole mass spectrometer). To perform tandem mass spectrometry (MS/MS), the desired ion (parent ion) is selected by its m/z ratio by Q1 and transmitted to the collision hexapole. An inert gas (typically argon) is introduced into the collision cell. Collisions take place between the ion and gas at variable lab frame collision energies which serve to increase the internal energy of the ions and promote fragmentation; this is called collision induced dissociation (CID).[10] The fragment ions are analysed by scanning Q3 over the desired m/z range. For example, fig. 2.6 shows the MS/MS mass spectrum of naphthalene ions (m/z 128). In this spectrum the parent

radical cation of naphthalene (m/z 128) was the mass selected and subjected to CID. The fragment ions obtained from naphthalene occur at m/z 127, 126, 102, and 78.

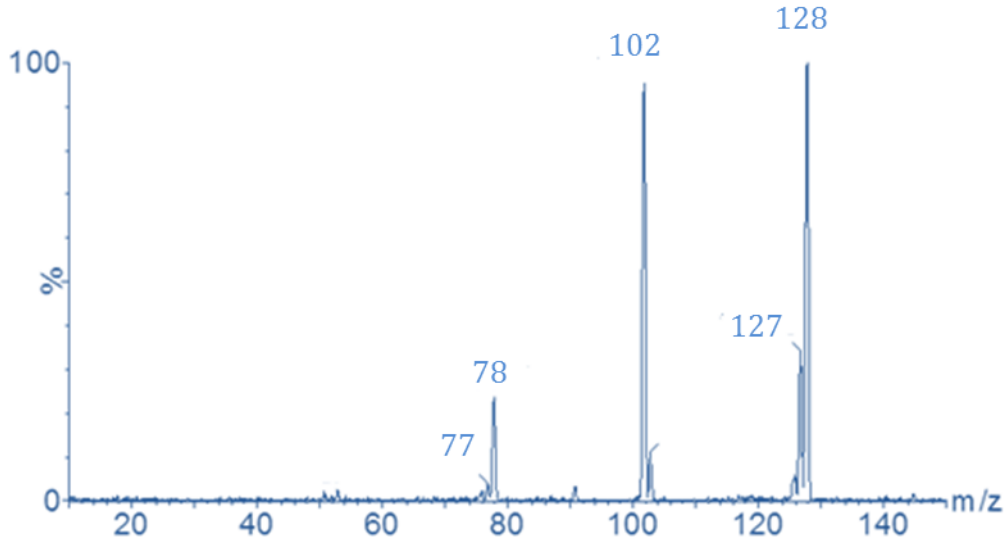

Figure 2-6: The MS/MS mass spectrum of naphthalene ions.

2.3.2 Obtaining a breakdown diagram

In the ion-target gas collision ion, translational energy of the ion is transformed into internal energy. The kinetic energy of the ion as determined by the voltage with which they are moved through the collision cell, and is called the laboratory frame collision energy (E_{lab}). Only a fraction of this collision energy is available to be converted to internal energy, depending on the relative masses of the ion and target.[11,12,13] Thus, we define the center of mass collision energy (E_{com}) as the maximum kinetic energy available to be transferred into the internal energy of ions from a single collision:

$$E_{com} = E_{lab} \frac{m_c}{m_c+m_i}$$ Equation 2.1

where m_c is a mass of the collision gas atom (argon), and m_i is a mass of the ion. Thus, by changing E_{lab}, the dissociation of an ion can be investigated as a function of its internal energy (by the virtue of changing E_{com}). In this thesis, the dissociation of the PAH ions were probed as a function of E_{com} to produce what is referred to as a breakdown diagram (a plot of the relative abundance of parent and products ions at each E_{com}). This is then the data that will be theoretically modeled.

2.4 Computational Methods

2.4.1 Ion structure calculations

Equilibrium ion structures and subsequent calculation of harmonic vibrational frequencies were calculated at the B3LYP/6-311G(d,p) level of theory with the Gaussian 09 suite of programs.[14] The optimization calculations are to find a low energy structure via finding a minimum in the potential energy surface for that structure. When the calculation is finished, the calculated vibrational frequencies tell if the obtained structure is an equilibrium structure (all frequencies positive) or an n-order saddlepoint (n frequencies negative).[15]

2.4.2 Density Function Theory

Density functional theory (DFT) is a popular computational method. The main idea of DFT is to calculate the electron density of molecule, ρ, and the electronic energy from ρ, without calculating the wavefunction.[16] Irrespective of the molecule size, the DFT calculations of the ground state electron density only depend on three variables ρ(x, y, z) while ab initio methods based on the Schrödinger equation scale with 3N (where N = number of electrons) which rapidly become computationally intensive as molecular size increases.[17,18] For the study of PAH molecules, the selected DFT functional was the B3LYP (Becke, three-parameter, Lee-Yang-Parr functional) method of theory because this method had been proven to be very exact in geometry computation. The basis set employed was the 6-311+G(d,p) basis set.

In order to compare the calculated energies of species, it is necessary to combine the calculated total electronic energy with the zero-point vibrational energy obtained from the vibrational frequency calculation:[19]

$$E_{0K} = \text{electronic} + \text{ZPE} \qquad \text{Equation 2.2}$$

These calculated vibrational frequencies are also used in Rice-Ramsperger-Kassel-Marcus (RRKM) theory to calculate unimolecular reaction rate constants that we need to model the experimental breakdown diagrams.

2.4.3 Rice – Ramsperger-Kassel- Marcus (RRKM) theory

The RRKM theory is commonly used to calculate the unimolecular dissociation rate constant . Lindemann was the first to successfully illustrate the mechanism for a unimolecular reaction at high pressures in 1922. The Lindemann mechanism is shown below[20]

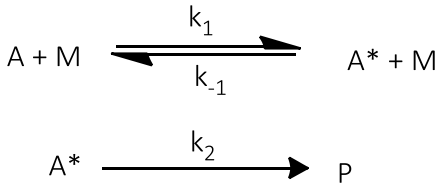

In the low pressure limit, this mechanism fails to predict unimolecular decay rate constants due to the absence of activating collisions. In 1927-1928, Rice, Ramsperger, and Kassel [21,22,23,24] developed the Lindemann mechanism further to read as

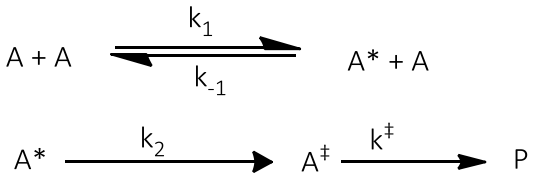

Where $A^{‡}$ is the transition state of the unimolecular reaction. This theory is named RRK theory, which assumes that the internal energy needs to be focussed into one vibrational mode for the reaction to occur, and that energy can flow through all oscillators statistically. The unimolecular reaction happens when the energy of one particular reactive mode arrives at the transition state. However, RRK theory treated all oscillators as the same, which does not accurately reflect the various modes available in a given molecule.

In 1952, Marcus developed RRK theory further by explicitly employing the distinct vibrational modes in a molecule, and the resulting theory is called RRKM theory.[25,26] The different energies employed in RRKM theory calculation are illustrated in fig. 2.7.[27]

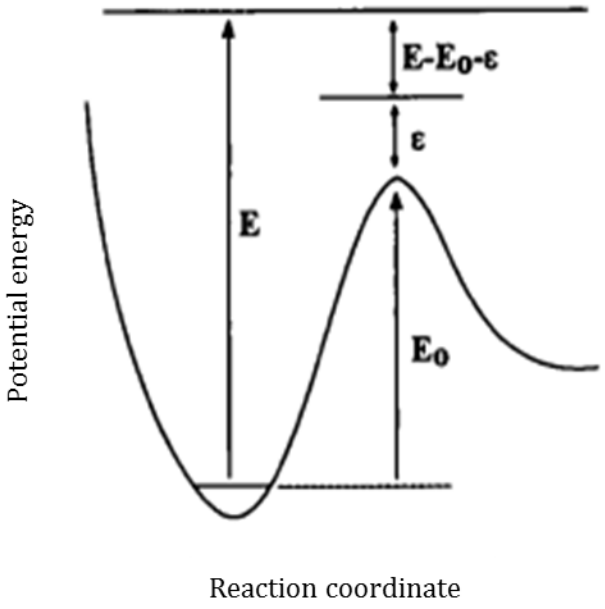

Figure 2-7: Schematic view of a reaction coordinates. [27]

E is the internal energy of reactant ion and E_0 is the 0 K activation energy for the reaction. ε is the energy of translational in the reaction coordinate. The RRKM equation that calculates the rate constant of a molecule as a function of E, (k(E)), is:

$$\mathrm{k(E)} = \frac{\sigma N^{\ddagger}(E-E_0)}{h\rho(E)} \qquad \text{Equation 2.3}$$

Where $N^{\ddagger}(E-E_0)$ is the sum of state of transition state, σ is the reaction symmetry number, h is Planck's constant, and $\rho(E)$ is the density of state of the parent ion at an internal energy

E.[27,28] $N^{\ddagger}(E - E_0)$ and $\rho(E)$ are calculated using the DFT vibrational frequencies of the ion and transition state via the direct counting algorithm described by Beyer and Swinehart.[29]

2.5 References

1. Henderson, W.; McIndoe, J. S., *Mass Spectrometry of Inorganic and Organometallic Compounds: Tools-Techniques-Tips*. John Wiley & Sons: 2005.
2. March, R. E.; Todd, J. F., A historical review of the early development of the quadrupole ion trap. *Quadrupole Ion Trap Mass Spectrometry, Volume 165, Second Edition* **2005**, 1-33.
3. Mitchell Jr, J., Applied polymer analysis and characterization: recent developments in techniques, instrumentation, problem solving. *Carl Hanser Verlag, Kolbergerstr. 22, D-8000 Munich 80, FRG, 1987. 573. 63/4 x 93/4 in* **1987**.
4. Carroll, D.; Dzidic, I.; Stillwell, R.; Haegele, K.; Horning, E., Atmospheric pressure ionization mass spectrometry. Corona discharge ion source for use in a liquid chromatograph-mass spectrometer-computer analytical system. *Analytical Chemistry* **1975,** *47* (14), 2369-2373.
5. <Mass Spectrometry Principles and Applications 3rd edition.pdf>.
6. March, R. E., An introduction to quadrupole ion trap mass spectrometry. *Journal of mass spectrometry* **1997,** *32* (4), 351-369.
7. Montaudo, G.; Lattimer, R. P., *Mass spectrometry of polymers*. CRC Press: 2001.
8. Yost, R.; Enke, C., Selected ion fragmentation with a tandem quadrupole mass spectrometer. *Journal of the American Chemical Society* **1978,** *100* (7), 2274-2275.
9. Yost, R.; Enke, C., Triple quadrupole mass spectrometry for direct mixture analysis and structure elucidation. *Analytical chemistry* **1979,** *51* (12), 1251-1264.
10. Yost, R. A.; Enke, C.; McGilvery, D.; Smith, D.; Morrison, J., High efficiency collision-induced dissociation in an rf-only quadrupole. *International Journal of Mass Spectrometry and Ion Physics* **1979,** *30* (2), 127-136.
11. Jennings, K. R., Collision-induced decompositions of aromatic molecular ions. *International Journal of Mass Spectrometry and Ion Physics* **1968,** *1* (3), 227-235.
12. Harrison, A. G.; Lin, M. S., Energy dependence of the fragmentation of the n-butylbenzene molecular ion. *International journal of mass spectrometry and ion physics* **1983,** *51* (2), 353-356.
13. Nacson, S.; Harrison, A. G., Energy transfer in collisional activation. Energy dependence of the fragmentation of n-alkylbenzene molecular ions. *International journal of mass spectrometry and ion processes* **1985,** *63* (2), 325-337.
14. Frisch, M.; Trucks, G.; Schlegel, H. B.; Scuseria, G.; Robb, M.; Cheeseman, J.; Scalmani, G.; Barone, V.; Mennucci, B.; Petersson, G., Gaussian 09. *Inc., Wallingford, CT* **2009,** *200*.
15. Frisch, A.; Nielsen, A.; Holder, A., Gaussview users manual. *Gaussian Inc., Pittsburgh, PA* **2000**.
16. Griffiths, D. J., Introduction to quantum mechanics. Englewood Cliffs, NJ: Prentice Hall: 1995.
17. Hohenberg, P.; Kohn, W., Inhomogeneous electron gas. *Physical review* **1964,** *136* (3B), B864.
18. Kohanoff, J.; Gidopoulos, N., Density functional theory: basics, new trends and applications. *Handbook of molecular physics and quantum chemistry* **2003,** *2* (Part 5), 532-568.
19. Lewars, E. G., *Computational chemistry: introduction to the theory and applications of molecular and quantum mechanics*. Springer Science & Business Media: 2010.
20. Green, N., *Comprehensive Chemical Kinetics: Unimolecular Kinetics, Part 1. The Reaction Step*. Elsevier: 2003; Vol. 39.
21. Hinshelwood, C., Quasi-Unimolecular Reactions. The Decomposition of Diethyl Ether in the Gaseous State. *Proceedings of the Royal Society of London. Series A, Containing Papers of a Mathematical and Physical Character* **1927**, 84-97.
22. Rice, O. K.; Ramsperger, H. C., Theories of unimolecular gas reactions at low pressures. *Journal of the American Chemical Society* **1927,** *49* (7), 1617-1629.

23. Kassel, L. S., Studies in homogeneous gas reactions. I. *The Journal of Physical Chemistry* **1928,** *32* (2), 225-242.
24. Kassel, L., Studies in homogeneous gas reactions. II. Introduction of quantum theory. *The Journal of Physical Chemistry* **1928,** *32* (7), 1065-1079.
25. Marcus, R.; Rice, O., The Kinetics of the Recombination of Methyl Radicals and Iodine Atoms. *The Journal of Physical Chemistry* **1951,** *55* (6), 894-908.
26. Marcus, R., Unimolecular dissociations and free radical recombination reactions. *The Journal of Chemical Physics* **1952,** *20* (3), 359-364.
27. Baercor, T.; Mayerfn, P. M., Statistical Rice-Ramsperger-Kassel-Marcus quasiequilibrium theory calculations in mass spectrometry. *Journal of the American Society for Mass Spectrometry* **1997,** *8* (2), 103-115.
28. Miller, W. H., Tunneling corrections to unimolecular rate constants, with application to formaldehyde. *Journal of the American Chemical Society* **1979,** *101* (23), 6810-6814.
29. Beyer, T.; Swinehart, D., Algorithm 448: number of multiply-restricted partitions. *Communications of the ACM* **1973,** *16* (6), 379.

Chapter 3 Experimental Procedures

3.1 Materials

All molecules (NAP, ANT, PHN, PYR, PER, COR, DHN, DHP, FLU, FLN, CYC, and ACE) were purchased from Sigma-Aldrich (Sigma-Aldrich, Oakville, Canada), and the chloroform (C298-1) was obtained from Fisher Scientific (Fair Lawn, New Jersey, USA). All samples of PAHs molecule were prepared by dissolving 0.1 mg from the molecule in 1 ml of pure chloroform.

3.2 APCI-MS experiment

An atmosphere pressure chemical ionization experiments of PAHs molecules were all run on the Micromass Quattro-LC triple-quadrupole mass spectrometer using the Masslynx V4.1 software under the same experiment conditions at the University of Ottawa. Prior to all experiments, the inlet was cleaned with a formic acid solution (10% formic acid, 90% distilled water). Also, the corona and sampling cone voltages were optimized to get the highest intensity for the target ion. For example, the cone and corona were optimized for the naphthalene molecule as shown in fig. 3.1a,b, respectively.

(a)

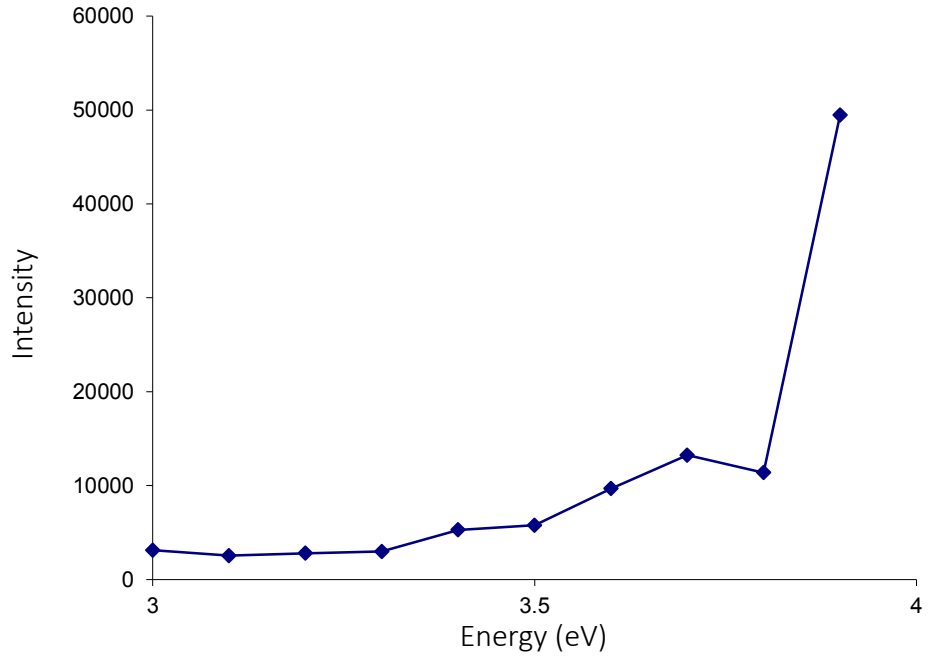

(b)

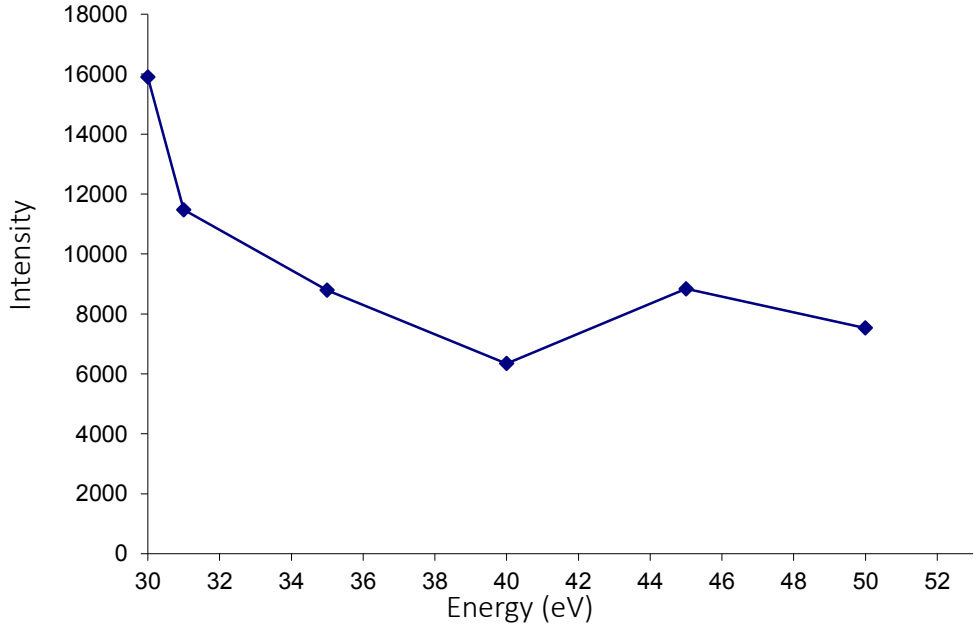

Figure 3-5:(a) Corona voltage optimization and (b) Sampling cone voltage optimization.

Sample solutions were injected into the inlet by syringe 5µl for each injection, and the flow was 0.3 ml/min in positive ionization mode. The corona was used from 3.4 to 3.9 kV independent on the optimization for the molecule while cone and extractor were constant at 30 V and 27 V consecutive. The source block temperature was 150° C and APCI probe temperature was 350-400° C. Also, the pressure of the desolvation gas (nitrogen gas) used was set at 95 psi. The first LM and HM resolution quadrupole were set in the Masslynx software to produce a resolution that yielded baseline separation of the isotopic ions in the mass spectrum. The experimental conditions are summarized in table 3.1.

Table 3.1: Optimized values for corona, first quadrupole resolution, and probe temperature.

Molecule	Corona (Kv)	Q1	Probe temperature,° C
NAP	3.5	17	400
DHN	4	15	350
DHP	4	15	350
ACE	4	17	400
FLU-H	3.92	15	400
ANT	3.4	17	400
PHN	3.4	17	400
CYC	3.82	19	400
PRY	3	17	400
FLN	3.9	19.9	400
PER	3.2	17	400
COR	3.9	15	400

3.3 APCI-MS/MS experiments.

All CID experiments were run in q2 of Micromass Quattro-LC triple-quadrupole mass spectrometer instrument with atmospheric pressure chemical ionization in positive mode. Twelve MS/MS experiments were done in this thesis, and below is a summary of the conditions used.

a) NAP radical cation, was selected mass at m/z 127.8 with second LM and HM resolution quadrupole were constant at 17 in the Masslynx software. The collision energies of CID were ranged from 5 V to 39 V.

b) DHN radical cation was selected mass at m/z 129.70 with second LM, and HM resolution quadrupole were constant at 17 in the Masslynx software. The collision energies of CID were ranged from 5V to 24 V.

c) DHP radical cation was selected mass at m/z 179.89 with second LM, and HM resolution quadrupole were constant at 17 in the Masslynx software. The collision energies of CID were ranged from 3V to 33 V.

d) ACE radical cation, was selected mass at m/z 151.87 with second LM, and HM resolution quadrupole were constant at 17 in the Masslynx software. The collision energies of CID were ranged from 5V to 42 V.

e) FLU $(M-H)^+$, was selected mass at m/z 164.85 with second LM, and HM resolution quadrupole were constant at 15 in the Masslynx software. The collision energies of CID were ranged from 1V to 45 V.

f) ANT radical cation was selected mass at m/z 177.8 with second LM, and HM resolution quadrupole were constant at 17 in the Masslynx software. The collision energies of CID were ranged from 5 V to 50 V.

g) PHN radical cation was selected mass at m/z 177.8 with second LM, and HM resolution quadrupole were constant at 17 in the Masslynx software. The collision energies of CID were ranged from 1V to 46 V.

h) CYC radical cation was selected mass at m/z 189.9with second LM, and HM resolution quadrupole were constant at 15 in the Masslynx software. The collision energies of CID were ranged from 5V to 45 V.

i) PYR radical cation was selected mass at m/z 201.88 with second LM, and HM resolution quadrupole were constant at 17 in the Masslynx software. The collision energies of CID were ranged from 5V to 49 V.

j) FLN radical cation was selected mass at m/z 201.87 with second LM, and HM resolution quadrupole were constant at 18 in the Masslynx software. The collision energies of CID were ranged from 5V to 50 V.

k) PER radical cation, was selected mass at m/z 251.96 with second LM, and HM resolution quadrupole were constant at 17 in the Masslynx software. The collision energies of CID were ranged from 5V to 51 V.

l) CON radical cation, was selected mass at m/z 299.85 with second LM, and HM resolution quadrupole were constant at 15 in the Masslynx software. The collision energies of CID were ranged from 5V to 57 V.

3.4 Calculations

3.4.1 RRKM Calculation

To derive the activation entropy ($\Delta S^{\ddagger}$) and the energy of activation (E_0) at 0K from the experimental breakdown curves requires the calculation of the dissociation rate constant for each channel, k(E), by using equation 2.3.[1] Vibrational and rotational information (frequencies and rotational constants) was obtained from the DFT calculation, and these values are used to calculate the density of states for the parent ions by using the Beyer-Swinehart algorithm[2]. The transition states were estimated using the harmonic vibrational frequencies of the parent ion. The vibrational mode correspondign to the reaction leading to each fragmentation product ($M^{\cdot+}$ for $[M-H]^+$, $[M-C_2H_2]^{\cdot+}$, $[M-C_4H_2]^{\cdot+}$, and $[M-2H]^{\cdot+}$) were removed to account for the coordinate of the reaction (the frequencies chosen are listed in the appendix). For example, when the parent ion loss H, the deleted vibrational mode was a C-H bond stretching mode. The breakdown curve was fitted by adjusting the properties of the transition state by scaling the lowest ten frequencies by a common factor. The activation entropy ($\Delta^{\ddagger}S$) was calculated at 1000 K by the equations of standard statistical mechanics

3.4.2 Theoretical breakdown diagram fitting and APCI-CID Modelling

The theoretical breakdown diagram is calculated using two FORTRAN programs. First, the RRKM k(E) was calculated using the program “dcms.exe”. A second program, “quattro.exe” uses these k(E) values for each dissociation channel and convolutes them with experimental functions of

the reaction timescale and ion internal energy distribution to produce a theoretical breakdown curve. The RRKM k(E) for each channel is then adjusted (see 3.4.1) to arrive at a suitable fit to the experimental data. The post-collision ion internal energy distribution is modeled by chosing an initial ion temperature (T_i), and a parameter, α , that links the post-collision ion temperature, T_{eff}, to the centre-of-mass collision energy ($T_{eff} = T_i + \alpha E_{com}$).[3] The theoretical breakdown diagram can be altered by changing four parameters that included the activation energy (E_0), initial temperature (T_i), α, and the first ten frequencies of transitions that calculated the activation entropy ($\Delta^{\ddagger}S$). All these parameters are altered by hand to get the best fit of the experimental breakdown diagram that corresponds to the theoretical breakdown diagram.

The time scale in the collision cell is calculated based on the length of collision cell (10 cm) and the translational energy of ion , E_{LAB}. The centre of mass energy (E_{COM}) was calculated by using the equation below

$$E_{com} = E_{lab} \frac{m_{Ar}}{m_{Ar}+m_i} \qquad \text{Equation 3.1}$$

Where m_{Ar} and m_i are mass of argon and parent ion respectively. The post-conllision internal energy distribution of ions has relationship with effecitve temperature from this equation

$$T_{CoM} = T_i + \alpha E_{CoM} \qquad \text{Equation 3.2}$$

Where T_i is initial temperature and α is an adjustable parameters which work to get the beat fitting theortical and experimental breakdown diagram with changing them. The resulting distribution of internal energy is like function of the center-of-mass collision energy and it can be calculated by using this equation:

$$P(E, E_{COM}) = \frac{\rho(E)e^{-E/RT_{COM}}}{Q(E_{COM})} \qquad \text{Equation 3.3}$$

Where $Q(E_{COM})$ is the total partition function of vibrational frequencies at T_{COM} while $\rho(E)$ is density of states of ion. The microcanonical rate constant was calculated by using RRKM theory as previously explained above. The fraction of ions dissociating is calculated as function of internal energy is by:

$$F(E) = 1 - e^{-k(E)t} \qquad \text{Equation 3.4}$$

Where $k(E)$ is microcanonical rate constant and t is maximum time of observation. These steps are described each section of theoretical diagram then are leaded to fit with experimental breakdown diagram.

3.4.4 iPEPICO experiment and modelling

In the discussion section of this thesis, comparisons are made between the present CID experiments and the results from imaging photoelectron photoion coincidence (iPEPICO) spectrometry experiments previously carried out on the VUV beamline of the Swiss Light Source (SLS).[4] Briefly, in the iPEPICO experiments, PAHs molecules are photoionized via monochromatic synchrotron radiation. After that, ions are sent to a time-of-flight (TOF) mass spectrometer, and the the ejected electrons are extracted to an imaging multichannel plate (MCP) detector and are time and position stamped. In iPEPICO, the breakdown curves for an ion is thus produced in coincidence with threshold electrons, and thus the internal energy of the ions is well established and does not have to be approximated (as is done in the CID experiments). Details are found in a publication by West, B. et al

3.5 Reference

1. Baercor, T.; Mayerfn, P. M., Statistical Rice-Ramsperger-Kassel-Marcus quasiequilibrium theory calculations in mass spectrometry. *Journal of the American Society for Mass Spectrometry* **1997,** *8* (2), 103-115.
2. Beyer, T.; Swinehart, D., Algorithm 448: number of multiply-restricted partitions. *Communications of the ACM* **1973,** *16* (6), 379.
3. Mayer, P. M.; Martineau, E., Gas-phase binding energies for non-covalent Aβ-40 peptide/small molecule complexes from CID mass spectrometry and RRKM theory. *Physical Chemistry Chemical Physics* **2011,** *13* (11), 5178-5186.
4. West, B.; Sit, A.; Mohamed, S.; Joblin, C.; Blanchet, V.; Bodi, A.; Mayer, P. M., Dissociation of the Anthracene Radical Cation: A Comparative Look at iPEPICO and Collision-Induced Dissociation Mass Spectrometry Results. *The Journal of Physical Chemistry A* **2014,** *118* (42), 9870-9878.

Chapter 4 Results

This chapter presents the experimental CID breakdown curves for the APCI generated PAH cations and the results of the RRKM modeling of those curves.

4.1 Naphthalene

Naphthalene ($C_{10}H_8$) is the smallest molecule that is considered to be a member of the PAH family, and the fragmentation of the radical cation of naphthalene has been studied in our laboratory using imaging photoelectron-photoin coincidence (iPEPICO) spectroscopy showing H-loss, C_2H_2-loss, C_4H_2-loss and H_2-loss as the four primary channels of fragmentation.[1] Here, we re-examine the dissociation of the naphthalene radical cation by collision-induced dissociation (CID). Fig 4.1 shows the CID mass spectra of the naphthalene radical cation (m/z 127.80) at different lab-frame collision energies ranging from 5 to 39 eV. When increasing the collision energy, the abundance of the parent ion decreases as additional fragment ions are formed (eg, fig 4.1, 33 eV).

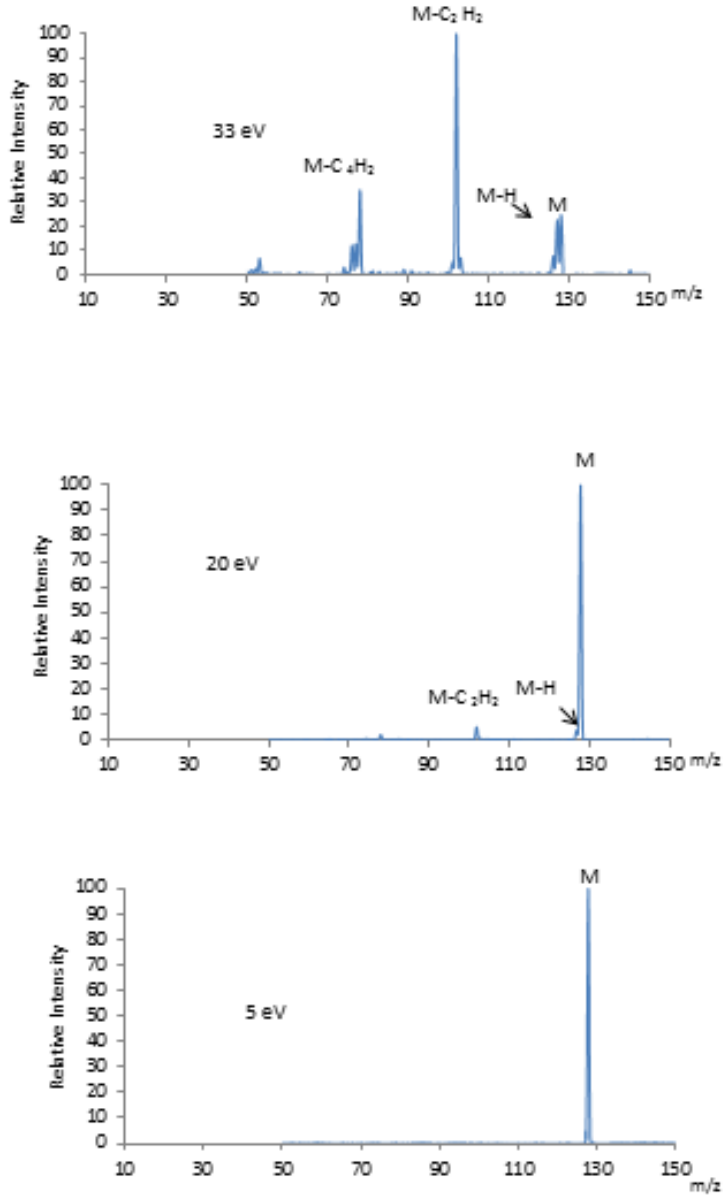

Figure 4-1:CID spectra of $C_{10}H_8^{\bullet+}$ at different lab frame collision energies. M = $C_{10}H_8^{\bullet+}$.

Four main dissociation channels are observed from the radical cation of naphthalene and these channels were similar to the channels that were obtained via iPEPICO experiments.[1] These include H and H_2 loss, and the loss of small hydrocarbons C_2H_2 and C_4H_2. Solano and Mayer

completed a detailed computational examination of the dissociation of the naphthalene radical cation, and it is summarized in fig 4.2. [2]

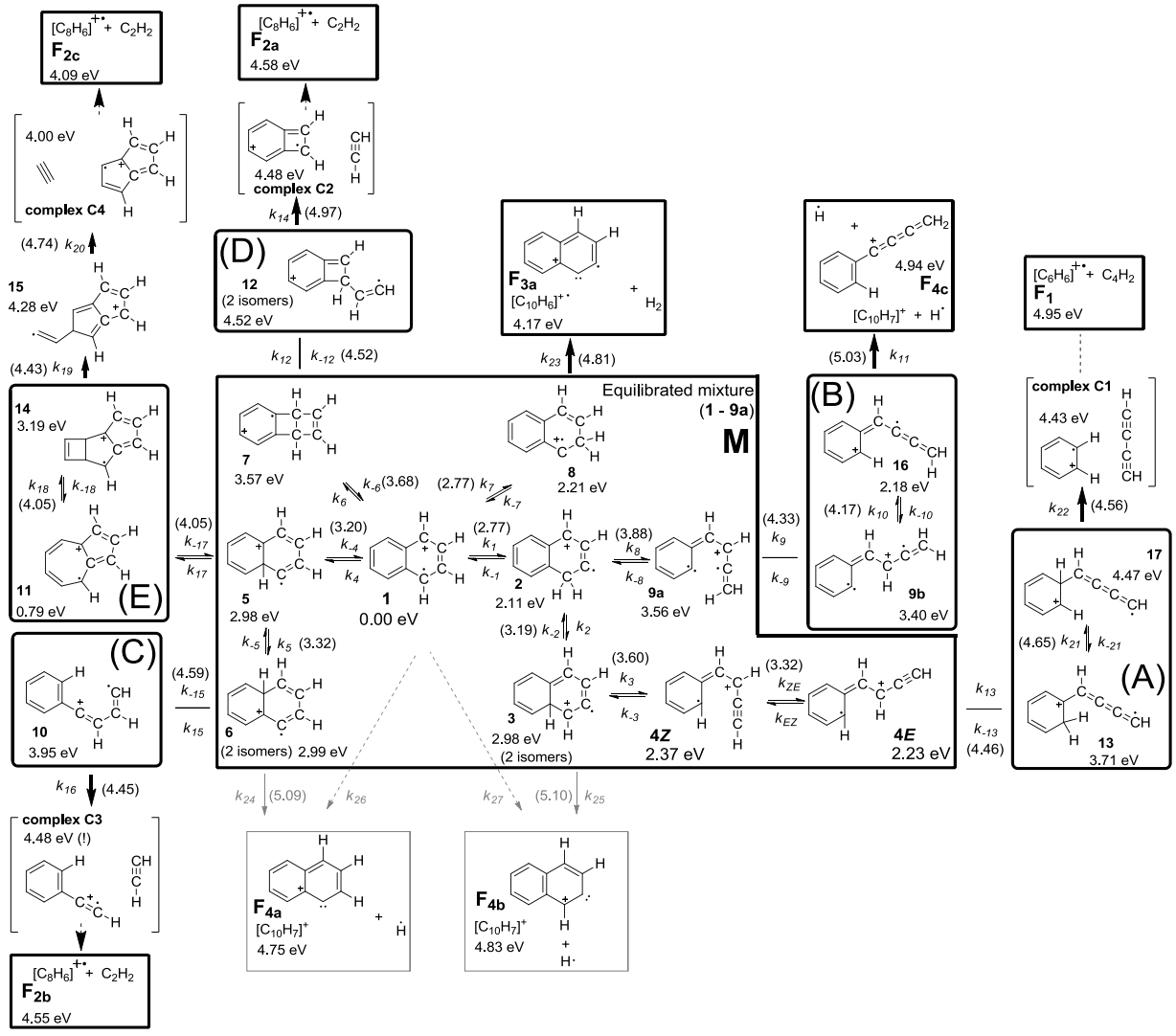

Figure 4-2:Calculated dissociation pathway of naphthalene radical cation with the most stable structures at low dissociation energies for all fragment ions pathways that calculated at the level of theory UB3LYP/6-311+G(3df,2p)//UB3LYP/6-31G(d). (Reprinted from Solano, E. A et al., 2015 with permission).[2]

Clearly even the simplest dissociation, H loss, is preceeded by extensive isomerization of the parent ion and there are numerous competing pathways for each channel. It is not in the

scope of this thesis to rigorously describe every fragmentation pathway for every ion studied, but rather, to predict the energy demand for these basic processes. Indeed, given the complexity of the potential energy surface on which this chemistry takes place, fig 4.2, only a very complex kinetic treatment, including many assumptions, can be used to relate the net experimental rate constant for a process to the surface details. Thus, we focus here on a more practical end-goal, that is to be able to predict the energy dependence of H/H_2 vs hydrocarbon loss from ionized PAHs, regardless of the structures made at the end of the day.

To this end, and to employ the RRKM equation (Eq. 2.3), symmetry numbers need to be assigned to each reaction pathway. Within the naphthalene molecule, there are many positions to form which to lose a radical H atom. It is difficult to know the missing hydrogen atom location because of hydrogen scrambling that is known to happen upon CID.[3] The difference in energy between two hydrogen atoms locations is only 0.05 eV, as calculated by Dyakov et al.[4] Based on this result, all hydrogen atoms have the same probabality of being lost.[5]As such all hydrogen locations were included as possible H-loss positions when doing RRKM calculations. The second observed fragmentation channel was C_2H_2-loss, and there are six ways possible structures that produce $C_8H_6^{\bullet+}$. The most energetically stable structure that can be produced when losing C_2H_2 from a radical naphthalene cation is the phenylacetylene radical cation.[2] C_4H_2-loss was assumed to produce the benzene cation.

The CID breakdown curve of $C_{10}H_8^{\bullet+}$ including all primary fragment ions, plotted as a function of the center-of-mass collision energy (E_{com}) (obtained from Equation 2.1) is shown in fig 4.3.

The solid lines represent the RRKM modeling of the curves. Harmonic vibrational frequencies of the naphthalene radical cation and transition states are listed in Table A.1 in the appendix . RRKM theory approximates the theoretical breakdown curve by following four parameters which can be changed manually to get the best curve fitting between the observed experimental results and theoretical reaction products, fig 4.3.

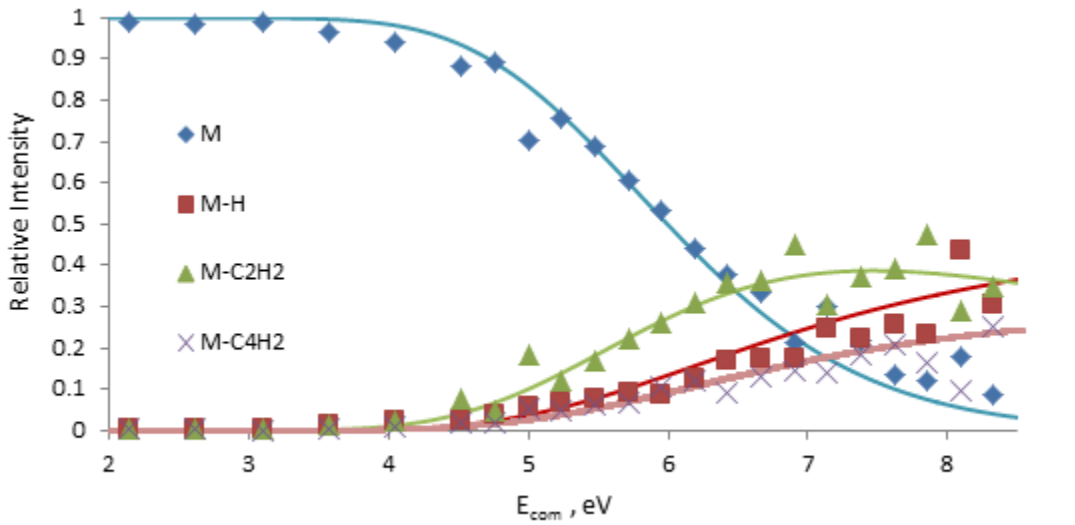

Figure 4-3: CID breakdown curves for the dissociation of the naphthalene radical cation (points) together with the RRKM modeling results (solid lines).

Table 4.1 displays the RRKM derived activation energies and entropies for the dissociation of the naphthalene radical cation. In equation 3.2, T_i and α were set to 400 K and 365 KeV^{-1}, respectively. Since increasing the collision energy resulted in H loss outcompeting C2H2 loss, the latter channel must be characterized by a reduced $\Delta^{\ddagger}S$ compared to $C_{10}H_7^+$ (Table 4.1).

Table 4.1: shows of activation energies (E_0) and entropy ($\Delta^{\ddagger}S$) for all dissociation of the naphthalene cation.

Channel	E_0 (eV)	$\Delta^{\ddagger}S_{1000k}$ (J mol^{-1} K^{-1})
M-H	4.10 ± 0.1	-6 ± 3
M-C_2H_2	3.72 ± 0.1	-15 ± 4
M-C_4H_2	4 .10 ± 0.1	4 ± 2

4.2 1,2 -dihydronaphthalene and 9,10- dihydrophenanthrene

The most abundant molecules in the interstellar medium (ISM) is H_2 because H_2 is formed on the surface of dust grains.[6,7] The current body of research has yet to determine the complex mechanisms involved, therefore research into this area is still ongoing.[8,9] PAH ions may also participate in this process, acting as surfaces in the ISM. In this part of the project, we show the results of our modeling of the dissociation of ionized 1,2-dihydronaphthalene and 9,10-dihydrophenanthrene fig4.4.

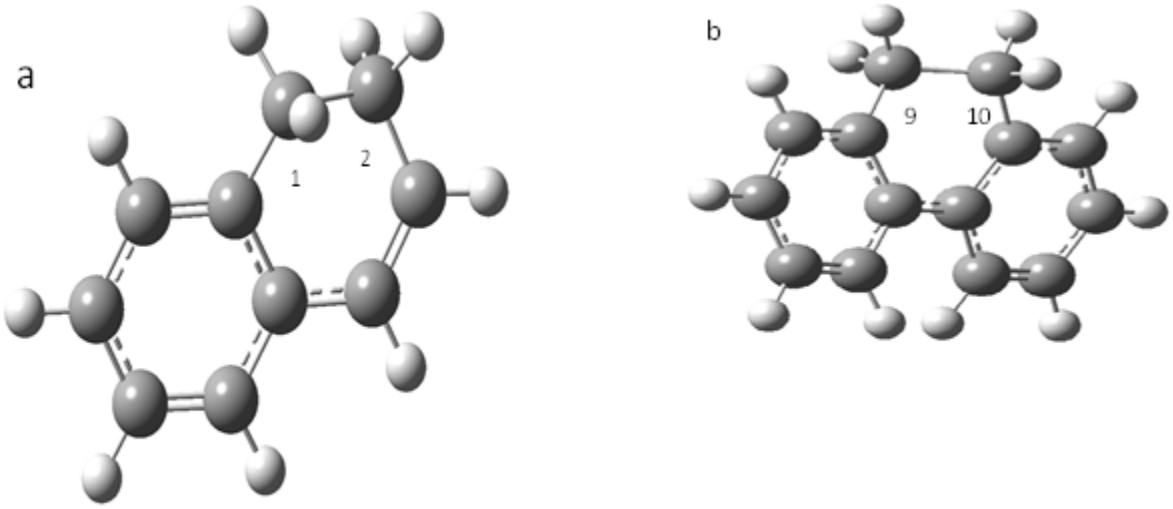

Figure 4-4:Optimized structures of a) 2,1-dihydronapthalene and b) 9,10-dihydrophenanthrene calculated at the B3LYP/6-311G++(d,p) level of theory.

The fragmentation channels for both molecules ,shown in fig 4.5 are similar and include sequential H loss and loss of a methyl radical.

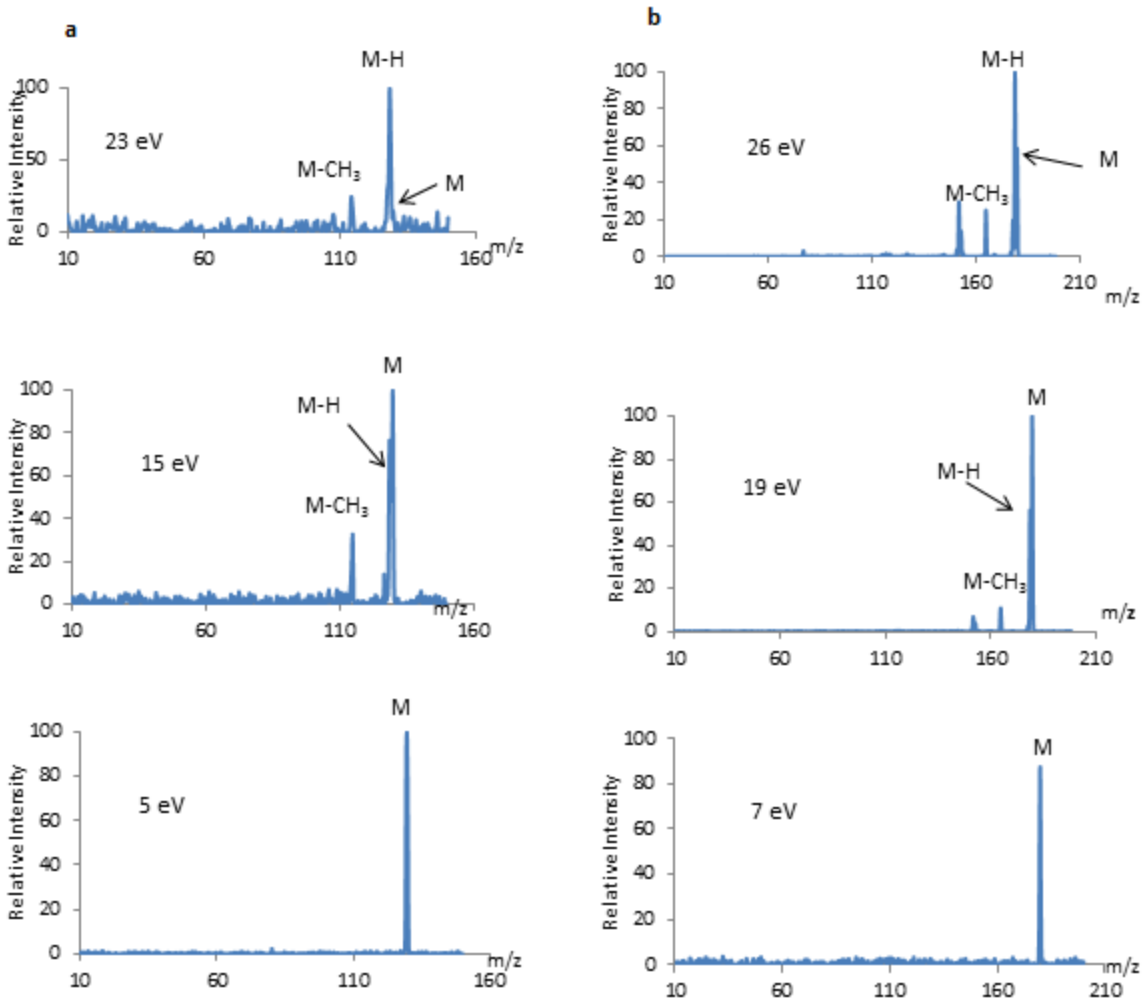

Figure 4--5: CID mass spectra at different collision energies for a) $C_{10}H_{10}^{\bullet+}$ and b) $C_{14}H_{12}^{\bullet+}$.

The primary fragments observed in CID experiments for $C_{10}H_{10}^{+\bullet}$ and $C_{14}H_{12}^{+\bullet}$ were used to create the experimental breakdown curves for these channels (in both cases, the two H atom losses were combined). The resulting breakdown diagrams, and the modeled curves are shown in fig 4.6. The modeling results are summarized in Table 4.2.

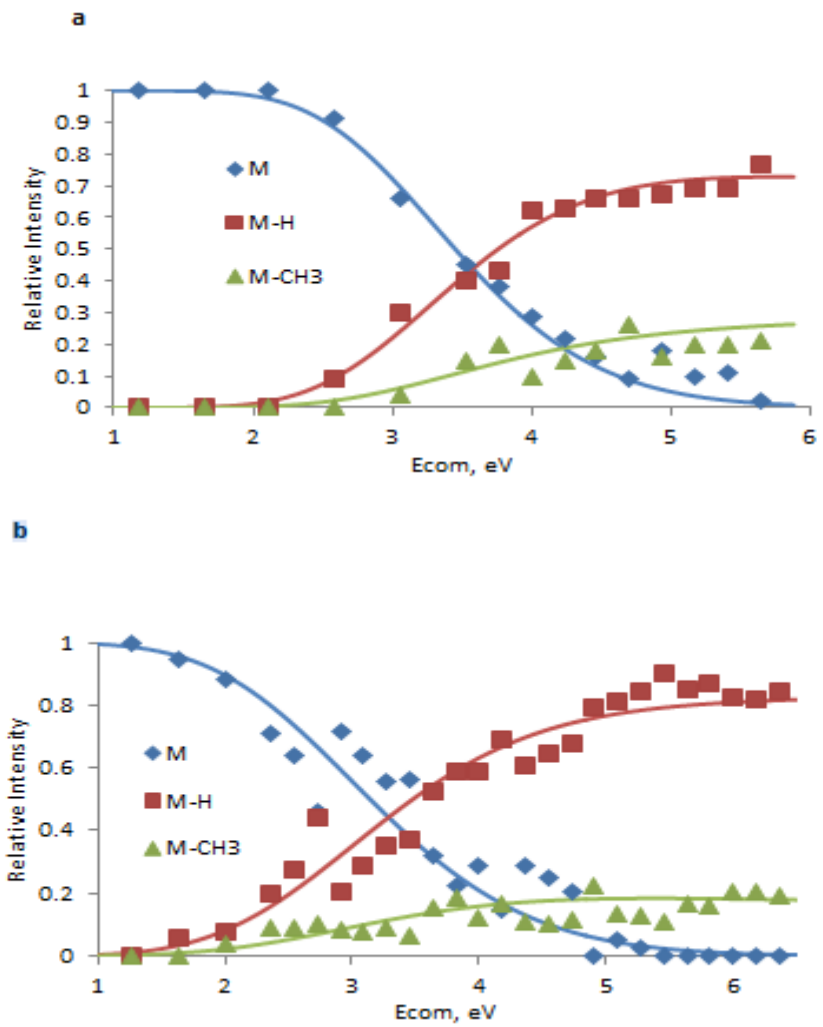

Figure 4-6: Experimental breakdown curves (points) and the results of RRKM modeling (lines) for a) dihydronaphthalene and b) dihydrophenanthrene.

The initial temperature value determined for dihydronaphthalene and dihydrophenanthrene radical cation was 550 K and 800 K respectively, while the α value was 310 KeV^{-1} and 200 KeV^{-1}, respectively.

Table 4.2 : RRKM results for the activation energy (E_0) and entropy ($\Delta^{\ddagger}S$) for all dissociation channels for ionized 1,2 dihydronaphthalene and 9,10 dihydrophenanthrene.

Channel	E_0 (eV)	$\Delta^{\ddagger}S_{1000K}$ J mol^{-1} K^{-1}
1,2-dihydronaphthalene		
M-H	2.44 ± 0.1	1 ± 5
M-CH_3	2.55 ± 0.1	11 ± 8
9,10-dihydrophenanthrene		
M-H	2.36 ± 0.1	8 ± 9
M-CH_3	2.36 ± 0.1	9 ± 6

The activation energy for hydrogen atom loss from dihydro-PAHs are lower than those observed from the fully-unsaturated PAHs because H atom loss occurs first from an sp^3-carbon.[10] West and co-workers demonstrated that CH_3 loss occurs after an isomerization reaction to the methyl-indole ion (in the case of 1,2-dihydronaphthalene) and the related methyl-substituted ion in the case of 9,10-dihydrophenanthrene.[10]

4.3 Acenaphthylene

Acenaphtylene is the most stable isomer from acetylene losses from anthracene and phenanthrene. [11] Also, it is proposed to be the product when diacetylene is lost from fluoranthene. The main fragmentation channels observed are were parallel H loss, H_2 loss, C_2H_2 loss, and C_4H_2 loss. The CID mass spectra of the acenaphthylene radical cation at different collision energies are shown in fig 4.7, together with the Igor Pro fits to the parent ion region. The experimental and theoretical breakdown curves are shown in fig 4.8, and the RRKM results are summarized in Table 4.3.

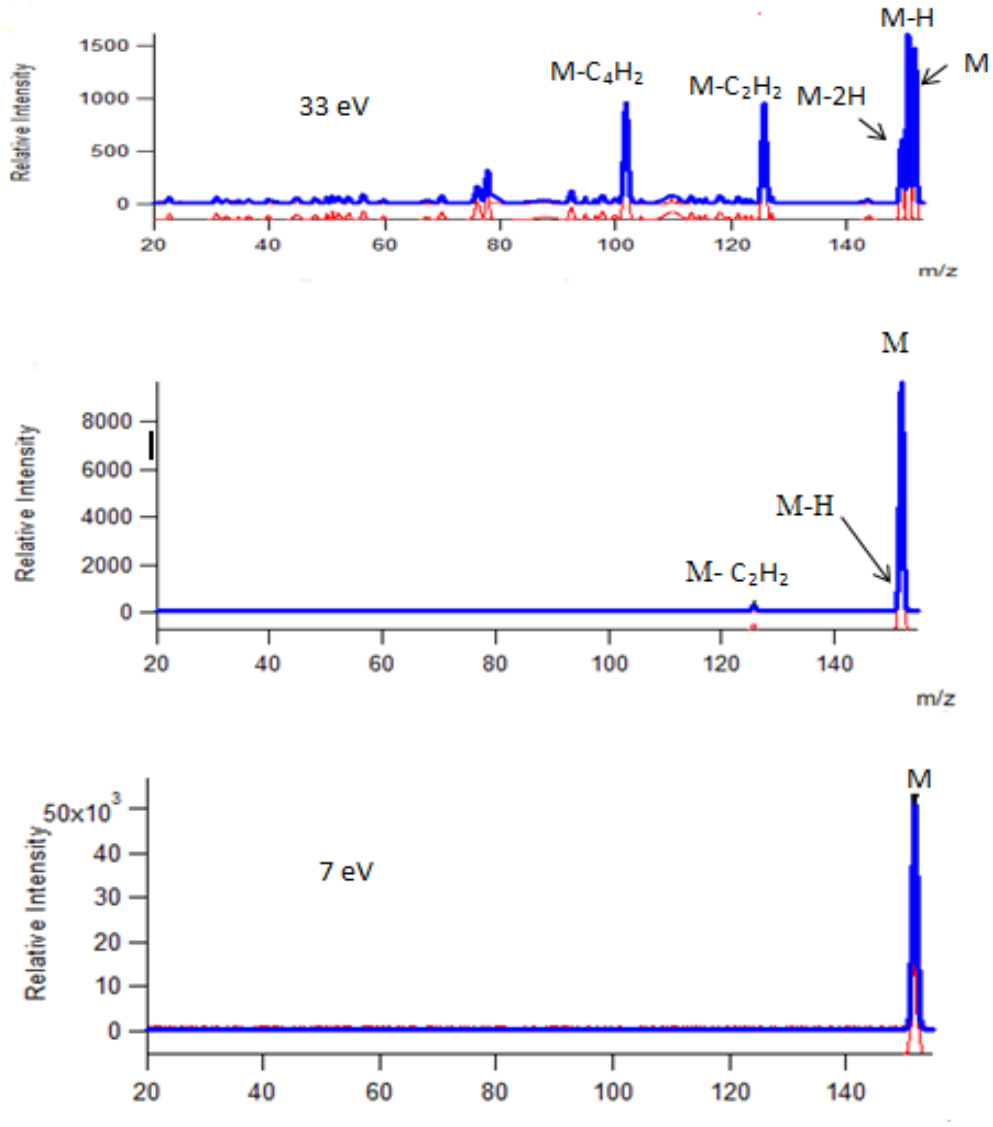

Figure 4-6:CID mass spectra of $C_{12}H_8^{\cdot+}$ ions at different collision energies, together with the Gaussian deconvolution of the peaks in the parent ion region.

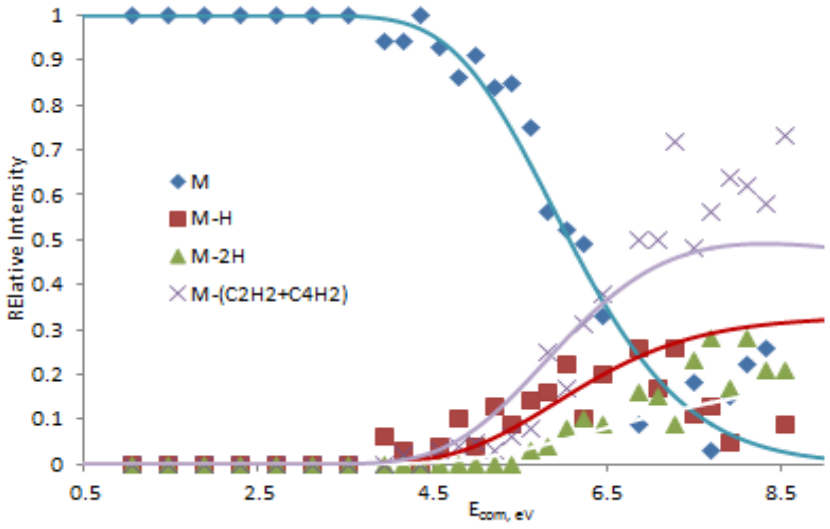

Figure 4-7:Experimental breakdown curves (points) and the results of RRKM modeling (lines) for $C12H8^{+\bullet}$ ions.

Above 7 eV, $M\text{-}H^{+}$ starts to lose (to contribute to the $M\text{-}2H^{+}$ channel) and thus the fitting is poor above the E_{com}.

Table 4.3: Summary of the activation energies (E_0) and entropies ($\Delta^{\ddagger}S$) for the dissociation of the acenaphthylene cation.

Channels	E_0 eV	$\Delta^{\ddagger}S$ $JK^{-1}mol^{-1}$
M-H	4.20 ± 0.1	14.17 ± 6
M-2H	4.32 ± 0.1	15.01 ± 5
$M\text{-}(C_2H_2 + C_4H_2)$	4.16 ± 0.1	23.91 ± 5

T_i and α set to 400K and 340 KeV^{-1} respectively

4.4 Fluorene - H

We tried many times to study the fragmentations of the fluorene radical cation but were unsuccessful in generating enough M^+ without simultaneously making $[M-H]^+$. The ^{13}C contribution of the $[M-H]^+$ peak always contributed significantly to the M+ signal, and thus any CID experiment would give overlapping results. We thus decided to study the unimolecular fragmentations of the fluorene - H cation, which was the most stable isomeric fragment ion from the loss of CH_3 from 9,10-dihydrophenanthrene .[10] This $C_{13}H_9^{+\bullet}$ ion exhibited dissociation channels similar to that of naphthalene: H loss , H_2 loss, C_2H_2 loss, and C_4H_2 loss . It was not possible to achieve baseline resolution of the precursor and H-loss product peaks in the CID mass spectra for this ion, and so the the parent ion region was first deconvoluted by using the Gaussian peak fitting algorithm in Igor Pro 6.37, illustrated in fig 4.9.

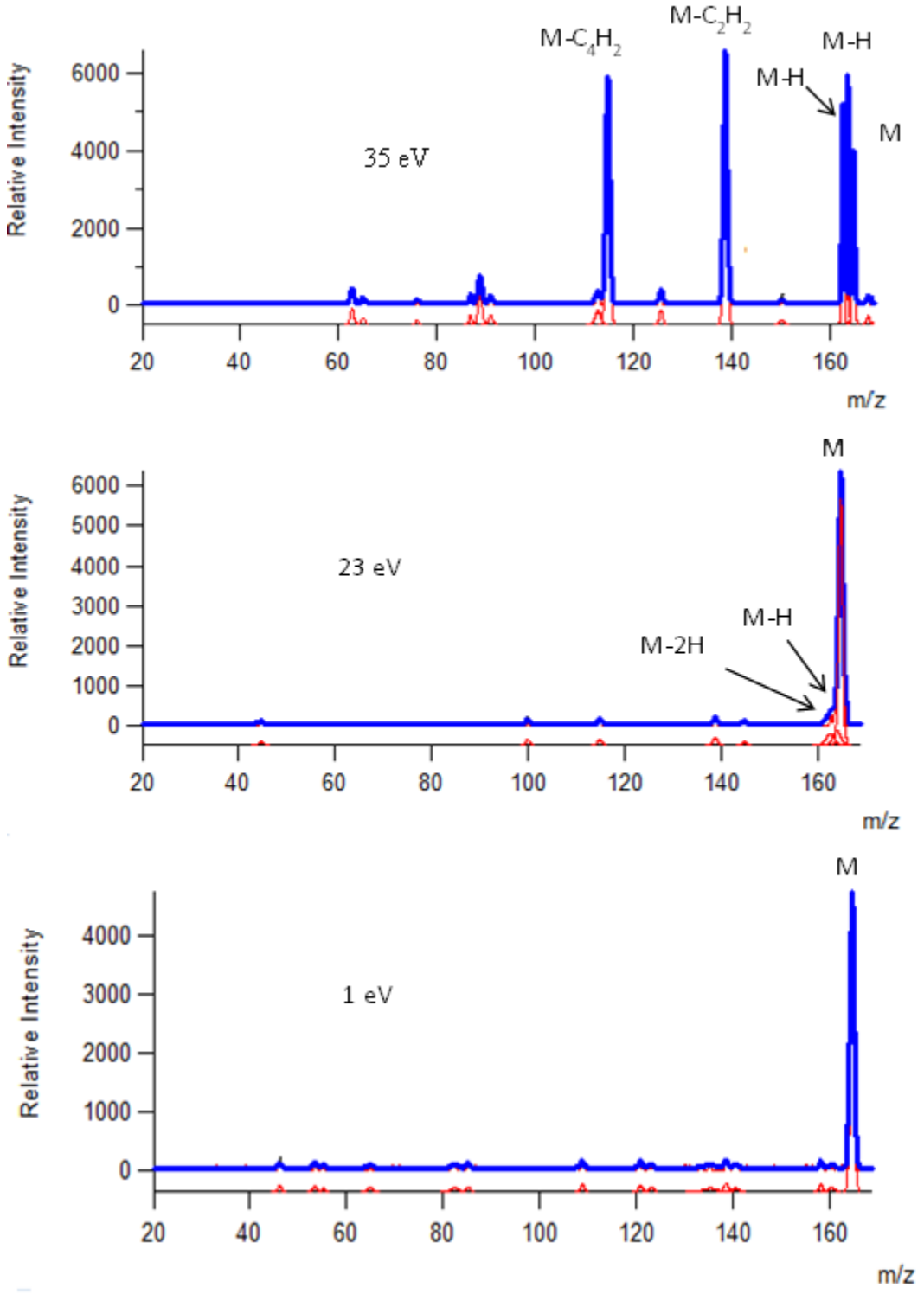

Figure 4-8:CID mass spectra of $C_{13}H_9^{\bullet+}$ ions at different collision energies, together with the Gaussian deconvolution of the peaks in the parent ion region.

The experimental breakdown curve was modelled by RRKM calculations to get the theoretical breakdown curve of fluorene-H radical cation, fig 4.10. Here again the signal intensity of the $[M-2H]^{\cdot+}$ ion was added to that of $[M-H]^+$ above an E_{com} of 6 eV because it was apparent that above this energy, the ion was the result of a sequential dissociation of the M-H ion. The RRKM results are summarized in Table 4.4.

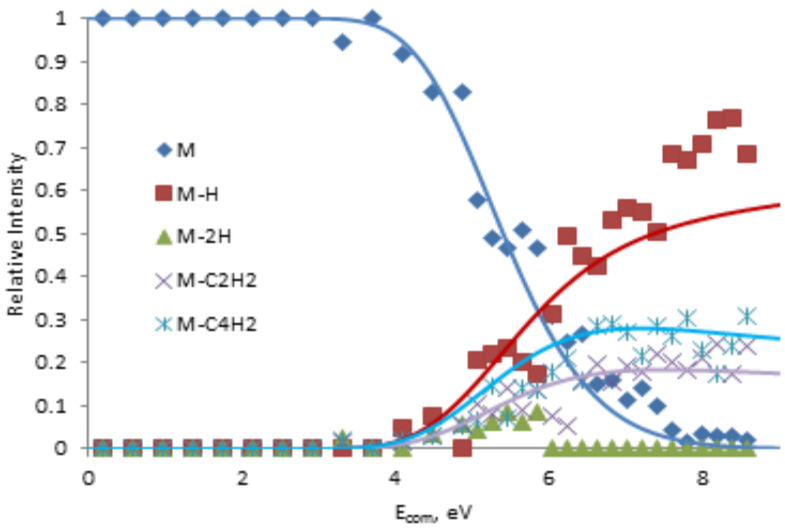

Figure 4-9: Experimental breakdown curves (points) and the results of RRKM modeling (lines) for $C_{13}H_9^{+\bullet}$.

Above 7 eV, $M\text{-}H^+$ starts to lose (to contribute to the $M\text{-}2H^+$ channel) and thus the fitting is poor above the E_{com}.

Table 4.4. Summary of the activation energies (E_0) and entropies ($\Delta^{\ddagger}S$) for the dissociation of the fluorene-H cation.

Channels	E_0 (eV)	$\Delta^{\ddagger}S$ $J\ K^{-1}mol^{-1}$
M-H	3.94 ± 0.1	20.85 ± 4.45
M-C_2H_2	3.84 ± 0.1	10.07 ± -4.25
M-C_4H_2	3.74 ± 0.04	15.94 ± 4.07

T_i and α were at 400 K and 335 KeV^{-1} respectively

4.5 Anthracene and Phenanthrene

Ling and Lifshitz have studied the fragmentations of the anthracene cation and its isomer phenanthrene, $C_{14}H_{10}^{\bullet+}$.[11] They included in their study a summary of "expected" experimental fragmentation products supported by theoretical calculations for the molecular structure of the fragment ions. The primary fragmentation channels for these molecules are similar to those of naphthalene, including $H^{\bullet}$, H_2, C_2H_2, $C_3H_3^{\bullet}$, and C_4H_2 losses.[11] In 2014, West et al. explored the anthracene radical cation fragmentation chemistry by using iPEPICO. The main fragmentation channels observed were H, 2H, and C_2H_2 respectively.[12] In this work, we investigated the anthracene and phenanthrene radical cations via APCI-CID experiments. CID experiments show three primary fragmentation channels for these two ions, fig 4.11.

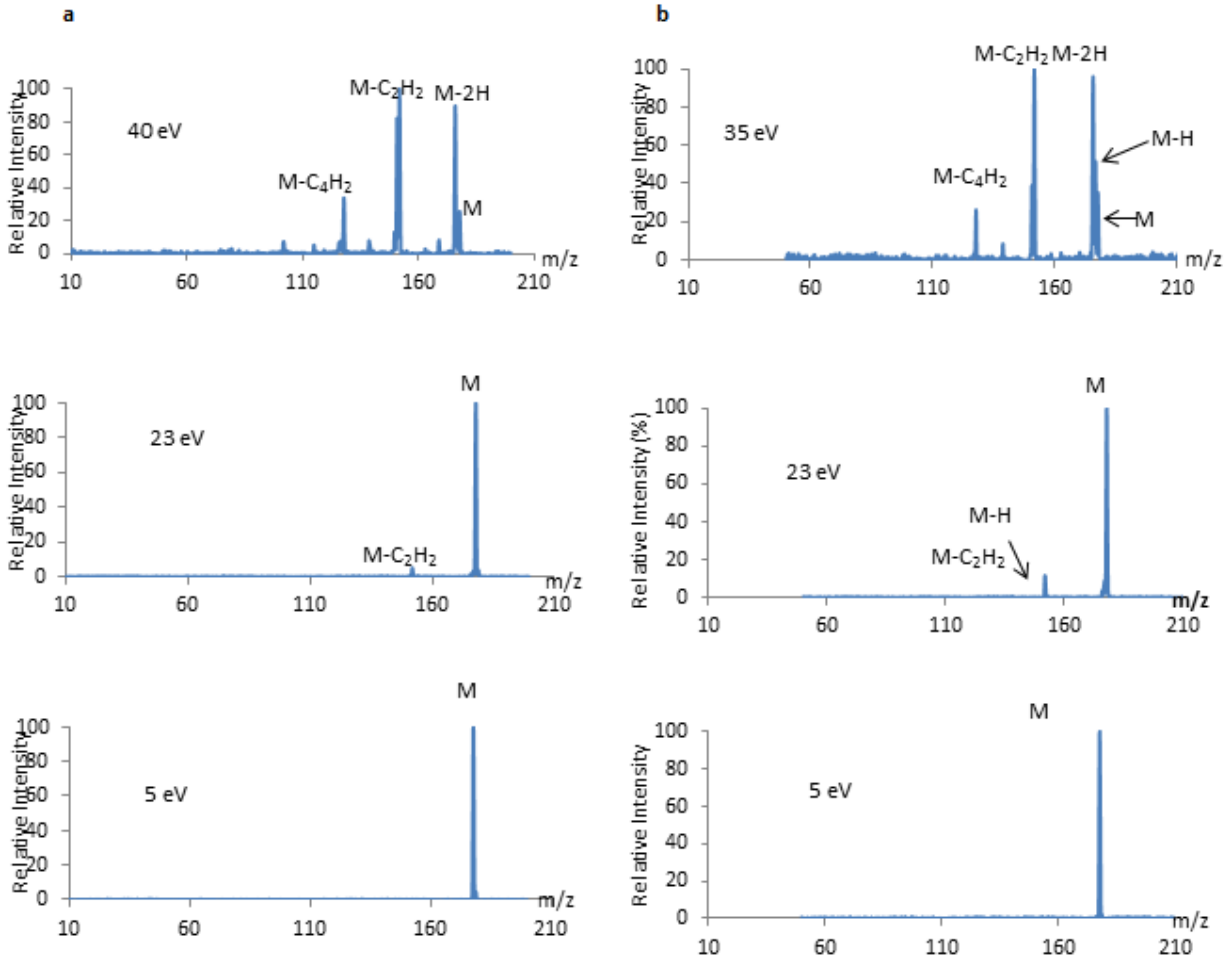

Figure 4-11: CID mass spectra at different collision energies of a) ionized anthracene and b) ionized phenanthrene.

Three primary dissociation channels of anthracene and phenanthrene correspond to the reactions (R1) through (R3) below;

$$C_{14}H_{10}^{+\bullet} \longrightarrow C_{14}H_9^{+} + H^{\bullet} \qquad \text{(R1)}$$

$$C_{14}H_{10}^{+\bullet} \longrightarrow C_{12}H_8^{+\bullet} + C_2H_2 \qquad \text{(R2)}$$

$$C_{14}H_{10}^{+\bullet} \longrightarrow C_{10}H_8^{+\bullet} + C_4H_2 \qquad \text{(R3)}$$

Reactions R1 and R2 were observed by iPEPICO and CID experiments while reaction R3 was only observed only in the current CID work. Fig A.7 in Appendix shows the calculated lowest energy product ion structures, but there was no attempt made to fully elucidate the reaction mechanisms. To facilitate modeling of the primary reactions, requential products were summed into their primary precursors. Thus, the intensity of the $[M-2H]^{+\cdot}$ was added to that for $[M-H]^+$ since it clearly arose from the dissociation of the latter, and not directly from the M+ ion itself. Fig 4.12 displays the final experimental breakdown curves for the two ions and the results of RRKM modeling. Calculated and derived harmonic frequencies used in the modeling are found in Table A.6 and A.7 in Appendix . The results of the RRKM analysis are shown in Table 4.5. The initial temperature value determined for the anthracene and phenanthrene radical cation were 400 K and 700 K respectively, while the α values were 400 KeV^{-1} and 345 KeV^{-1}, respectively.

Table 4.2 : RRKM results for the activation energy (E_0) and entropy ($\Delta^{\ddagger}S$) for all dissociation channels for ionized anthracene and phenanthrene.

Channels	E_0 (eV)	$\Delta^{\ddagger}S_{1000K}$ (J mol^{-1} K^{-1})
Anthracene		
M-H	4.55 ± 0.1	13 ± 2
M-C_2H_2	4.18 ± 0.1	-1 ± 2
M- C_4H_2	4.87 ± 0.3	23 ± 8
Phenanthrene		
M-H	4.20 ± 0.1	4 ± 4
M-C_2H_2	3.84 ± 0.05	-10 ± 3
M-C_4H_2	4.50 ± 0.05	10 ± 4

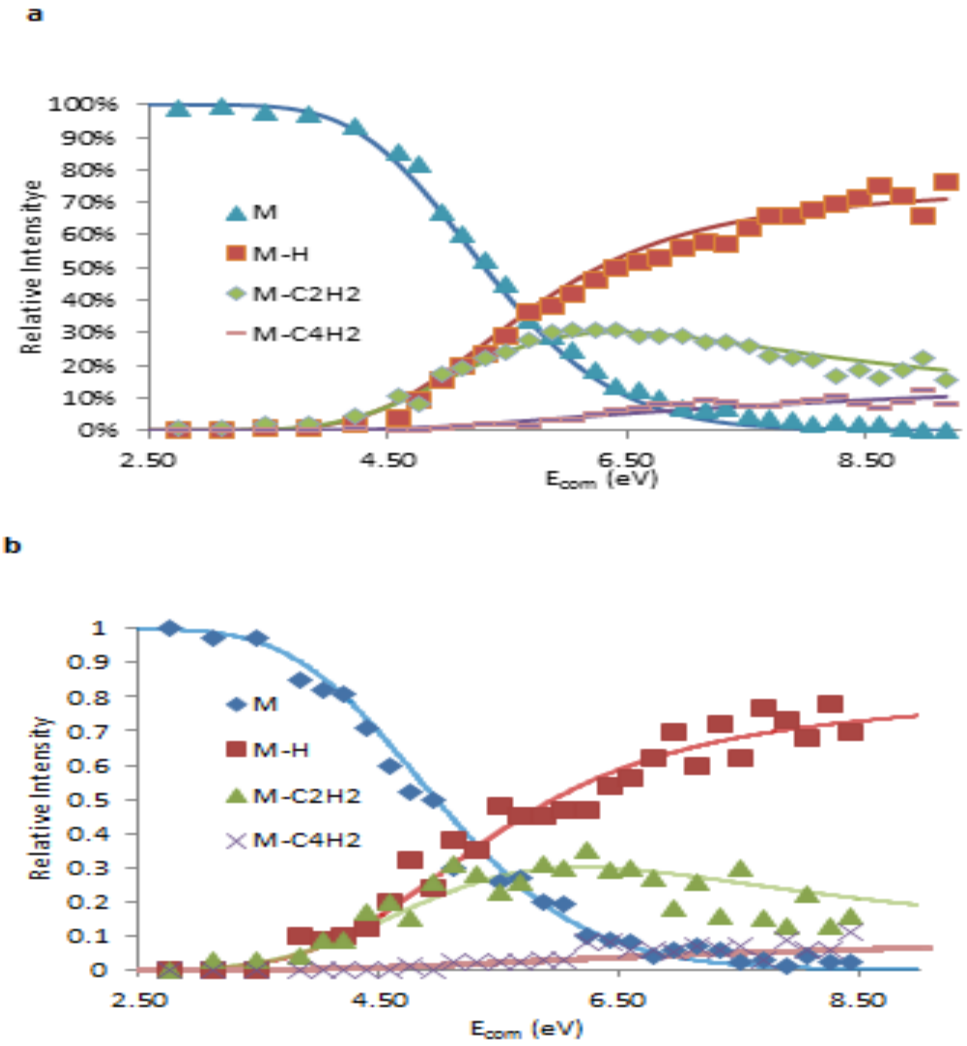

Figure 4-10: CID breakdown curves (points) and RRKM modeling results (lines) for ionized a) anthracene and b) phenanthrene.

4.6 Cyclopenta [d,e,f] phenanthrene

The primary dissociation channel observed for ionized cyclopenta [d,e,f] phenanthrene is H loss which leads to a fully unsaturated ion that itself then undergoes the typical H and C_2H_2 loss reactions. Fig 4.13 shows CID mass spectra for ionized cyclopenta[d,e,f]phenanthrene with the

primary and sequential fragmentation products at different collision energies. As was done for fluorene-H ion, the parent ion region had to be deconvoluted in Igor Pro 6.37 program.

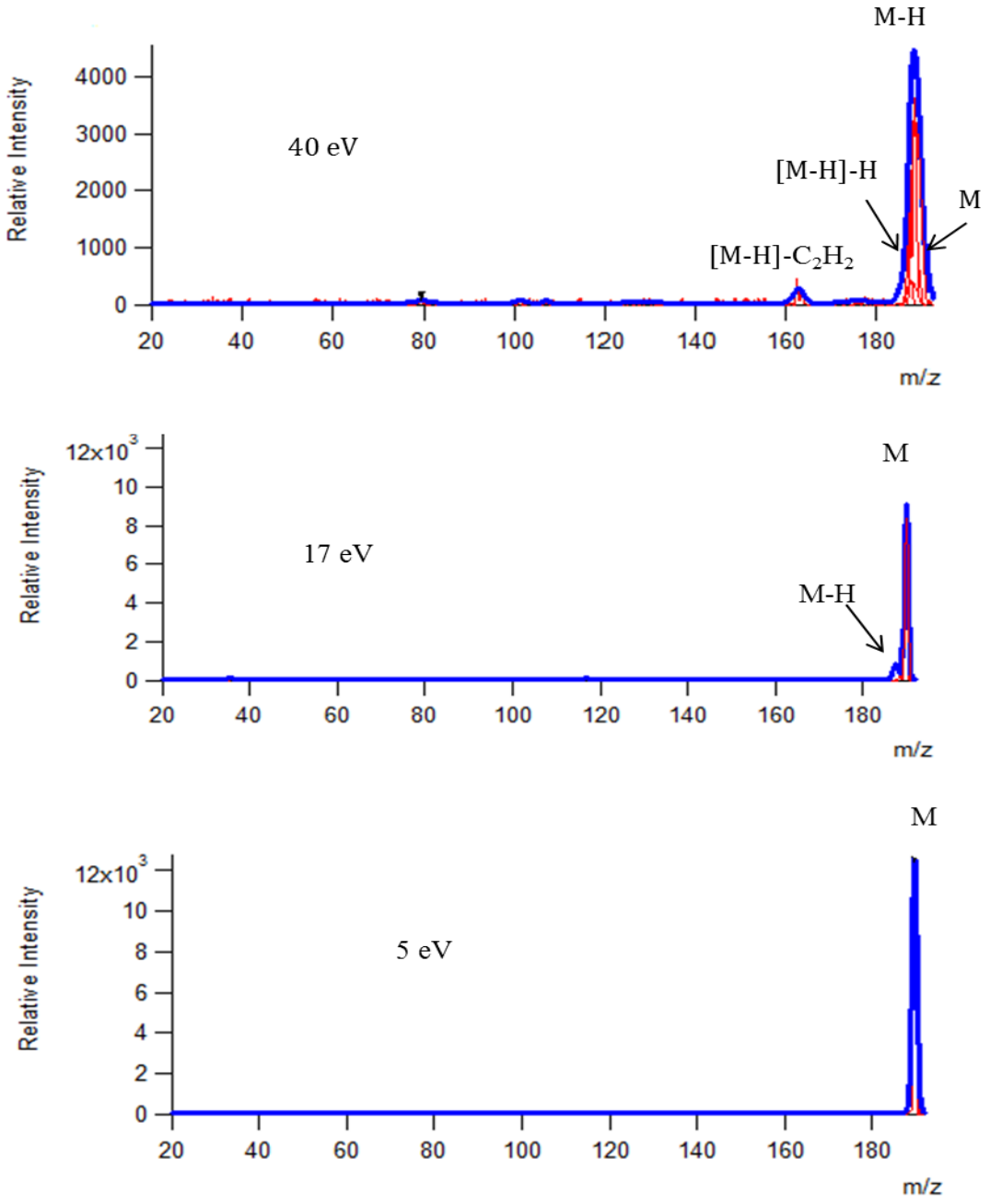

Figure 4-11:CID mass spectra of $C_{15}H_{10}^{\bullet+}$ ions at different collision energies, together with the Gaussian deconvolution of the peaks in the parent ion region.

Only the primary loss of H was modeled with RRKM theory ,fig 4.14 and the reaction was found to have an E_0 of 3.0 ± 0.09 eV, similar to the other ions featuring an sp^3-carbon. The $\Delta^{\ddagger}S$ was found to be 3.55 ± 4.40 (T_i and α were at 450K and 360 KeV^{-1} respectively).

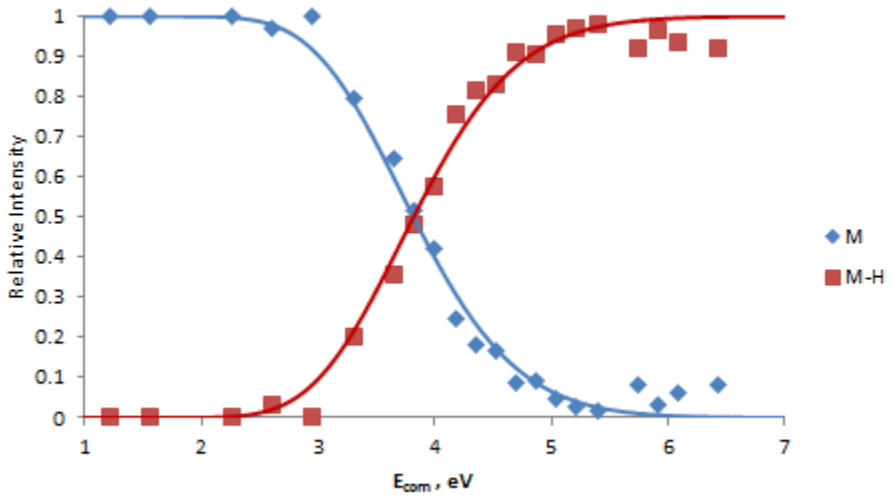

Figure 4-12: Experimental breakdown curves (points) and the results of RRKM modeling (lines) for $C_{15}H_{10}^{+\bullet}$.

4.7 Pyrene

Dissociation of the pyrene radical cation has been studied via time-resolved photo-ionization in the VUV, MS/MS with electron ionization and RRKM/QET calculations. The primary channels were observed are similar $H^{\bullet}$ and H_2 losses, as well following $H^{\bullet}$ losses, similar to those reported by Ling et al.[13] Our experiments also feature a minor loss of C_2H_2, fig 4.15.

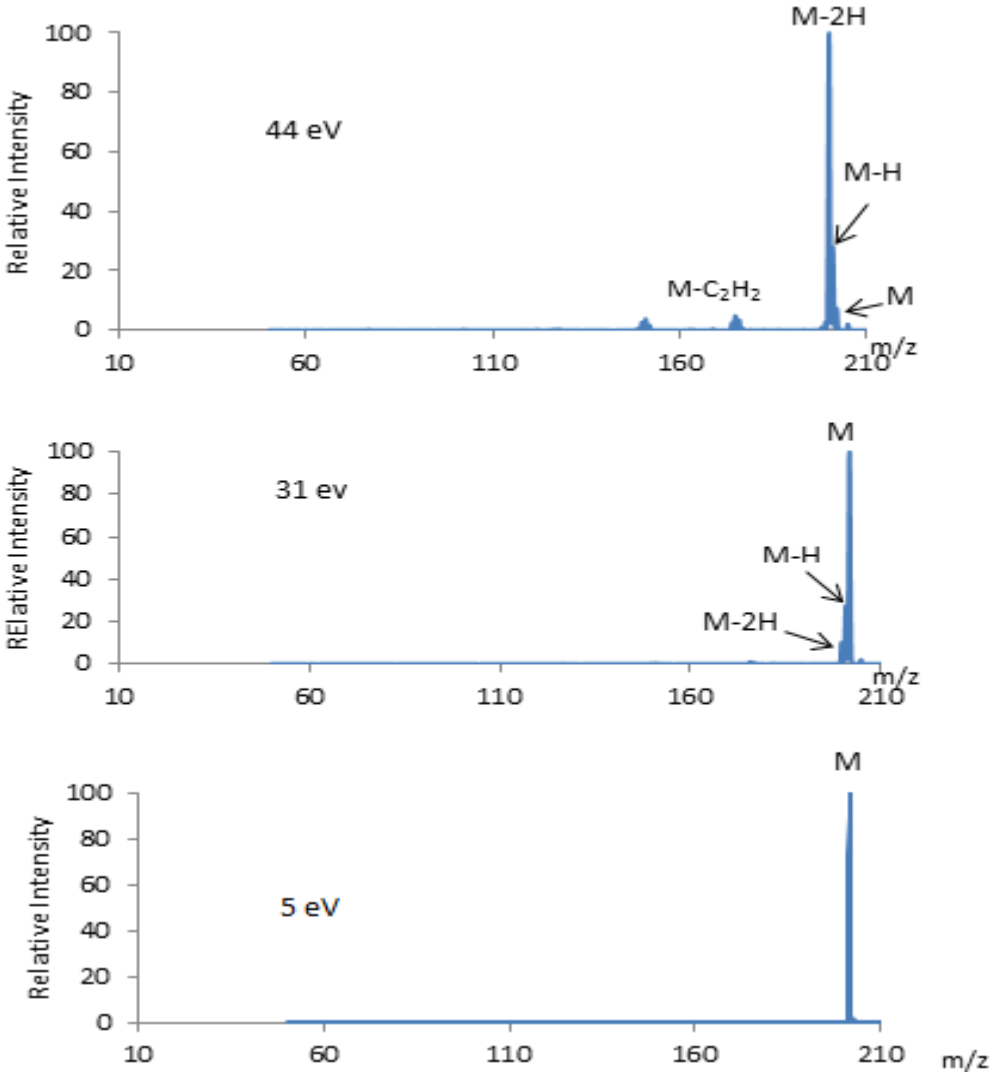

Figure 4-13:CID mass spectra of $C_{16}H_{10}^{\bullet+}$ ions at different collision energies.

The experimental breakdown curve was modeled using RRKM theory to produce the theoretical breakdown curve of the pyrene radical cation. The final result of the best fit between experimental and theoretical breakdown diagrams is shown in fig4.16. The RRKM results are summarized in Table 4.6.

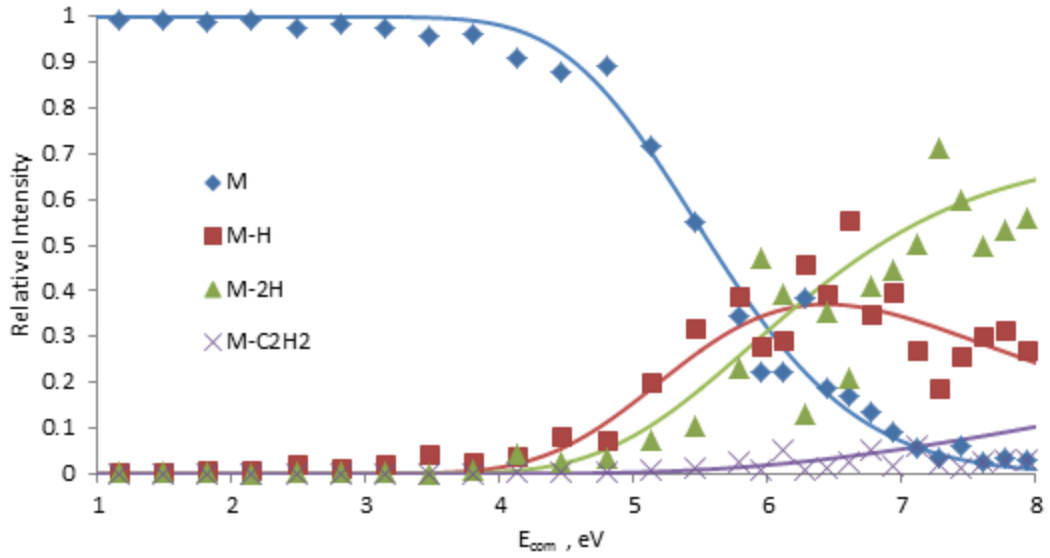

Figure 4-14: Experimental breakdown curves (points) and the results of RRKM modeling (lines) for $C_{16}H_{10}^{+\bullet}$.

Table 4.6: Summary of the activation energies (E_0) and entropies ($\Delta^{\ddagger}S$) for the dissociation of the pyrene cation.

Channels	E_0 (eV)	$\Delta^{\ddagger}S$ (J K^{-1} mol^{-1})
M-H	4.05 ± 0.2	-31 ± 8
M-2H	5.0 ± 0.2	7 ± 8
M-C_2H_2	6.1 ± 0.3	24 ± 14

T_i and α set to 500 K and 410 KeV^{-1} respectively

4.8 Fluoranthene

Ling et al. have studied the fragmentations of the fluoranthene radical cation, an isomer of pyrene, via time-resolved photoionization in the vacuum UV, MS/MS with electron ionization, and RRKM/QET calculations. The primary channels observed are loss of $H^{\cdot}$ and H_2 loss, as well as successive $H^{\cdot}$ losses.[14] We also observe C_4H_2 loss in our CID experiments, fig 4.17. The parent region in each spectrum was deconvoluted with the Igor Pro 6.37 program as described earlier.

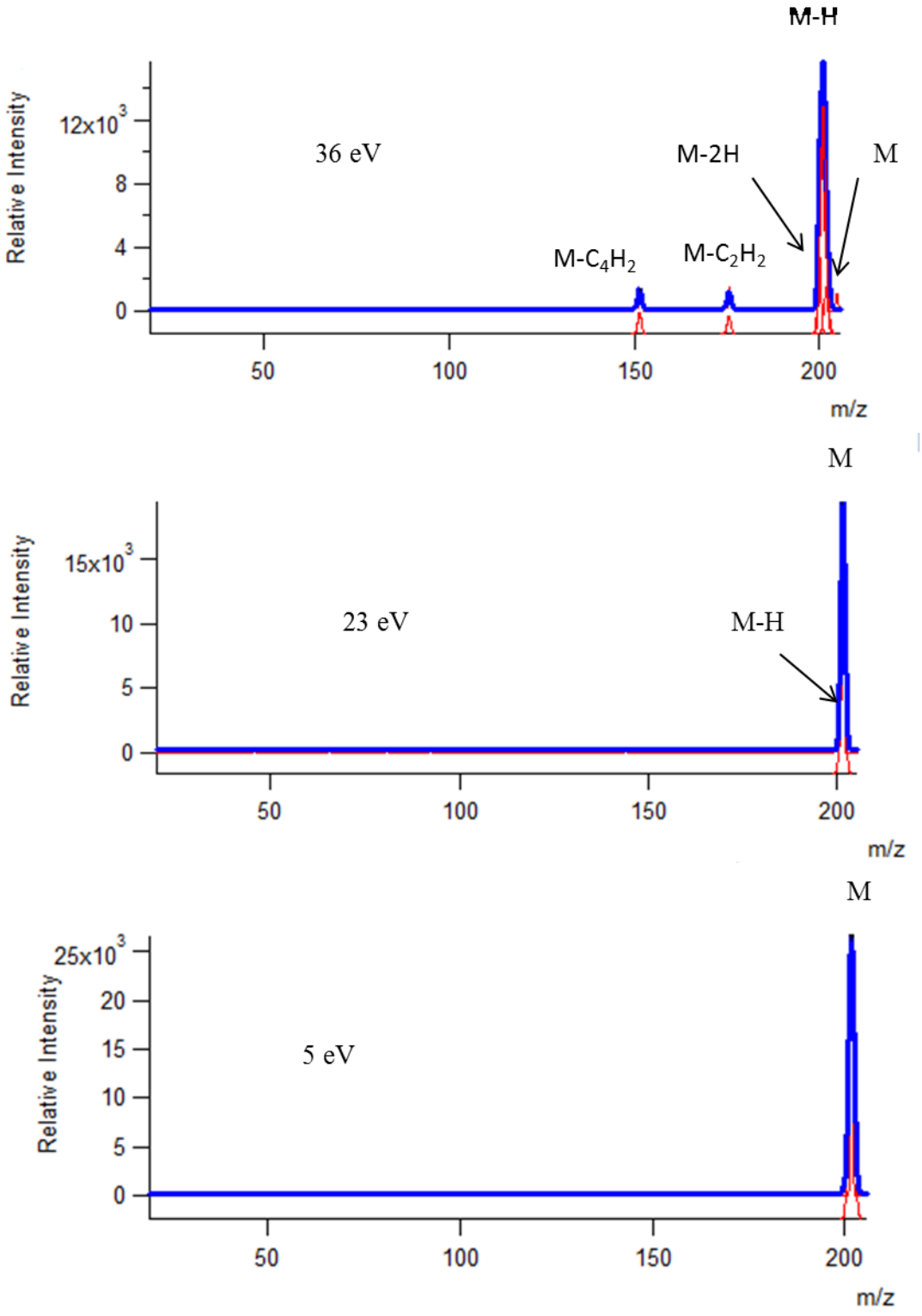

Figure 4-15: CID mass spectra of fluoranthene $C_{16}H_{10}^{\bullet+}$ ions at different collision energies, together with the Gaussian deconvolution of the peaks in the parent ion region.

The experimental breakdown curve was modeled using RRKM theory and the results are shown in fig 4.18, with the RRKM parameters summarized in Table 4.7. In this fitting, the M-2H channel was added to the M-H channel at 6 eV and above. The two minor hydrocarbon loss channels were combined to yield a single energy requirement for hydrocarbon loss.

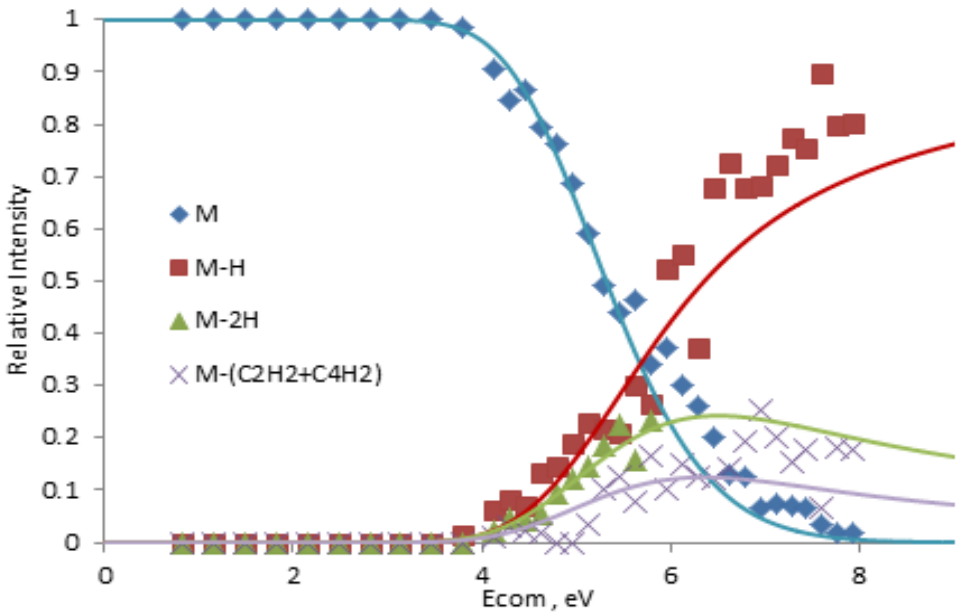

Figure 4-16: Experimental breakdown curves (points) and the results of RRKM modeling (lines) for $C_{16}H_{10}^{+\bullet}$.

The first reaction fluoranthrene was H loss and the activation energy for this channel was found to be 4.1 eV, in good agreement with the E_0 of H loss from pyrene (4.1 eV).

Table 4.7. Summary of the activation energies (E_0) and entropies ($\Delta^{\ddagger}S$) for the dissociation of the fluoranthrene cation.

Channels	E_0 (eV)	$\Delta^{\ddagger} S$ ($J\ K^{-1}\ mol^{-1}$)
M-H	4.1 ± 0.2	38 ± 8
M-2H	3.66 ± 0.2	8 ± 8
M-(C_2H_2 + C_4H_2)	3.64 ± 0.3	3.6 ± 14

Ti was 400 K and α was 330 KeV^{-1} .

4.9 Perylene

The unimolecular dissociation of the perylene radical cation takes place by H loss and H_2 loss as well as a minor C_2H_2 loss apparent in a few of the CID mass spectra, fig 4.19. Since it is so minor, we do not include the C_2H_2 loss ion in the is not included in an experimental breakdown curve, fig 4.20. RRKM results are summarized in Table 4.8.

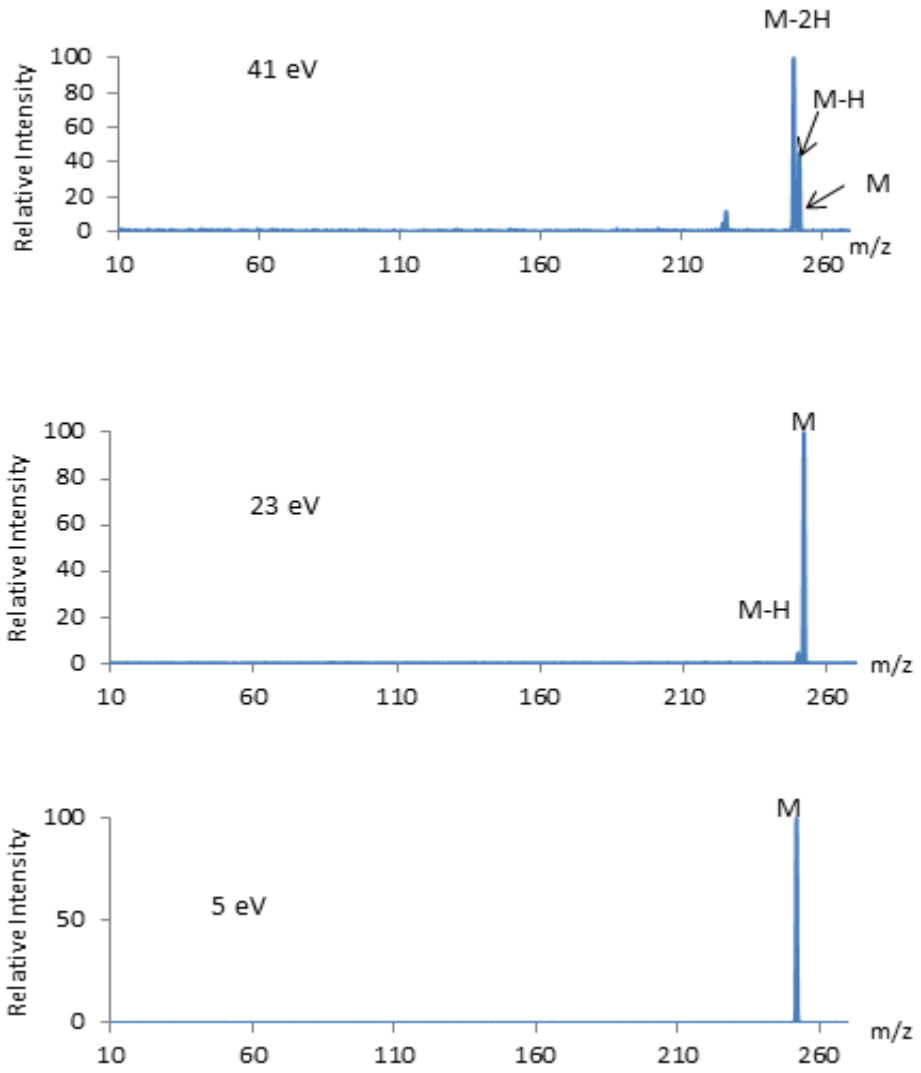

Figure 4-17:CID mass spectra of perylene $C_{20}H_{12}^{\bullet+}$ ions at different collision energies.

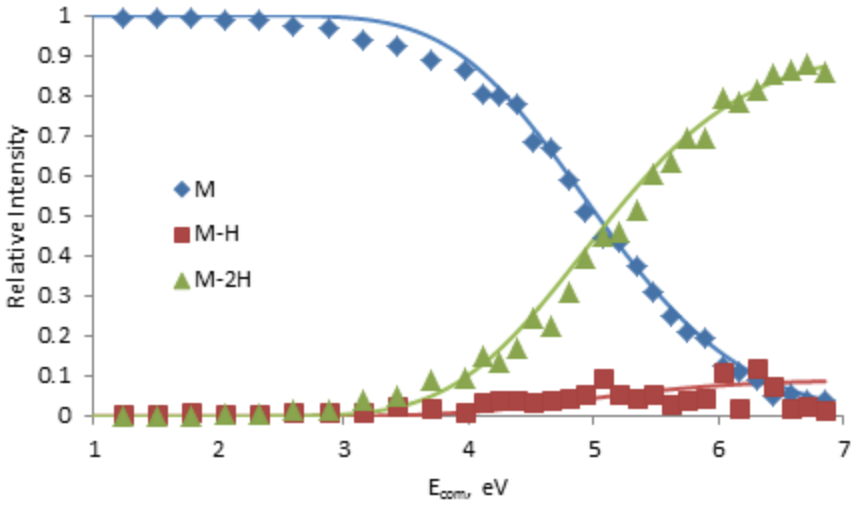

Figure 4-18: Experimental breakdown curves (points) and the results of RRKM modeling (lines) for $C_{20}H_{12}^{+\bullet}$ ions.

Table 4.8. Summary of the activation energies (E_0) and entropies ($\Delta^{\ddagger}S$) for the dissociation of the perylene cation.

Channel	E_0 (eV)	$\Delta^{\ddagger}S$ ($JK^{-1}mol^{-1}$)
M-H	4.1 ± 0.1	-22 ± 4
M–2H	4.1 ± 0.1	0 ± 7

T_i and α set to 800 K and 300 KeV^{-1} respectively

4.10 Coronene

The coronene molecule was the largest PAH studied in this thesis. As with the other larger PAHs, the main dissociation pathways simplify to loss of H and H2/2H, fig 4.21. Loss of a third H

atom was periodically observed in mass spectra, but was not consistently enough to be considered anything other than an artifact.

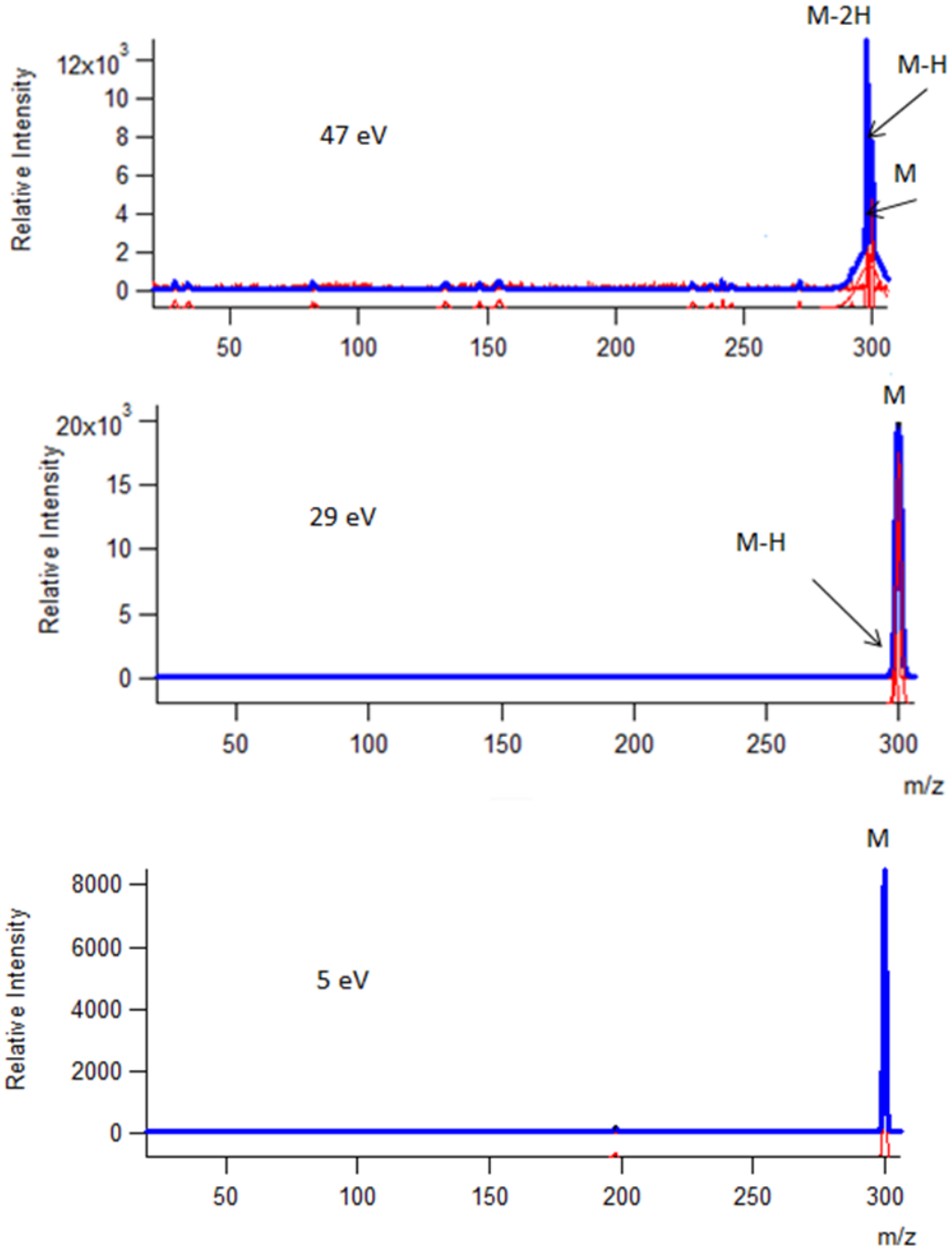

Figure 4-19:CID mass spectra of $C_{24}H_{12}^{\bullet+}$ ions at different collision energies, together with the Gaussian deconvolution of the peaks in the parent ion region.

The most likely structures for the main fragmentation products are displayed in Appendix .

The experimental breakdown curves and subsequent RRKM model are shown in Figure 4.22, and the RRKM results are summarized in Table 4.9.

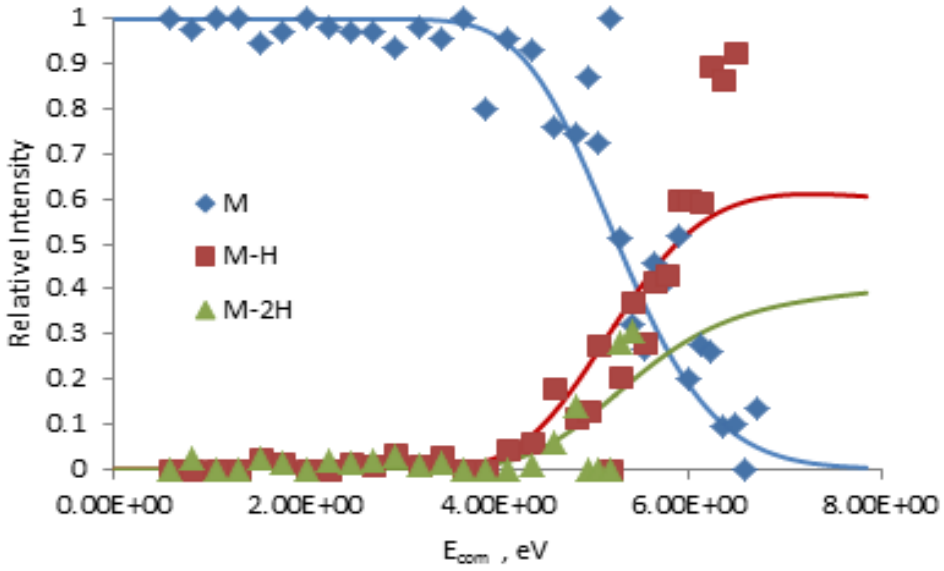

Figure 4-20: Experimental breakdown curves (points) and the results of RRKM modeling (lines) for $C_{24}H_{12}^{+\bullet}$ ions.

Table 4.9. Summary of the activation energies (E_0) and entropies ($\Delta^{\ddagger}S$) for the dissociation of the coronene cation.

Channels	E_0 (eV)	$\Delta^{\ddagger}S$ J $K^{-1}mol^{-1}$
M-H	3.72 ± 0.1	-1 ± 4.6
M-2H	3.85 ± 0.1	0 ± 6.7

T_i and α set at 378 K and 330 KeV^{-1} respectively.

4.11 References.

1. West, B.; Joblin, C.; Blanchet, V.; Bodi, A.; Sztáray, B.; Mayer, P. M., On the dissociation of the naphthalene radical cation: new iPEPICO and tandem mass spectrometry results. *The Journal of Physical Chemistry A* **2012,** *116* (45), 10999-11007.
2. Solano, E. A.; Mayer, P. M., A complete map of the ion chemistry of the naphthalene radical cation? DFT and RRKM modeling of a complex potential energy surface. *The Journal of chemical physics* **2015,** *143* (10), 104305.
3. Gallup, G. A.; Steinheider, D.; Gross, M. L., A mechanism for hydrogen scrambling in ionized benzene. *International Journal of Mass Spectrometry and Ion Physics* **1976,** *22* (1), 185-188.
4. Dyakov, Y. A.; Mebel, A.; Lin, S.; Lee, Y.; Ni, C. K., Acetylene elimination in photodissociation of neutral azulene and its cation: an ab initio and RRKM study. *Journal of the Chinese Chemical Society* **2006,** *53* (1), 161-168.
5. Jolibois, F.; Klotz, A.; Gadéa, F.; Joblin, C., Hydrogen dissociation of naphthalene cations: a theoretical study. *Astronomy & Astrophysics* **2005,** *444* (2), 629-634.
6. Carruthers, G. R., Rocket observation of interstellar molecular hydrogen. *The Astrophysical Journal* **1970,** *161*, L81.
7. Gould, R. J.; Salpeter, E. E., The Interstellar Abundance of the Hydrogen Molecule. I. Basic Processes. *The Astrophysical Journal* **1963,** *138*, 393.
8. Lemaire, J.-L.; Vidali, G.; Baouche, S.; Chehrouri, M.; Chaabouni, H.; Mokrane, H., Competing mechanisms of molecular hydrogen formation in conditions relevant to the interstellar medium. *The Astrophysical Journal Letters* **2010,** *725* (2), L156.
9. Cazaux, S.; Morisset, S.; Spaans, M.; Allouche, A., When sticking influences H2 formation. *Astronomy & Astrophysics* **2011,** *535*, A27.
10. West, B.; Joblin, C.; Blanchet, V.; Bodi, A.; Sztáray, B.; Mayer, P. M., Dynamics of hydrogen and methyl radical loss from ionized dihydro-polycyclic aromatic hydrocarbons: A tandem mass spectrometry and imaging photoelectron–photoion coincidence (iPEPICO) study of dihydronaphthalene and dihydrophenanthrene. *The Journal of Physical Chemistry A* **2014,** *118* (10), 1807-1816.
11. Ling, Y.; Lifshitz, C., Time-Dependent mass spectra and breakdown graphs. 21. C14H10 isomers. *The Journal of Physical Chemistry A* **1998,** *102* (4), 708-716.
12. West, B.; Sit, A.; Mohamed, S.; Joblin, C.; Blanchet, V.; Bodi, A.; Mayer, P. M., Dissociation of the Anthracene Radical Cation: A Comparative Look at iPEPICO and Collision-Induced Dissociation Mass Spectrometry Results. *The Journal of Physical Chemistry A* **2014,** *118* (42), 9870-9878.
13. Ling, Y.; Gotkis, Y.; Lifshitz, C., Time-dependent mass spectra and breakdown graphs. 18. pyrene. *European Journal of Mass Spectrometry* **1995,** *1* (1), 41-49.
14. Ling, Y.; Lifshitz, C., Time-Dependent Mass Spectra and Breakdown Graphs. 19. Fluoranthene. *The Journal of Physical Chemistry* **1995,** *99* (28), 11074-11080.

Chapter 5. Discussion

In this chapter the results of the present APCI-CID experiments will be compared with iPEPICO and other literature data. The data is summarized in table 5.1. In general, there is good qualitative agreement between the activation entropies and energies derived from the RRKM modeling of the CID breakdown curves with those obtained from the RRKM modeling of iPEPICO data and time-resolved photodissociation data of Ling and co-workers.

All of the PAH ions studied in this project yielded either one or two primary fragmentation channels: hydrogen atom loss and hydrocarbon loss. Hydrogen atom loss was the common channel in all PAH ions. It was previously stipulated that the activation energies values for H loss were found to increase with the size of PAH.[1] If we compared the activation energy of H loss for naphthalene with another molecule such as benzene or anthracene, it presented that the E_0 of C-H bond for naphthalene (4.10 eV) is greater than the energy of activation for benzene (3.7 eV), but smaller than that found in anthracene (4.55 eV).[1] As the size of the PAH increases, this reaction's energetics drop to ~ 4 eV, and finally to 3.7 eV with coronene. This could speak to a change in mechanism with increasing size of PAH. It was noted that H loss from naphthalene ions is preceded by extensive scrambelling of the carbon backbone [2] , while this may not be the case as the PAH skeleton gets larger.

Table 5.1 : Activation energy (E_0) and entropy ($\Delta^{\ddagger}S$) for the CID of the PAH ions compared to iPEPICO values.

		Activation energies E_0 (eV)			Entropies of activation $\Delta^{\ddagger}S_{1000}$ ($JK^{-1}mol^{-1)}$		
	Channels	APCI_CID	iPEPICO	Ling et al	APCI_CID	iPEPICO	Ling et al
NAP	M-H	4.1 ± 0.1	4.20 ± 0.04[a]	---	4.0 ± 0.1	2 ± 2 [a]	---
	M-C_2H_2	3.7 ± 0.1	4.12 ± 0.05[a]	---	-15 ± 4	0 ± 2 [a]	---
	M-C_4H_2	4.1 ± 0.1	4.27 ± 0.07[a]	---	4 ± 2	4 ± 4 [a]	---
ANT	M-H	4.6 ± 0.1	4.28 ± 0.29[b]	4.38 ± 0.1[d]	13 ± 2	12 ± 15 [b]	5.9 ± 1 [d]
	M-C_2H_2	4.2 ± 0.1	4.21 ± 0.30[b]	4.50 ± 0.1[d]	-1 ± 2	7 ± 10 [b]	12.8 ± 1[d]
	M-C_4H_2	4.9 ± 0.03	---	4.46 ± 0.1[d]	23 ± 8	---	2.0 ± 1 [d]
PHN	M-H	4.2 ± 0.1	---	3.92 ± 0.1[d]	4 ± 4	---	4.4 ± 1[d]
	M-C_2H_2	3.8 ± 0.1	---	3.99 ± 0.1[d]	-10 ± 3	---	12.3 ± 1[d]
	M-C_4H_2	4.5 ± 0.1	---	4.20 ± 0.1[d]	10 ± 4	---	4.2 ± 1[d]
DHN	M-H	2.5 ± 0.1	2.44 ± 0.10 [c]	---	1 ± 5	27 ± 14 [c]	---
	M-CH_3	2.6 ± 0.1	2.57 ± 0.12 [c]	---	11 ± 8	18 ± 11 [c]	---
DHP	M-H	2.4 ± 0.1	2.37 ± 0.12[c]	---	8 ± 9	18 ± 19 [c]	---
	M-CH_3	2.4 ± 0.1	2.38 ± 0.1 [c]	---	9 ± 6	-3 ±15 [c]	---
FLU-H	M-H	3.9 ± 0.1	4.13[g]	---	20 ± 4	13[g]	---
	M-C_2H_2	3.8 ± 0.1	4.23[g]	---	10 ± -4	-11[g]	---
	M-C_4H_2	3.7 ± 0.1	4.05[g]	---	15 ± 4	-11[g]	---
CYC	M-H	3.0 ± 0.1	3.55[g]	---	4 ± 4	83[g]	---
PYR	M-H	4.1 ± 0.2	---	4.60 [e]	-31 ± 8	---	10.7 [e]
	M-2H	5.0 ± 0.2	---	4.10[e]	7 ± 8	---	13.3 [e]
	M-C_2H_2	6.1 ± 0.3	---	---	24 ± 14	---	---
FLN	M-H	4.1 ± 0.2	4.87[g]	4.38 [f]	44 ± 8	49[g]	12.1 [f]
	M-2H	3.7 ± 0.2	3.29[g]	3.60 [f]	12 ± 3	10[g]	14.4 [f]
	M-(C_2H_2+ C_4H_2)	3.6 ± 0.3	2.59[g]	---	7 ± 3	-44[g]	---
PER	M-H	4.1 ± 0.1	---	---	-22 ± 4	---	---
	M-2H	4.1 ± 0.1	---	---	0 ± 7	---	---
COR	M-H	3.7 ± 0.1	---	---	-1 ± 5	---	---
	M-2H	3.9 ± 0.1	--	---	0 ± 6.7	---	---
ACE	M-H	4.2 ± 0.1	4.99[g]	---	14 ± 6	47[g]	---
	M-2H	4.3 ± 0.1	3.87[g]	---	15 ± 5	33[g]	---
	M-(C_2H_2 + C_4H_2)	4.2 ± 0.1	5.77[g]	---	24 ± 5	73[g]	---

a = reference[76], b = reference[75] and c = reference [85], d = reference[86] , e = reference[87], f = reference[88] , g = unpublished data

Clearly the carbon hybridization has an impact on the C-H bond cleavage reaction energetics as seen by the low values ~ 2.4 eV for dihydro-naphthalene and phenanthrene. These

mechanisms were found by West et al [5] to have two sources for H loss, one directly from the sp^3 site and one from a rearranged structure (that also led to methyl loss). The C-H bond to an sp^2 center is known to be shorter and stronger than that for an sp^3-carbon. [9] The entropies of activation for H loss channel, it showed that all molecules have positive values of $\Delta^{\ddagger} S_{1000K}$ and they have loose transition state; except three of them (PYR, PER and COR) showed negative values of activation entropy and they have a tighter transition states, though the uncertainty in the entropy values precludes concrete conclusions to be drawn from the magnitudes of the values.[1]

The other main channel was hydrocarbons (C_2H_2 and C_4H_2) loss, which was a significant channel for smaller PAHs, but decreased in abundance as the size of the PAH increased to the point that it was not observed for perylene and coronene. This is likely due to an entropy effect whereby hydrocarbon loss, which requires significant rearrangement , can not compete with loss as the C-S keleton gets larger. Almost all the hydrocarbon loss channels exhibited positive entropy of activation values indicating that the processes are generally governed by entropically favorable, loose, transition states.[1,8]

To better summarize the agreement between the APCI-CID result with iPEPICO results, the respective activation energies were plotted against each other in fig 5.1.

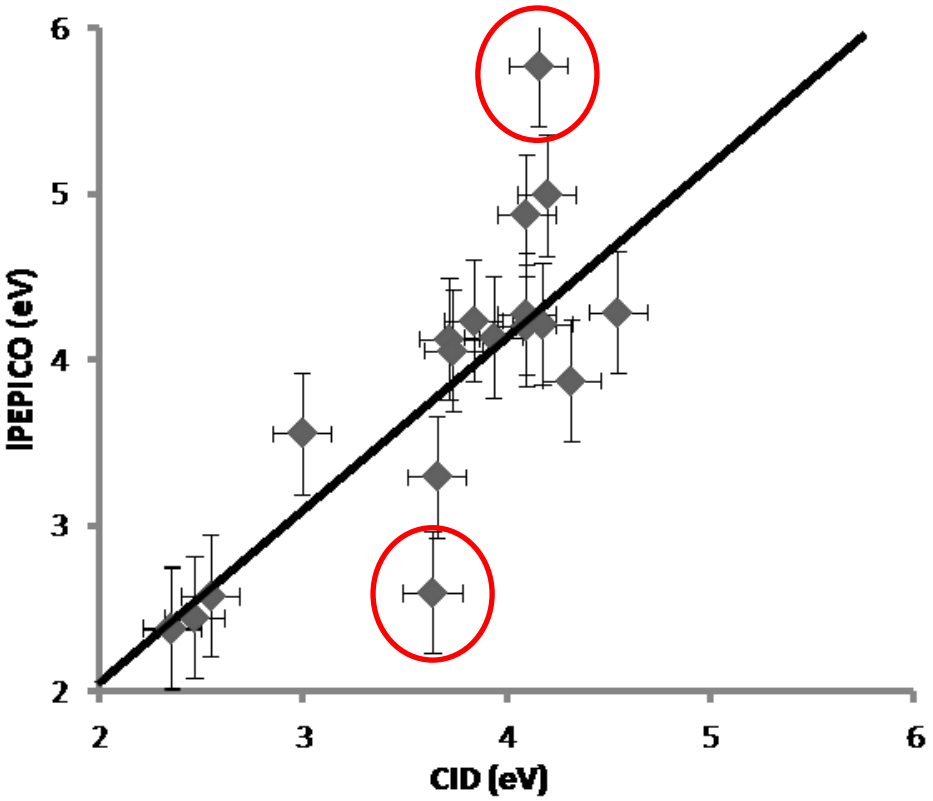

Figure 5-1: Plot of the RRKM derived activation energies for all channels from iPEPICO and APCI-CID measurements. The solid line represents the 1:1 relationship.

.

In general the data falls along the 1:1 line represented by the solid line in Figure 5.1. The main outlier, indicated in red, correspond to the loss of hydrocarbon from fluoranthene and acenaphthylene. Since these iPEPICO values (based on unpublished data from our group) appear to not only disagree with the APCI-CID results, but also other iPEPICO values, it is likely

that the RRKM modeling of the iPEPICO data for these two molecules need to be refined. The average error for the activation energy of the CID method is 0.1eV while it is 0.14 eV for the iPEPICO method. Also, I believe that the APCI source will be a good method to study large molecules of PAHs . The activation energies for large molecule will be observed at 5 eV or less (especially for first fragmentation because all hydrogen atoms attached with sp^2-carbons on the molecule structure such as ovalene).

5.2 References

1. Ho, Y.-P.; Dunbar, R. C.; Lifshitz, C., CH bond strength of naphthalene ion. a reevaluation using new time-resolved photodissociation results. *Journal of the American Chemical Society* **1995,** *117* (24), 6504-6508.
2. Solano, E. A.; Mayer, P. M., A complete map of the ion chemistry of the naphthalene radical cation? DFT and RRKM modeling of a complex potential energy surface. *The Journal of chemical physics* **2015,** *143* (10), 104305.
3. West, B.; Joblin, C.; Blanchet, V.; Bodi, A.; Sztáray, B.; Mayer, P. M., On the dissociation of the naphthalene radical cation: new iPEPICO and tandem mass spectrometry results. *The Journal of Physical Chemistry A* **2012,** *116* (45), 10999-11007.
4. West, B.; Sit, A.; Mohamed, S.; Joblin, C.; Blanchet, V.; Bodi, A.; Mayer, P. M., Dissociation of the Anthracene Radical Cation: A Comparative Look at iPEPICO and Collision-Induced Dissociation Mass Spectrometry Results. *The Journal of Physical Chemistry A* **2014,** *118* (42), 9870-9878.
5. West, B.; Joblin, C.; Blanchet, V.; Bodi, A.; Sztáray, B.; Mayer, P. M., Dynamics of hydrogen and methyl radical loss from ionized dihydro-polycyclic aromatic hydrocarbons: A tandem mass spectrometry and imaging photoelectron–photoion coincidence (iPEPICO) study of dihydronaphthalene and dihydrophenanthrene. *The Journal of Physical Chemistry A* **2014,** *118* (10), 1807-1816.
6. Ling, Y.; Lifshitz, C., Time-Dependent mass spectra and breakdown graphs. 21. C14H10 isomers. *The Journal of Physical Chemistry A* **1998,** *102* (4), 708-716.
7. Ling, Y.; Gotkis, Y.; Lifshitz, C., Time-dependent mass spectra and breakdown graphs. 18. pyrene. *European Journal of Mass Spectrometry* **1995,** *1* (1), 41-49.
8. Ling, Y.; Lifshitz, C., Time-Dependent Mass Spectra and Breakdown Graphs. 19. Fluoranthene. *The Journal of Physical Chemistry* **1995,** *99* (28), 11074-11080.
9. Anslyn, E. V.; Dougherty, D. A., *Modern physical organic chemistry*. University Science Books: 2006.

Chapter 6. Conclusions

The dissociation of PAH radical cations has been studied using atmospheric pressure chemical ionization – collision induced dissociation mass spectrometry. The common primary fragmentation channels observed from these molecules included H loss, C_2H_2 loss, C_4H_2 loss and 2H loss as well. The activation entropies and energies of activation derived for each channel by the RRKM modeling of CID breakdown curves were found to be in general agreement with the results from iPEPICO studies on the same molecules.

All PAHs molecules produce the primary dissociation channel was H loss and this channel was a joint channel for all PAHs. The activation energy for H loss from naphthalene was 4.10 eV and it is high energy compared to the E_0 for H loss from coronene was 3.70 eV which lets us to consider that the structure of PAHs molecules contain of 5 rings or more will yield low dissociation energy for H loss. However, the activation energy for H loss from dihydro- PAHs was low ~ 2.4 eV because of the hydrogen atom was removed easier than other PAHs molecules.

The C_2H_2 channel was another main channel was observed by PAHs molecules and the dissociation energy for C_2H_2 loss was lower by 0.4 eV than the E_0 for H loss, except Pyrene molecule which showed high dissociation energy for C_2H_2 loss ~ 6.1 eV. The dissociation energy for both channels that yield from PAHs molecules were about 3.7 – 6.1 eV. Based on these results, the dissociation energies for PAHs ions in the ISM could be similar to these results that

illustrated in this study. Also, PAHs could be a loss hydrogen atom easily, especially from dihydro-PAHs molecules with low dissociation energy. In this case, PAHs molecules might be one of primary source to yield hydrogen atom in the space due to the highest abundance of elements were observed there was hydrogen.

The APCI-CID technique has proven to be a useful complimentary tool to iPEPICO spectroscopy (and a lab-frame technique as opposed to a major national facility) for the study of the ion chemistry of ionized PAH molecules.

Appendix

A.1 Naphthalene

Table 7.1: Vibrational frequencies (cm^{-1}) of naphthalene radical cation and primary transition state for daughter ion products. The vibrational frequencies in brackets show the frequency that was deleted for each transition state.

$C_{10}H_8$ $^{+\bullet}$ ($M^{+\bullet}$)	TS $(M-H)^+$	TS $(M-C_2H_2)$ $^{+\bullet}$	TS $(M-C_4H_2)$ $^{+\bullet}$
157.75	173.525	205.075	146.7075
182.85	201.135	237.705	170.0505
357.35	393.085	464.555	332.3355
376.07	413.677	488.891	349.7451
426.16	468.776	554.008	396.3288
438.49	482.339	570.037	407.7957
473.54	520.894	615.602	440.3922
514.26	565.686	668.538	478.2618
556.57	612.227	723.541	517.6101
609.01	669.911	791.713	566.3793
730.58	730.58	730.58	730.58
753.71	753.71	753.71	753.71
775.38	775.38	775.38	775.38
777.81	777.81	777.81	777.81
807.88	807.88	807.88	807.88
876.53	876.53	876.53	876.53
937.05	937.05	937.05	937.05
940.78	940.78	940.78	940.78
980.56	980.56	980.56	980.56
1003.55	1003.55	1003.55	1003.55
1023.24	1023.24	1023.24	1023.24
1026.7	1026.7	1026.7	1026.7
1042.07	1042.07	1042.07	1042.07
1071.14	1071.14	1071.14	1071.14
1125.25	1125.25	1125.25	1125.25
1127.87	1127.87	1127.87	1127.87
1199.07	1199.07	1199.07	1199.07
1210.94	1210.94	1210.94	1210.94
1243.64	1243.64	1243.64	1265.22
1265.22	1265.22	1265.22	1310.33

1310.33	1310.33	1310.33	1417.32
1417.32	1417.32	1428.32	1428.32
1428.32	1428.32	1440.38	1440.38
1440.38	1440.38	1476.85	1476.85
1476.85	1476.85	1511.99	1511.99
1511.99	1511.99	1517.66	1517.66
1517.66	1517.66	1559.56	1559.56
1559.56	1559.56	1578.02	1578.02
1578.02	1578.02	1632.11	1632.11
1632.11	1632.11	3208.87	3208.87
3208.87	3208.87	3210.88	3210.88
3210.88	3210.88	3211.32	3211.32
3211.32	3211.32	3213.4	3213.4
3213.4	3213.4	3225.67	3225.67
3225.67	3225.67	3225.8	3225.8
3225.8	3225.8	3235.85	3235.85
3235.85	3235.85	3235.95	3235.95
3235.95	(3235.95)	(1417.32)	(1243.64)

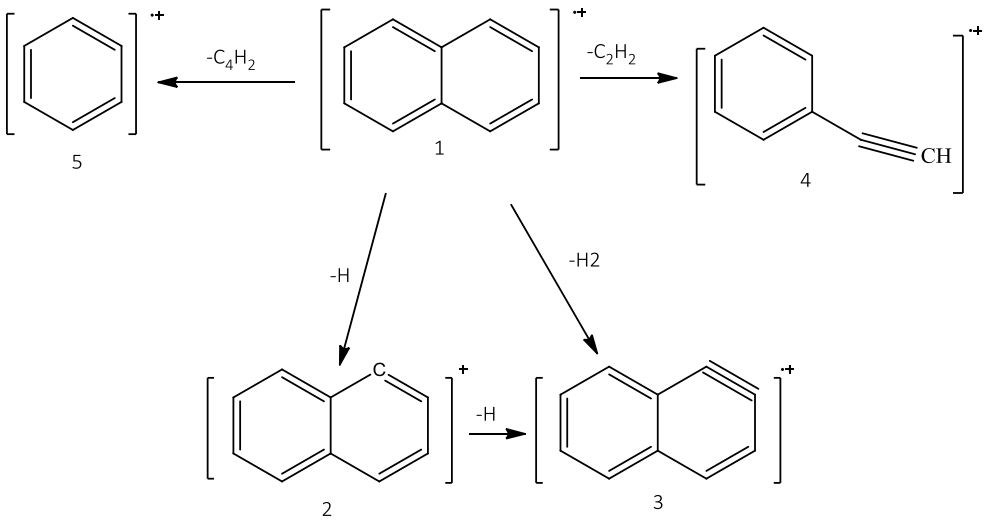

Figure A.1: schematic of all fragment from naphthalene radical cation with the possible structure for each channel.

A.2 Dihydronaphthalene

Table A.2: Vibrational frequencies (cm^{-1}) of 1,2 dihydronaphthalene radical cation and primary transition state for fragment ion products. The vibrational frequencies in brackets show the frequency that was removed for each transition state.

$C_{10}H_{10}^{+\bullet}$ ($M^{+\bullet}$)	TS $(M-H)^{+}$	TS $(M-CH_3)^{+\bullet}$
111.858	121.9252	101.1662
134.8882	147.0281	172.1257
229.5009	250.156	252.7454
336.9938	367.3232	268.9632
358.6176	390.8932	314.0317
418.7089	456.3927	352.3571
469.8095	512.0924	359.6468
479.529	522.6866	375.103
500.1373	545.1497	435.1534
580.2045	632.4229	508.3226
677.7634	677.7634	696.8819
696.8819	696.8819	732.0196
732.0196	732.0196	769.985
769.985	769.985	796.6145
796.6145	796.6145	826.5482
826.5482	826.5482	893.9915
893.9915	893.9915	901.8162
901.8162	901.8162	935.4091
935.4091	935.4091	960.6946
960.6946	960.6946	1002.924
1002.924	1002.924	1013.179
1013.179	1013.179	1024.062
1024.062	1024.062	1032.994
1032.994	1032.994	1041.199
1041.199	1041.199	1148.303
1148.303	1148.303	1162.428
1162.428	1162.428	1190.26
1190.26	1190.26	1201.764
1201.764	1201.764	1212.375
1212.375	1212.375	1243.257

1243.257	1243.257	1263.058
1263.058	1263.058	1286.969
1286.969	1286.969	1341.444
1341.444	1341.444	1377.11
1377.11	1377.11	1395.466
1395.466	1395.466	1420.178
1420.178	1420.178	1452.304
1452.304	1452.304	1455.592
1455.592	1455.592	1481.152
1481.152	1481.152	1499.694
1499.694	1499.694	1535.892
1535.892	1535.892	1564.145
1564.145	1564.145	1629.182
1629.182	1629.182	2947.015
2947.015	2947.015	2989.49
2989.49	2989.49	3067.192
3067.192	3067.192	3093.276
3093.276	3093.276	3173.414
3173.414	3173.414	3184.787
3184.787	3187.473	3187.473
3187.473	3190.859	3190.859
3190.859	3197.23	3197.23
3197.23	3209.875	3209.875
3209.875	(3184.787)	(677.7634)

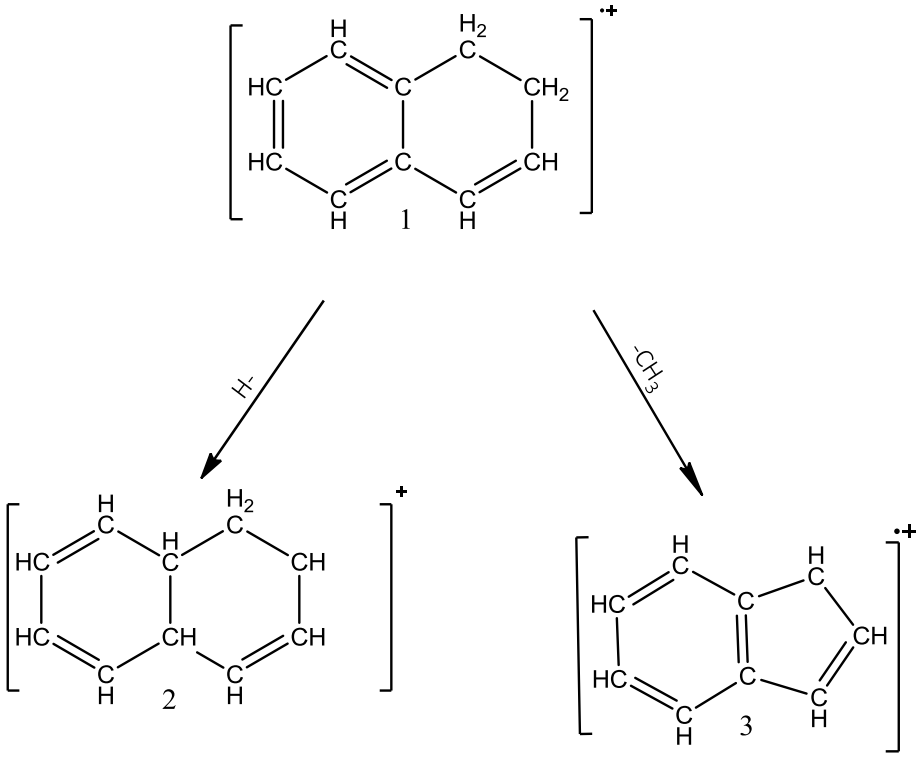

Figure A.2: schematic of two primary fragment from dihydronaphtalene radical cation with a possible structure for each channel

A.3 Dihydrophenanthrene

Table A.3: Vibrational frequencies (cm^{-1}) of 9,10 dihydrophenanthrene radical cation and primary transition state for daughter ion products. The vibrational frequencies in brackets show the frequency that removed for each transition state.

$C_{14}H_{12}^{+\bullet}$ ($M^{+\bullet}$)	TS ($M-H)^{+}$	TS ($M-CH_3)^{+\bullet}$
72.9541	64.92915	62.01099
94.9864	84.5379	80.73844
157.4006	140.0865	133.7905
198.8797	177.0029	169.0477
258.0848	229.6955	219.3721
287.7957	256.1382	244.6263

384.0706	341.8228	326.46
393.1873	349.9367	334.2092
432.4487	384.8793	367.5814
459.2722	408.7523	390.3814
473.8481	473.8481	473.8481
477.9224	477.9224	477.9224
500.3426	500.3426	500.3426
529.5316	529.5316	529.5316
587.9925	587.9925	587.9925
619.9806	619.9806	619.9806
703.9017	703.9017	703.9017
719.1044	719.1044	719.1044
719.5954	719.5954	719.5954
770.8486	770.8486	770.8486
778.8691	778.8691	778.8691
809.0416	809.0416	809.0416
815.7988	815.7988	815.7988
879.9635	879.9635	879.9635
882.6574	882.6574	892.8169
892.8169	892.8169	983.9584
983.9584	983.9584	991.6732
991.6732	991.6732	993.9027
993.9027	993.9027	1003.494
1003.494	1003.494	1018.596
1018.596	1018.596	1020.207
1020.207	1020.207	1034.989
1034.989	1034.989	1048.056
1048.056	1048.056	1052.156
1052.156	1052.156	1114.781
1114.781	1114.781	1156.562
1156.562	1156.562	1182.561
1182.561	1182.561	1187.661
1187.661	1187.661	1194.141
1194.141	1194.141	1199.66
1199.66	1199.66	1228.105
1228.105	1228.105	1235.35
1235.35	1235.35	1284.571
1284.571	1284.571	1298.886
1298.886	1298.886	1318.599
1318.599	1318.599	1353.034
1353.034	1353.034	1359.72

1359.72	1359.72	1378.8
1378.8	1378.8	1398.278
1398.278	1398.278	1454.503
1454.503	1454.503	1459.222
1459.222	1459.222	1471.023
1471.023	1471.023	1472.82
1472.82	1472.82	1495.305
1495.305	1495.305	1507.233
1507.233	1507.233	1537.211
1537.211	1537.211	1548
1548	1548	1615.135
1615.135	1615.135	1635.629
1635.629	1635.629	2995.97
2995.97	2995.97	3009.559
3009.559	3009.559	3095.959
3095.959	3095.959	3096.871
3096.871	3096.871	3184.457
3184.457	3184.457	3184.611
3184.611	3184.611	3194.571
3194.571	3195.354	3195.354
3195.354	3202.317	3202.317
3202.317	3204.918	3204.918
3204.918	3213.851	3213.851
3213.851	3226.091	3226.091
3226.091	(3194.5707)	(882.6574)

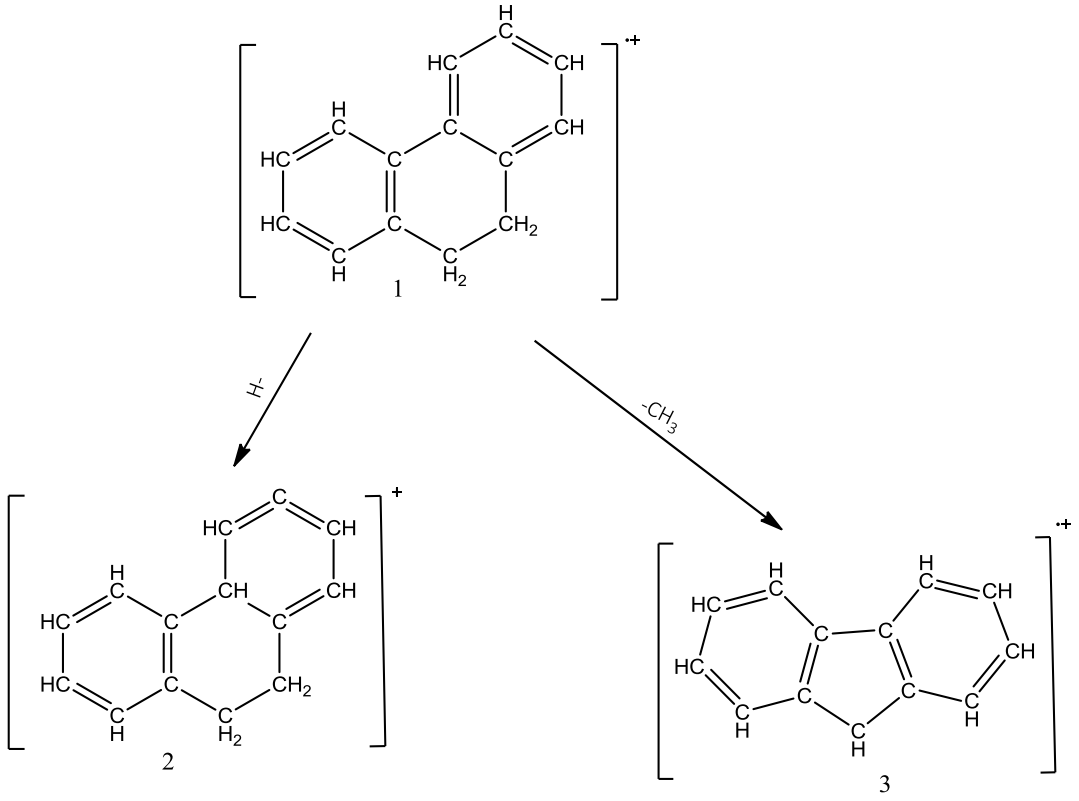

Figure A.3 : schematic of two primary fragments from dihydrophenanthene radical cation with a possible structure for each channel

A.4 Acenaphthylene

Table A.4: Vibrational frequencies (cm^{-1}) of acenaphthylene radical cation and primary transition state for the products of fragment ion. The vibrational frequencies in brackets show the frequency that was removed for each transition state.

$C_{12}H_8^{+\bullet}$ ($M^{+\bullet}$)	TS $(M-H)^+$	TS $(M-2H)^{+\bullet}$	TS $M-(C_2H_2+C_4H_2)^{+\bullet}$
170.434	148.2776	163.6166	124.4168
195.248	169.8658	187.4381	142.531
200.3763	174.3274	192.3612	146.2747
359.2785	312.5723	344.9074	262.2733
419.7885	365.216	402.997	306.4456

437.7345	380.829	420.2251	319.5462
451.4848	392.7918	433.4254	329.5839
490.0273	426.3238	470.4262	357.7199
510.664	444.2777	490.2374	372.7847
541.863	471.4208	520.1885	395.56
548.1053	548.1053	548.1053	548.1053
618.6258	618.6258	618.6258	618.6258
676.85	676.85	676.85	676.85
701.4076	701.4076	701.4076	738.5088
738.5088	738.5088	738.5088	786.2373
786.2373	786.2373	786.2373	790.0486
790.0486	790.0486	790.0486	804.5076
804.5076	804.5076	804.5076	858.8895
858.8895	858.8895	858.8895	859.7024
859.7024	859.7024	859.7024	931.2431
931.2431	931.2431	931.2431	963.3473
963.3473	963.3473	963.3473	975.0849
975.0849	975.0849	975.0849	1015.242
1015.242	1015.242	1015.242	1020.14
1020.14	1020.14	1020.14	1039.743
1039.743	1039.743	1039.743	1043.655
1043.655	1043.655	1043.655	1069.946
1069.946	1069.946	1069.946	1088.615
1088.615	1088.615	1088.615	1112.453
1112.453	1112.453	1112.453	1135.719
1135.719	1135.719	1135.719	1211.021
1211.021	1211.021	1211.021	1226.722
1226.722	1226.722	1226.722	1253.008
1253.008	1253.008	1253.008	1285.087
1285.087	1285.087	1285.087	1337.008
1337.008	1337.008	1337.008	1339.492
1339.492	1339.492	1339.492	1373.799
1373.799	1373.799	1373.799	1390.779
1390.779	1390.779	1390.779	1437.558
1437.558	1437.558	1437.558	1439.8
1439.8	1439.8	1439.8	1478.186
1478.186	1478.186	1478.186	1523.909
1523.909	1523.909	1523.909	1583.575
1583.575	1583.575	1583.575	1611.127
1611.127	1611.127	1611.127	1642.81
1642.81	1642.81	1642.81	3186.36

3186.36	3186.36	3186.36	3186.895
3186.895	3186.895	3186.895	3195.964
3195.964	3195.964	3195.964	3196.109
3196.109	3206.885	3196.109	3206.885
3206.885	3207.123	3206.885	3207.123
3207.123	3219.15	3219.15	3219.15
3219.15	3231.087	3231.087	3231.087
3231.087	(3196.109)	(3207.123)	(701.4076)

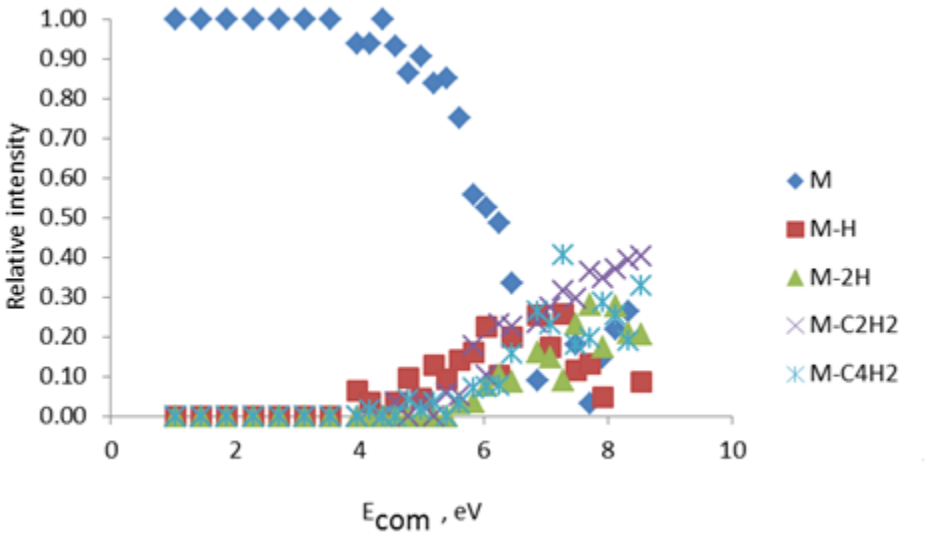

Figure A-4 : experimental breakdown curve of acenaphthylene before adding the M-C_2H_2 channel to M-C_4H_2 channel.

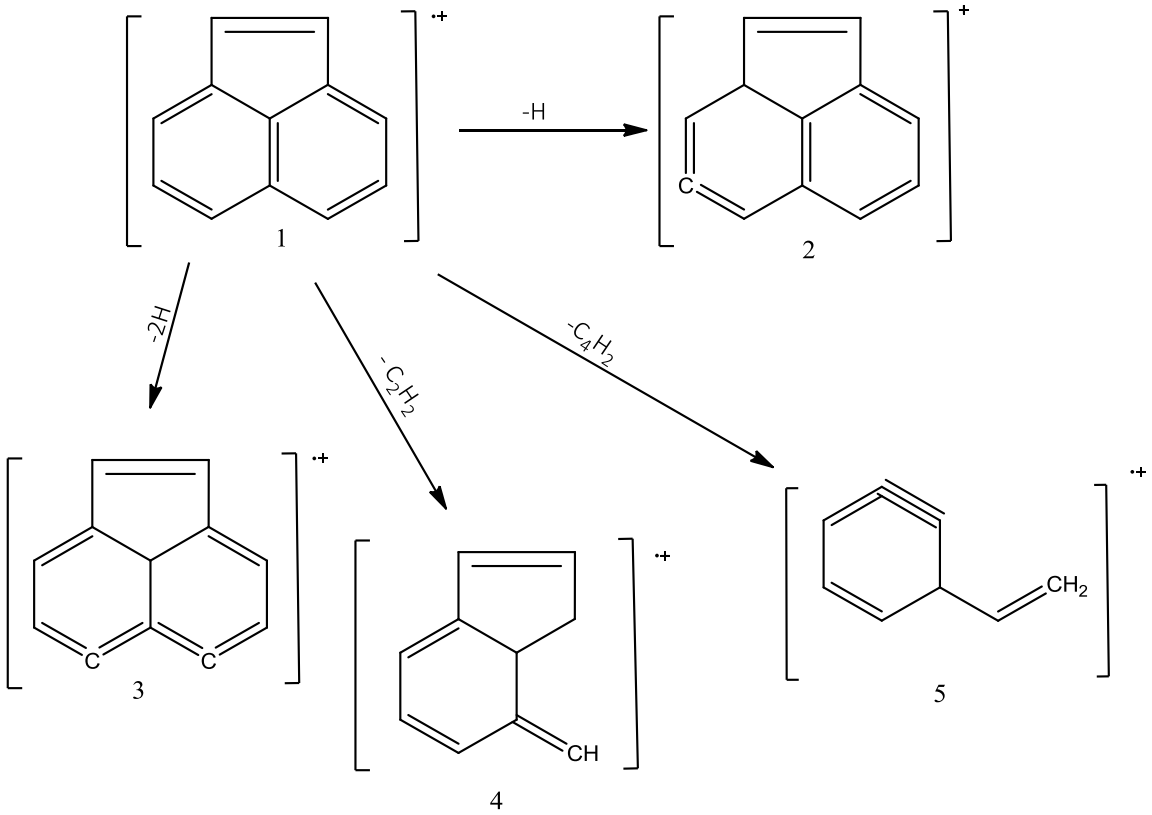

Figure A.5: schematic of all fragments from acenaphthylene radical cation with a possible structure for each channel.

A.5 Fluorene-H

Table A.5: Vibrational frequencies (cm^{-1}) of fluorene-H radical cation and primary transition state for fragment ion products. The vibrational frequencies in brackets show the frequency that was removed for each transition state.

Parent ion	M-H	M-C2H2	M-C4H2
96.62	71.4988	83.0932	77.296
112.7	83.398	96.922	90.16
220.59	163.2366	189.7074	176.472
235.73	174.4402	202.7278	188.584
278.17	205.8458	239.2262	222.536
363.6	269.064	312.696	290.88
411.68	304.6432	354.0448	329.344
425.05	314.537	365.543	340.04
448.77	332.0898	385.9422	359.016

472.64	349.7536	406.4704	378.112
500.68	500.68	500.68	500.68
517.39	517.39	517.39	517.39
598.82	598.82	598.82	598.82
627.54	627.54	627.54	627.54
692.72	692.72	692.72	692.72
723.53	723.53	723.53	723.53
735.69	735.69	735.69	735.69
777.01	777.01	777.01	777.01
789.98	789.98	789.98	789.98
840.79	840.79	840.79	840.79
866.61	866.61	866.61	866.61
883.75	883.75	883.75	883.75
914.45	914.45	914.45	914.45
978.98	978.98	978.98	978.98
990.07	990.07	990.07	990.07
1007.48	1007.48	1007.48	1007.48
1012.25	1012.25	1012.25	1012.25
1014.19	1014.19	1014.19	1014.19
1014.95	1014.95	1014.95	1014.95
1028.49	1028.49	1028.49	1028.49
1030.71	1030.71	1030.71	1030.71
1098.73	1098.73	1098.73	1098.73
1110.5	1110.5	1110.5	1110.5
1176.72	1176.72	1176.72	1176.72
1184.71	1184.71	1184.71	1184.71
1195.81	1195.81	1195.81	1195.81
1226.16	1226.16	1226.16	1226.16
1250.5	1250.5	1250.5	1250.5
1284.9	1284.9	1284.9	1284.9
1336.93	1336.93	1336.93	1336.93
1360.32	1360.32	1360.32	1360.32
1391.24	1391.24	1391.24	1391.24
1410.71	1410.71	1410.71	1410.71
1446.53	1463.77	1446.53	1446.53
1463.77	1483.92	1463.77	1463.77
1483.92	1491.69	1483.92	1483.92
1491.69	1499.57	1491.69	1491.69
1499.57	1560.07	1499.57	1499.57
1560.07	1568.56	1568.56	1560.07
1568.56	1599.27	1599.27	1568.56

1599.27	3190.08	3190.08	1599.27
3190.08	3190.5	3190.5	3190.08
3190.5	3195.42	3195.42	3190.5
3195.42	3195.79	3195.79	3195.42
3195.79	3201.45	3201.45	3195.79
3201.45	3201.98	3201.98	3201.98
3201.98	3202.97	3202.97	3202.97
3202.97	3205.28	3205.28	3205.28
3205.28	3206.33	3206.33	3206.33
3206.33			

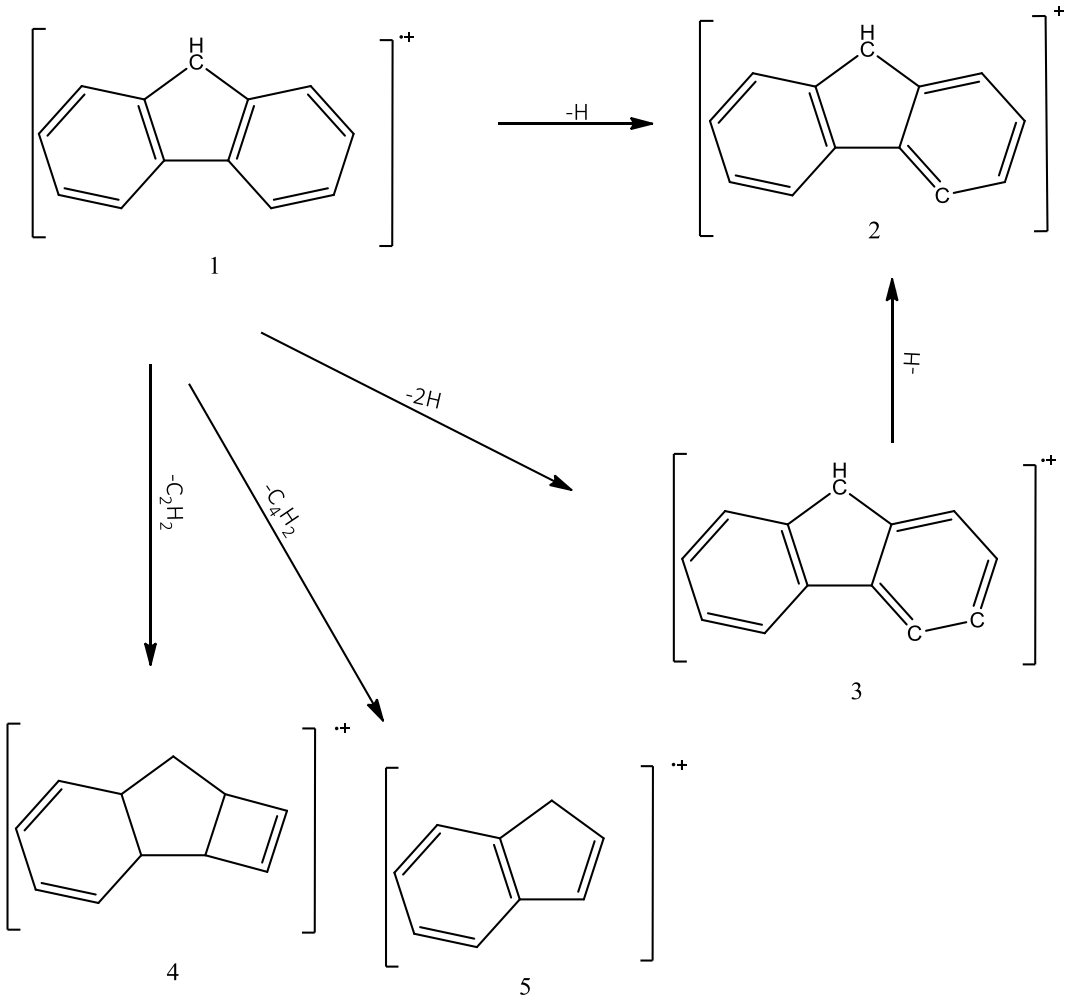

Figure A.6 : schematic of the primary fragment from fluorene-H radical cation with a possible structure for each channel.

A.6 Anthracene

Table A.6: Vibrational frequencies (cm^{-1}) of fluorene-H radical cation and primary transition state for fragment ion products. The vibrational frequencies in brackets show the frequency that was removed for each transition state.

$C_{14}H_{10}{}^{+\bullet}$ ($M^{+\bullet}$)	TS $(M-H)^{+}$	TS $(M-C_2H_2)^{+\bullet}$	TS $(M-C_4H_2)^{+\bullet}$
85.51	85.51	85.51	85.51
118.39	118.39	118.39	118.39
219.49	219.49	219.49	219.49
234.22	234.22	234.22	234.22
269.11	269.11	269.11	269.11
383.9	383.9	383.9	383.9
386.15	386.15	386.15	386.15
394.71	394.71	394.71	394.71
440.49	440.49	440.49	440.49
461.09	461.09	461.09	461.09
482.77	482.77	482.77	482.77
518.84	518.84	518.84	518.84
558.82	558.82	558.82	558.82
609.57	609.57	609.57	609.57
627.13	627.13	627.13	627.13
667.31	667.31	667.31	667.31
730.7	730.7	730.7	730.7
754.75	754.75	754.75	754.75
763.37	763.37	763.37	763.37
766.75	766.75	766.75	766.75
774.67	774.67	774.67	774.67
831.32	831.32	831.32	831.32
866.26	866.26	866.26	866.26
896.93	896.93	896.93	896.93
916.01	916.01	916.01	916.01

926.8	926.8	926.8	926.8
929.96	929.96	929.96	929.96
938.41	938.41	938.41	938.41
994.78	994.78	994.78	994.78
999.79	999.79	999.79	999.79
1024.84	1024.84	1024.84	1024.84
1025.58	1025.58	1025.58	1025.58
1050.99	1050.99	1050.99	1050.99
1120.56	1120.56	1120.56	1120.56
1158.47	1158.47	1158.47	1158.47
1189.4	1189.4	1189.4	1189.4
1204.29	1204.29	1204.29	1204.29
1209.96	1209.96	1209.96	1209.96
1210.35	1210.35	1210.35	1210.35
1282.25	1282.25	1282.25	1282.25
1301.11	1301.11	1301.11	1301.11
1307.45	1307.45	1307.45	1307.45
1318.2	1318.2	1318.2	1318.2
1375.18	1375.18	1375.18	1375.18
1409.87	1409.87	1428.73	1409.87
1428.73	1428.73	1431.83	1431.83
1431.83	1431.83	1484.46	1484.46
1484.46	1484.46	1484.77	1484.77
1484.77	1484.77	1534.07	1534.07
1534.07	1534.07	1552.92	1552.92
1552.92	1552.92	1570.38	1570.38
1570.38	1570.38	1573.15	1573.15
1573.15	1573.15	1598.51	1598.51
1598.51	1598.51	1614.91	1614.91
1614.91	1614.91	3174.41	3174.41
3174.41	3174.41	3176.28	3176.28
3176.28	3176.28	3183.38	3183.38
3183.38	3183.38	3183.7	3183.7
3183.7	3183.7	3186.34	3186.34
3186.34	3186.34	3187.01	3187.01
3187.01	3187.01	3197.63	3197.63
3197.63	3197.63	3197.76	3197.76
3197.76	3197.76	3207.63	3207.63
3207.63	3207.7	3207.7	3207.7
3207.7	(3207.63)	(1409.87)	(1428.73)

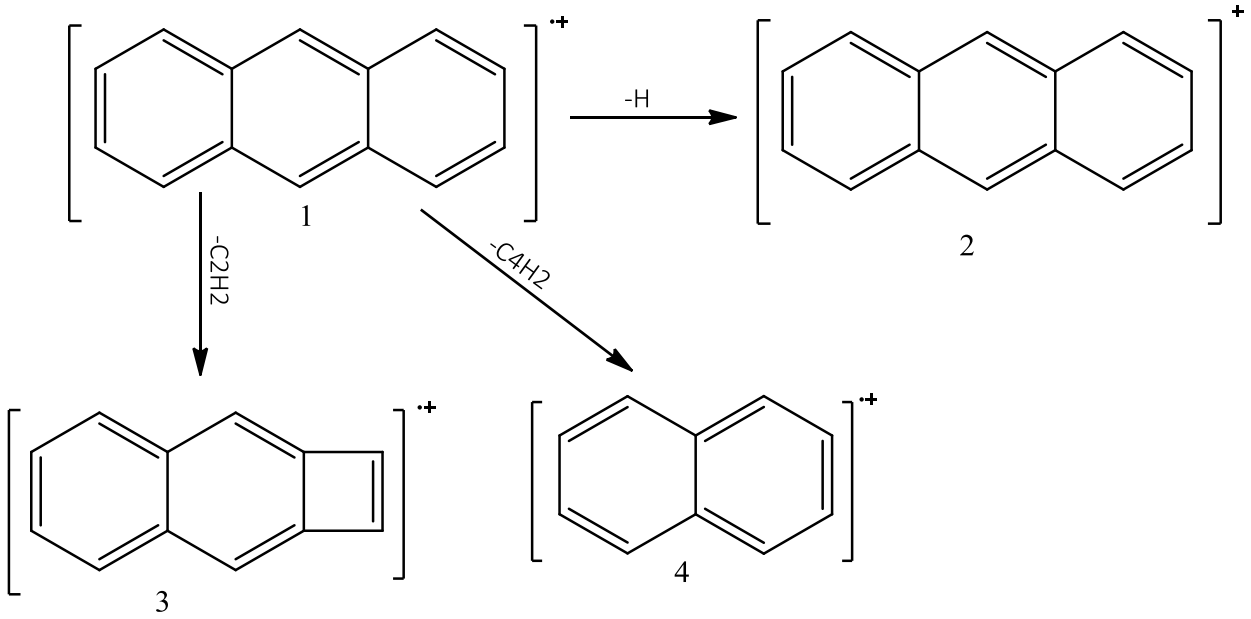

Figure A-7: schematic of all fragment from anthracene radical cation with a possible structure for each channel.

A.7 Phenanthrene

Table A.7: Vibrational frequencies (cm^{-1}) of phenanthrene radical cation and original transition state for fragmentation products. The vibrational frequencies in brackets show the frequency that was removed for each transition state.

$C_{14}H_{10}^{+\bullet}$ ($M^{+\bullet}$)	TS $(M-H)^{+}$	TS $(M-C_2H_2)^{+\bullet}$	TS $(M-C_4H_2)^{+\bullet}$
79.7783	75.78939	86.16056	67.81156
102.2622	97.14909	110.4432	86.92287
212.52	201.894	229.5216	180.642
234.322	222.6059	253.0678	199.1737
243.0311	230.8795	262.4736	206.5764
385.0503	365.7978	415.8543	327.2928
407.4507	387.0782	440.0468	346.3331
412.1016	391.4965	445.0697	350.2864

437.3335	415.4668	472.3202	371.7335
477.1055	453.2502	515.2739	405.5397
486.2297	486.2297	486.2297	486.2297
493.9397	493.9397	493.9397	493.9397
547.3853	547.3853	547.3853	547.3853
553.1944	553.1944	598.5876	553.1944
598.5876	598.5876	703.5094	598.5876
703.5094	703.5094	712.6956	703.5094
712.6956	712.6956	721.3415	712.6956
721.3415	721.3415	756.6021	721.3415
756.6021	756.6021	772.7266	756.6021
772.7266	772.7266	779.1171	772.7266
779.1171	779.1171	843.345	779.1171
843.345	843.345	855.2501	843.345
855.2501	855.2501	877.4427	855.2501
877.4427	877.4427	890.5578	877.4427
890.5578	890.5578	902.7602	890.5578
902.7602	902.7602	980.1544	902.7602
980.1544	980.1544	993.6287	980.1544
993.6287	993.6287	998.5444	993.6287
998.5444	998.5444	1004.132	998.5444
1004.132	1004.132	1017.667	1017.667
1017.667	1017.667	1020.804	1020.804
1020.804	1020.804	1058.337	1058.337
1058.337	1058.337	1060.509	1060.509
1060.509	1060.509	1113.757	1113.757
1113.757	1113.757	1155.464	1155.464
1155.464	1155.464	1162.318	1162.318
1162.318	1162.318	1163.818	1163.818
1163.818	1163.818	1200.367	1200.367
1200.367	1200.367	1239.278	1239.278
1239.278	1239.278	1249.779	1249.779
1249.779	1249.779	1281.403	1281.403
1281.403	1281.403	1314.086	1314.086
1314.086	1314.086	1324.247	1324.247
1324.247	1324.247	1339.005	1339.005
1339.005	1339.005	1388.859	1388.859
1388.859	1388.859	1447.144	1447.144
1447.144	1447.144	1457.274	1457.274
1457.274	1457.274	1457.672	1457.672
1457.672	1457.672	1462.135	1462.135

1462.135	1462.135	1538.013	1538.013
1538.013	1538.013	1552.392	1552.392
1552.392	1552.392	1555.401	1555.401
1555.401	1555.401	1580.826	1580.826
1580.826	1580.826	1600.338	1600.338
1600.338	1600.338	1636.054	1636.054
1636.054	1636.054	3182.001	3182.001
3182.001	3182.001	3185.814	3185.814
3185.814	3185.814	3186.387	3186.387
3186.387	3186.387	3190.833	3190.833
3190.833	3190.833	3192.408	3192.408
3192.408	3195.197	3195.197	3195.197
3195.197	3203.547	3203.547	3203.547
3203.547	3209.35	3209.35	3209.35
3209.35	3210.997	3210.997	3210.997
3210.997	3216.954	3216.954	3216.954
3216.954	(3192.408)	(553.1944)	(1004.132)

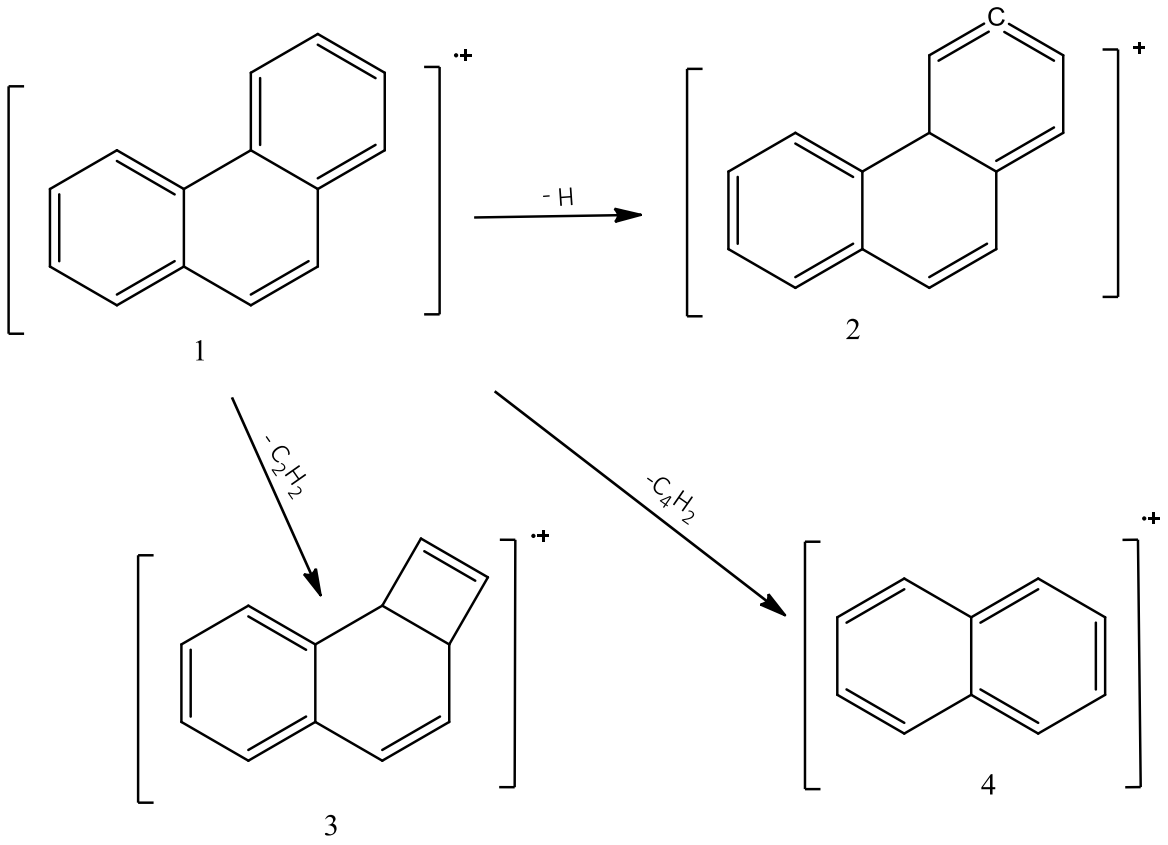

Figure A-8 :schematic of all fragment from phenanthrene radical cation with a possible structure for each channel.

A.8 Cyclopenta[d,e,f] phenanthrene

Table A.8: Vibrational frequencies (cm^{-1}) of cyclopenta[d,e,f]phenanthrene radical cation and primary transition state for fragment ion products. The vibrational frequencies in brackets show the frequency that was removed for each transition state.

parent ion	M-H
99.6292	98.63291
173.1286	171.3973
207.0056	204.9355
258.2252	255.6429
273.0739	270.3432
342.556	339.1304
428.684	424.3972

452.3461	447.8226
479.1511	474.3596
491.9851	487.0652
516.933	516.933
525.4055	525.4055
555.0976	555.0976
568.5084	568.5084
581.2857	581.2857
640.5246	640.5246
659.1673	659.1673
667.5386	667.5386
702.5206	702.5206
711.8084	711.8084
757.0763	757.0763
777.986	777.986
783.7513	783.7513
798.0557	798.0557
827.4646	827.4646
829.5523	829.5523
861.8905	861.8905
892.7186	892.7186
945.9756	945.9756
973.0263	973.0263
977.2301	977.2301
985.1384	985.1384
994.8966	994.8966
1005.459	1005.459
1025.329	1025.329
1053.705	1053.705
1059.539	1059.539
1083.223	1083.223
1133.627	1133.627
1165.471	1165.471
1193.404	1193.404
1199.775	1199.775
1203.578	1203.578
1240.443	1240.443
1262.105	1262.105
1309.138	1309.138
1352.994	1352.994
1386.507	1386.507

1409.508	1409.508
1418.397	1418.397
1432.994	1432.994
1467.012	1467.012
1495.412	1495.412
1518.972	1518.972
1558.224	1558.224
1575.3	1575.3
1584.715	1584.715
1621.898	1621.898
1692.466	1692.466
2804.991	2804.991
3153.454	3155.035
3155.035	3156.699
3156.699	3171.577
3171.577	3173.111
3173.111	3174.639
3174.639	3182.049
3182.049	3182.676
3182.676	3214.116
3214.116	(

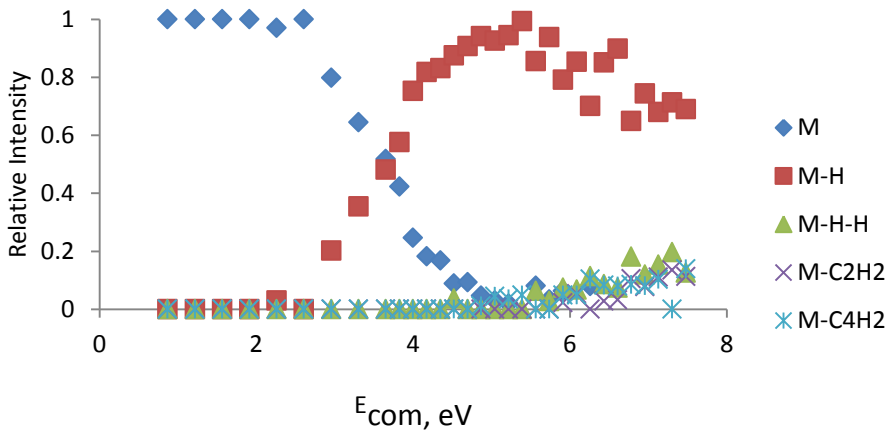

Figure A-9: experimental breakdown curve of cyclopenta[d,e,f]pheneanthrene before adding the channels to primary channel[M-H].

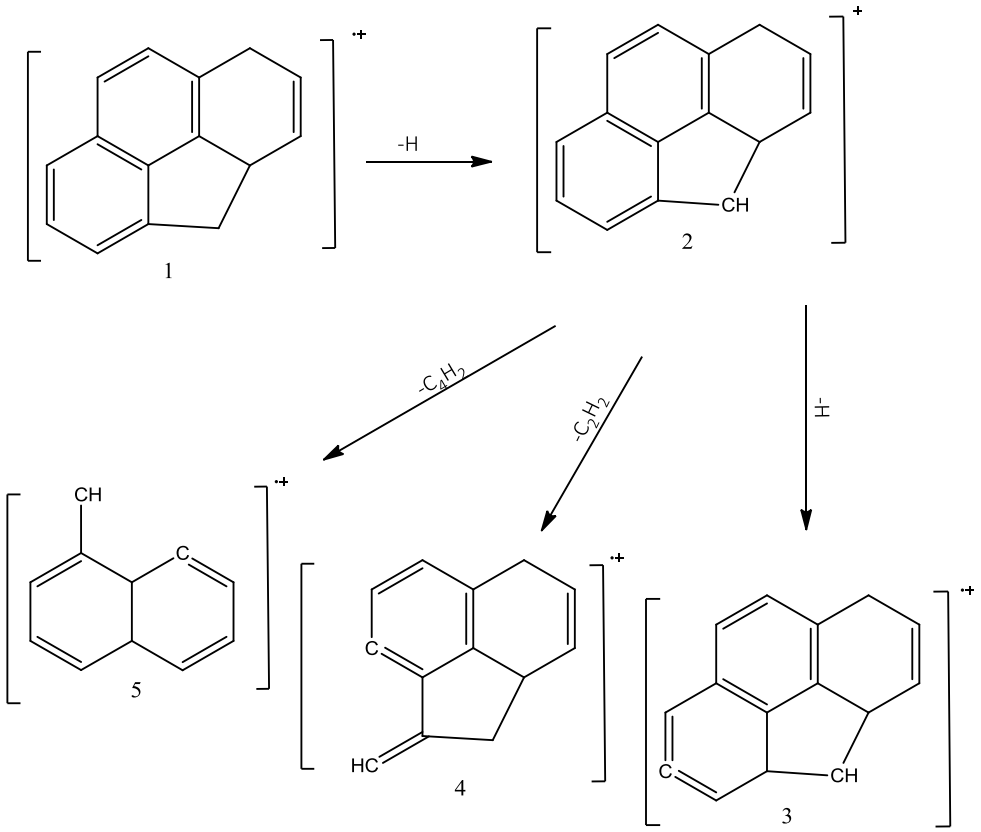

Figure A-1: schematic of all fragments from cyclopenta[d,e,f]phenanthrene radical cation with a possible structure for each channel.

A.9 Pyrene

Table A.9: Vibrational frequencies (cm^{-1}) of pyrene radical cation and primary transition state for fragment ion products. The vibrational frequencies in brackets show the frequency that was removed for each transition state.

$C_{16}H_{10}^{+\bullet}$ ($M^{+\bullet}$)	TS $(M-H)^{+}$	TS $(M-2H)^{+\bullet}$	TS $(M-C_2H_2)^{+\bullet}$
100.9755	161.5608	90.87795	85.82918
145.1396	232.2234	130.6256	123.3687
198.7748	318.0397	178.8973	168.9586

244.5974	391.3558	220.1377	207.9078
254.4994	407.199	229.0495	216.3245
353.5707	565.7131	318.2136	300.5351
399.3937	639.0299	359.4543	339.4846
413.732	661.9712	372.3588	351.6722
458.6586	733.8538	412.7927	389.8598
467.8516	748.5626	421.0664	397.6739
471.1624	471.1624	471.1624	471.1624
500.6799	500.6799	500.6799	500.6799
504.7164	504.7164	504.7164	504.7164
538.8483	538.8483	538.8483	538.8483
539.4856	539.4856	539.4856	539.4856
546.831	546.831	546.831	546.831
600.8845	600.8845	600.8845	600.8845
676.3083	676.3083	676.3083	676.3083
687.6937	687.6937	687.6937	687.6937
694.1494	694.1494	694.1494	694.1494
710.7154	710.7154	710.7154	710.7154
742.0781	742.0781	742.0781	742.0781
779.433	779.433	779.433	779.433
805.4822	805.4822	805.4822	805.4822
815.6729	815.6729	815.6729	815.6729
830.8374	830.8374	830.8374	842.8469
842.8469	842.8469	842.8469	873.5285
873.5285	873.5285	873.5285	949.0841
949.0841	949.0841	949.0841	959.9141
959.9141	959.9141	959.9141	991.8412
991.8412	991.8412	991.8412	993.8505
993.8505	993.8505	993.8505	1002.856
1002.856	1002.856	1002.856	1004.19
1004.19	1004.19	1004.19	1011.566
1011.566	1011.566	1011.566	1014.132
1014.132	1014.132	1014.132	1094.689
1094.689	1094.689	1094.689	1121.245
1121.245	1121.245	1121.245	1144.38
1144.38	1144.38	1144.38	1168.339
1168.339	1168.339	1168.339	1170.812
1170.812	1170.812	1170.812	1202.451
1202.451	1202.451	1202.451	1213.613
1213.613	1213.613	1213.613	1234.386
1234.386	1234.386	1234.386	1247.798

1247.798	1247.798	1247.798	1264.014
1264.014	1264.014	1264.014	1266.055
1266.055	1266.055	1266.055	1364.726
1364.726	1364.726	1364.726	1370.017
1370.017	1370.017	1370.017	1373.354
1373.354	1373.354	1373.354	1423.256
1423.256	1423.256	1423.256	1448.406
1448.406	1448.406	1448.406	1451.143
1451.143	1451.143	1451.143	1463.004
1463.004	1463.004	1463.004	1465.858
1465.858	1465.858	1465.858	1516.049
1516.049	1516.049	1516.049	1519.897
1519.897	1519.897	1519.897	1559.259
1559.259	1559.259	1559.259	1580.298
1580.298	1580.298	1580.298	1585.055
1585.055	1585.055	1585.055	1592.6
1592.6	1592.6	1592.6	1656.808
1656.808	1656.808	1656.808	3182.898
3182.898	3182.898	3182.898	3183.543
3183.543	3183.543	3183.543	3184.302
3184.302	3184.302	3184.302	3185.307
3185.307	3188.068	3185.307	3188.068
3188.068	3188.76	3188.068	3188.76
3188.76	3197.218	3188.76	3197.218
3197.218	3197.264	3197.218	3197.264
3197.264	3208.043	3208.043	3208.043
3208.043	3208.118	3208.118	3208.118
3208.118	(3185.307)	(3197.264)	(830.8374)

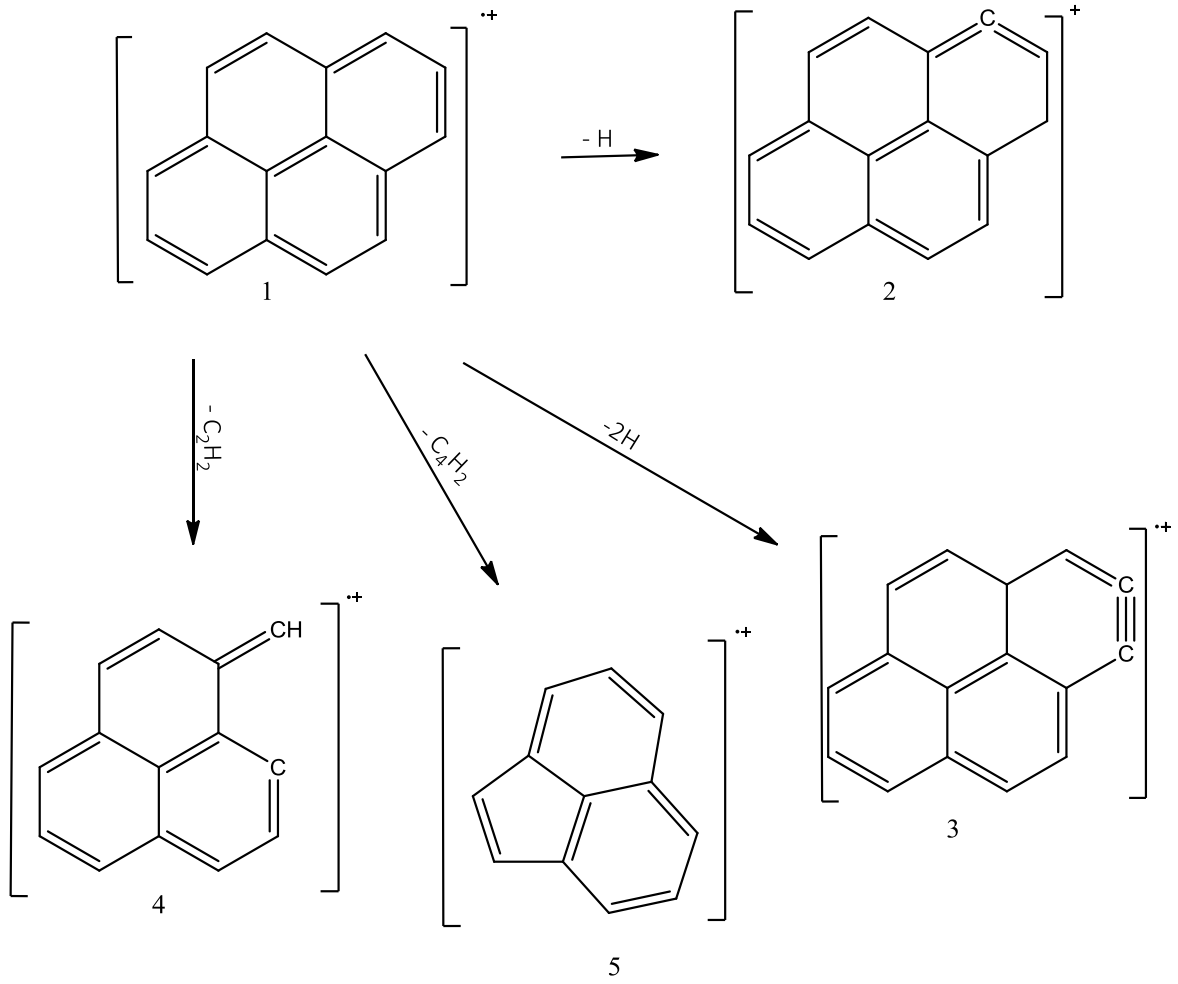

Figure A-2: schematic of all fragments from pyrene radical cation with a possible structure for each channel.

A.10 Fluoranthene

Table A.10: Vibrational frequencies (cm^{-1}) of fluoranthene radical cation and primary transition state for daughter ion products. The vibrational frequencies in brackets show the frequency that was removed for each transition state.

$C_{16}H_{10}^{+\bullet}$ ($M^{+\bullet}$)	TS $(M\text{-}H)^{+}$	TS $(M\text{-}2H)^{+\bullet}$	TS $(M\text{-}(C2H2+C4H2))^{+\bullet}$
102.2981	60.35588	91.04531	96.16021
121.3449	71.59349	107.997	114.0642
165.2921	97.52234	147.11	155.3746
208.1334	122.7987	185.2387	195.6454
253.4633	149.5433	225.5823	238.2555
294.7728	173.916	262.3478	277.0864

356.3247	210.2316	317.129	334.9452
433.3164	255.6567	385.6516	407.3174
436.528	257.5515	388.5099	410.3363
464.3762	273.982	413.2948	436.5136
477.356	477.356	477.356	477.356
493.2254	493.2254	493.2254	493.2254
570.1523	570.1523	570.1523	570.1523
571.0697	571.0697	571.0697	571.0697
571.6977	571.6977	571.6977	571.6977
627.2273	627.2273	627.2273	627.2273
627.4267	627.4267	627.4267	627.4267
648.5062	648.5062	648.5062	648.5062
684.2624	684.2624	684.2624	684.2624
746.3347	746.3347	746.3347	746.3347
752.8644	752.8644	752.8644	752.8644
776.6553	776.6553	776.6553	776.6553
783.1728	783.1728	783.1728	783.1728
788.5249	788.5249	788.5249	788.5249
816.1166	816.1166	816.1166	816.1166
826.9247	826.9247	826.9247	826.9247
882.5668	882.5668	882.5668	882.5668
905.9304	905.9304	905.9304	905.9304
918.3416	918.3416	918.3416	918.3416
927.173	927.173	927.173	927.173
953.7003	953.7003	953.7003	953.7003
981.3597	981.3597	981.3597	981.3597
989.0518	989.0518	989.0518	989.0518
989.8737	989.8737	989.8737	989.8737
990.8752	990.8752	990.8752	990.8752
1037.717	1037.717	1037.717	1037.717
1042.619	1042.619	1042.619	1042.619
1060.802	1060.802	1060.802	1060.802
1105.32	1105.32	1105.32	1105.32
1122.75	1122.75	1122.75	1122.75
1161.051	1161.051	1161.051	1161.051
1182.22	1182.22	1182.22	1182.22
1184.145	1184.145	1184.145	1184.145
1207.742	1207.742	1207.742	1207.742
1234.278	1234.278	1234.278	1234.278
1253.269	1253.269	1253.269	1253.269
1292.335	1292.335	1292.335	1292.335

1317.354	1317.354	1317.354	1317.354
1339.837	1339.837	1339.837	1339.837
1395.035	1395.035	1395.035	1395.035
1401.913	1401.913	1401.913	1401.913
1441.166	1441.166	1441.166	1441.166
1452.455	1470.591	1452.455	1452.455
1470.591	1484.554	1470.591	1484.554
1484.554	1504.522	1484.554	1504.522
1504.522	1520.993	1504.522	1520.993
1520.993	1612.233	1520.993	1612.233
1612.233	1638.559	1612.233	1638.559
1638.559	1641.058	1638.559	1641.058
1641.058	1644.017	1641.058	1644.017
1644.017	1656.718	1644.017	1656.718
1656.718	3160.406	1656.718	3160.406
3160.406	3161.071	3160.406	3161.071
3161.071	3161.203	3161.071	3161.203
3161.203	3166.94	3161.203	3166.94
3166.94	3170.702	3166.94	3170.702
3170.702	3171.558	3170.702	3171.558
3171.558	3177.21	3171.558	3177.21
3177.21	3183.881	3183.881	3183.881
3183.881	3184.633	3184.633	3184.633
3184.633	3189.179	3189.179	3189.179
3189.179	(1452.455)	(3177.21)	(1470.591)

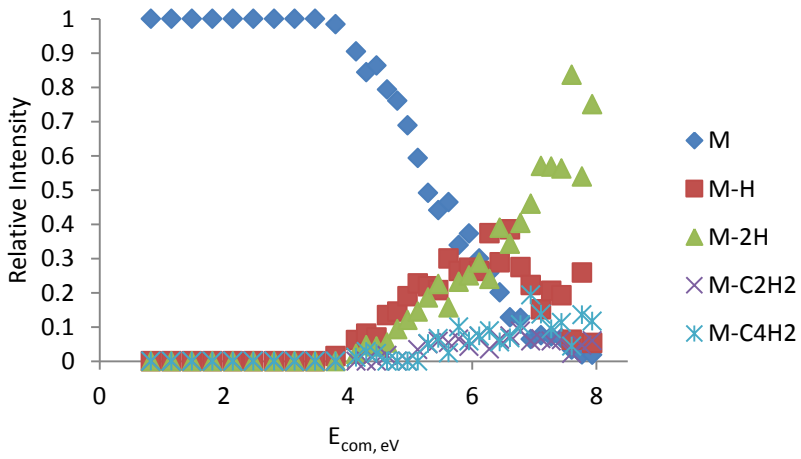

Figure A-12 : experimental breakdown curve of fluoranthrene before adding the M-C_2H_2 channel to M-C_4H_2 channel and the channel M-2H to M-H at 6 eV and above.

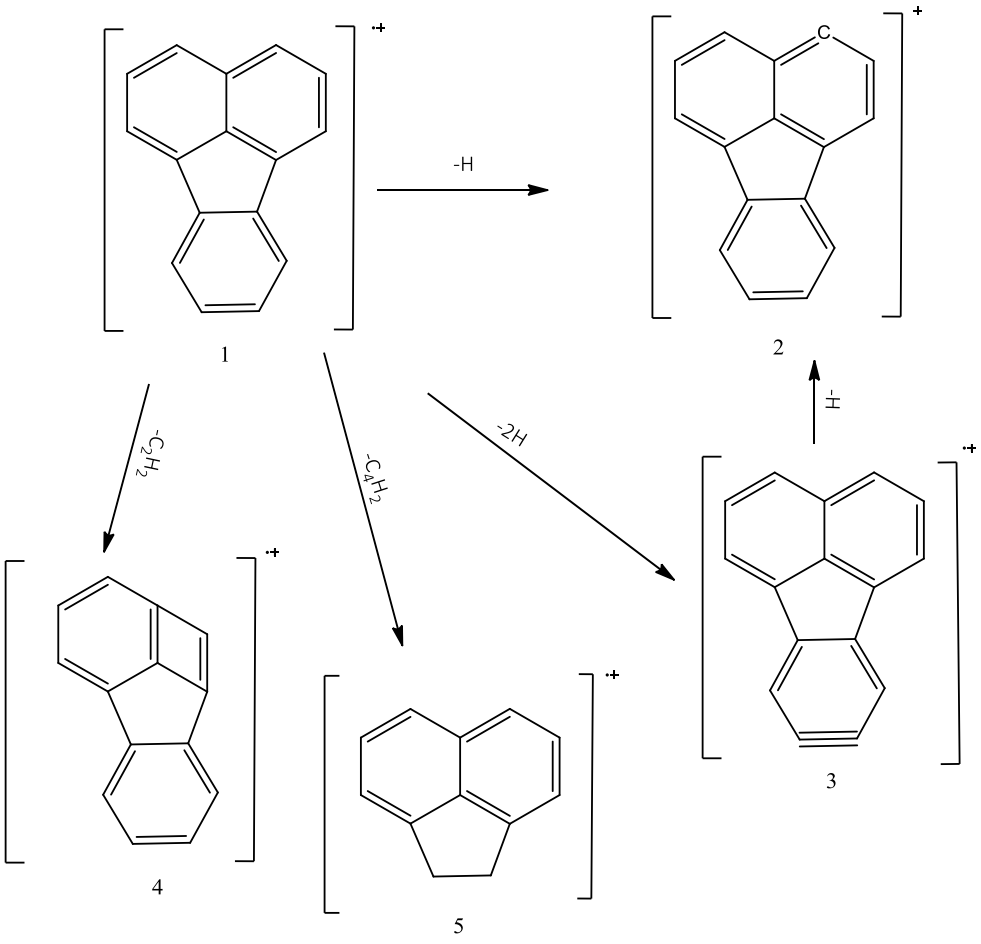

Figure A-3: schematic of all fragment from fluoranthene radical cation with a possible structure for each channel.

A.11 Perylene

Table A.11: Vibrational frequencies (cm^{-1}) of perylene radical cation and primary transition state for fragment ion products. The vibrational frequencies in brackets show the frequency that was removed for each transition state.

$C_{20}H_{10}^{+\bullet}$ ($M^{+\bullet}$)	TS $(M-H)^{+}$	TS $(M-2H)^{+\bullet}$
43.3403	58.50941	43.3403
90.613	122.3276	90.613
137.4268	185.5262	137.4268
169.0902	228.2718	169.0902
200.7391	270.9978	200.7391
244.7599	330.4259	244.7599
251.7128	339.8123	251.7128
278.6765	376.2133	278.6765
357.595	482.7533	357.595
368.6609	497.6922	368.6609
412.8375	412.8375	412.8375
434.9276	434.9276	434.9276
447.8897	447.8897	447.8897
459.9024	459.9024	459.9024
465.3935	465.3935	465.3935
510.4805	510.4805	510.4805
529.026	529.026	529.026
534.6291	534.6291	534.6291
536.7759	536.7759	536.7759
553.9808	553.9808	553.9808
586.2685	586.2685	586.2685
618.7647	618.7647	618.7647
630.7763	630.7763	630.7763
632.1981	632.1981	632.1981
649.8518	649.8518	649.8518
692.0782	692.0782	692.0782
729.9951	729.9951	729.9951

774.7352	774.7352	774.7352
778.9964	778.9964	778.9964
797.544	797.544	797.544
803.1695	803.1695	803.1695
809.817	809.817	809.817
813.8465	813.8465	813.8465
815.6437	815.6437	815.6437
825.5425	825.5425	825.5425
927.4447	927.4447	927.4447
936.1758	936.1758	936.1758
950.1596	950.1596	950.1596
957.0491	957.0491	957.0491
962.1064	962.1064	962.1064
1005.884	1005.884	1005.884
1006.497	1006.497	1006.497
1010.546	1010.546	1010.546
1012.172	1012.172	1012.172
1015.662	1015.662	1015.662
1053.758	1053.758	1053.758
1088.802	1088.802	1088.802
1120.926	1120.926	1120.926
1132.793	1132.793	1132.793
1149.404	1149.404	1149.404
1168.74	1168.74	1168.74
1179.558	1179.558	1179.558
1212.544	1212.544	1212.544
1223.006	1223.006	1223.006
1230.554	1230.554	1230.554
1246.166	1246.166	1246.166
1246.904	1246.904	1246.904
1256.75	1256.75	1256.75
1318.328	1318.328	1318.328
1323.405	1323.405	1323.405
1367.268	1367.268	1367.268
1372.18	1372.18	1372.18
1398.658	1398.658	1398.658
1400.756	1400.756	1400.756
1408.345	1408.345	1408.345
1417.442	1417.442	1417.442
1473.65	1473.65	1473.65
1479.003	1479.003	1479.003

1480.875	1480.875	1480.875
1492.621	1492.621	1492.621
1519.91	1519.91	1519.91
1566.148	1566.148	1566.148
1586.326	1586.326	1586.326
1589.548	1589.548	1589.548
1596.829	1596.829	1596.829
1604.74	1604.74	1604.74
1608.4	1608.4	1608.4
1618.772	1618.772	1618.772
3184.388	3184.388	3184.388
3184.648	3184.648	3184.648
3187.057	3187.057	3187.057
3187.593	3187.593	3187.593
3198.345	3198.345	3198.345
3198.755	3198.755	3202.131
3202.131	3202.131	3202.564
3202.564	3211.113	3211.113
3211.113	3211.134	3211.134
3211.134	3225.479	3225.479
3225.479	3225.608	3225.608
3225.608	(3202.564)	(3198.755)

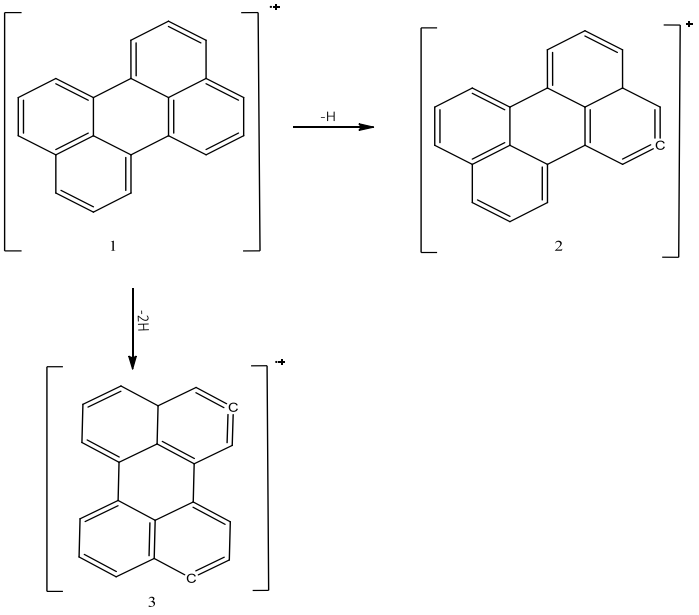

Figure **A**-4**: s**chematic of all fragments from perylene radical cation with a possible structure for each channel**.**

A.12 Coronene

Table A.12: Vibrational frequencies (cm^{-1}) of coronene radical cation and primary transition state for the produces of fragmentation. The vibrational frequencies in brackets show the frequency that was deleted for each transition state.

$C_{24}H_{12}^{+\bullet}$ ($M^{+\bullet}$)	TS $(M-H)^{+}$	TS $(M-2H)^{+\bullet}$
84.9943	86.69419	84.9943
89.0208	90.80122	89.0208
92.0376	93.87835	92.0376
122.4845	124.9342	122.4845
159.8899	163.0877	159.8899
221.4203	225.8487	221.4203
282.4689	288.1183	282.4689
292.794	298.6499	292.794
297.5668	303.5181	297.5668
298.7509	304.7259	298.7509
370.2535	370.2535	370.2535
380.1545	380.1545	380.1545
384.4781	384.4781	384.4781
436.812	436.812	436.812
443.1224	443.1224	443.1224
468.1199	468.1199	468.1199
476.5564	476.5564	476.5564
479.3837	479.3837	479.3837
488.6973	488.6973	488.6973
495.859	495.859	495.859
498.7722	498.7722	498.7722
514.119	514.119	514.119
537.9982	537.9982	537.9982
552.4949	552.4949	552.4949
557.7671	557.7671	557.7671
636.0744	636.0744	636.0744
653.2295	653.2295	653.2295
657.9638	657.9638	657.9638
676.9762	676.9762	676.9762
684.1978	684.1978	684.1978
685.3999	685.3999	685.3999
687.4259	687.4259	687.4259

709.197	709.197	709.197
724.9687	724.9687	724.9687
752.3177	752.3177	752.3177
772.7626	772.7626	772.7626
776.5089	776.5089	776.5089
790.5397	790.5397	790.5397
805.2907	805.2907	805.2907
811.6449	811.6449	811.6449
826.4371	826.4371	826.4371
831.0632	831.0632	831.0632
869.8026	869.8026	869.8026
871.9884	871.9884	871.9884
890.9128	890.9128	890.9128
935.6817	935.6817	935.6817
976.6176	976.6176	976.6176
983.721	983.721	983.721
990.4817	990.4817	990.4817
996.9615	996.9615	996.9615
1002.776	1002.776	1002.776
1006.398	1006.398	1006.398
1010.79	1010.79	1010.79
1021.682	1021.682	1021.682
1058.988	1058.988	1058.988
1156.815	1156.815	1156.815
1162.723	1162.723	1162.723
1169.969	1169.969	1169.969
1179.686	1179.686	1179.686
1191.204	1191.204	1191.204
1201.224	1201.224	1201.224
1237.396	1237.396	1237.396
1238.363	1238.363	1238.363
1246.852	1246.852	1246.852
1248.699	1248.699	1248.699
1260.002	1260.002	1260.002
1269.816	1269.816	1269.816
1327.512	1327.512	1327.512
1341.364	1341.364	1341.364
1349	1349	1349
1392.437	1392.437	1392.437
1400.84	1400.84	1400.84
1402.243	1402.243	1402.243

1430.487	1430.487	1430.487
1433.962	1433.962	1433.962
1438.461	1438.461	1438.461
1451.952	1451.952	1451.952
1464.482	1464.482	1464.482
1494.245	1494.245	1494.245
1506.698	1506.698	1506.698
1508.981	1508.981	1508.981
1514.821	1514.821	1514.821
1537.734	1537.734	1537.734
1553.804	1553.804	1553.804
1560.74	1560.74	1560.74
1576.279	1576.279	1576.279
1610.437	1610.437	1610.437
1619.417	1619.417	1619.417
1637.674	1637.674	1637.674
1675.255	1675.255	1675.255
3196.472	3196.472	3196.472
3196.932	3196.932	3196.932
3197.505	3197.505	3197.505
3198.505	3198.505	3198.542
3198.542	3198.542	3199.22
3199.22	3199.22	3210.633
3210.633	3210.633	3211.131
3211.131	3211.131	3211.266
3211.266	3211.922	3211.922
3211.922	3213.419	3213.419
3213.419	3213.68	3213.68
3213.68	(3211.266)	(3198.505)

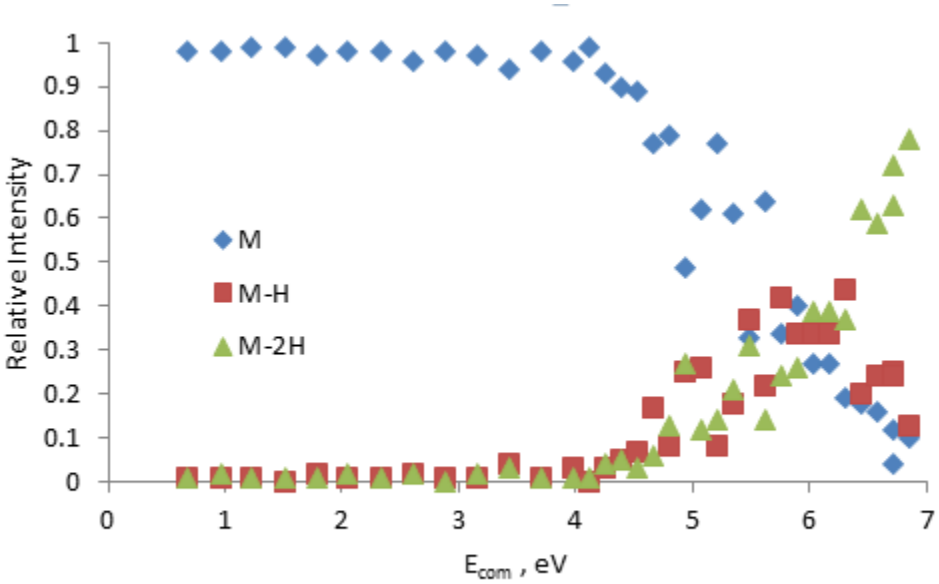

Figure A-5: experimental breakdown curve for coroene radical cation before adding the intensity of M-2H to the M-H intensity at 5.5 eV and above.

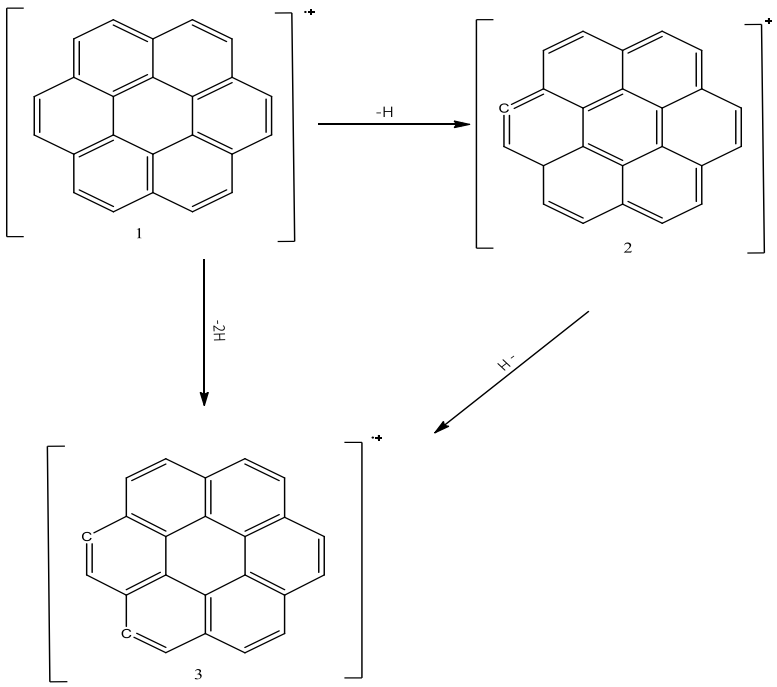

Figure A-6: schematic of all fragments from coronene radical cation with a possible structure for each channel.